Structural and Compositional Properties of Semiconductor Quantum Dots and Nanocrystals

A thesis submitted to The University of Manchester for the degree of PhD
in the Faculty of Engineering and Physical Sciences

2010

Reza Jalilikashtiban

School of Materials

Table of Contents

The total number words: 32,102

List of Figures

Abstract

The thesis presented here entitled “Structural and Compositional Properties of Semiconductor Quantom Dots and Nanocrystals” for the degree of Doctor of Philosophy is submitted to the University of Manchester by Reza Jalilikashtiban in August 2010.

The research carried out here employed analytical and imaging transmission electron microscopy and scanning transmission electron microscopy to gain a good understanding of local structure and composition of semiconductor nanocrystals and quantum dots for electronics and optoelectronics applications. One of the world’s most advanced analytical scanning transmission electron microscopes in the field, the Daresbury SuperSTEM, was used to scrutinise the structure and composition of the samples. Three nanostructure systems are investigated in this thesis:

1. Structures consisting of Ge-nanocrystals (NCs) in alumina. Here HRTEM suggests relaxed and twinned smaller NCs grown annealed at lower temperature compared to elongated non-faulty bigger NCs annealed at higher temperature. HRTEM also suggests a polycrystalline structure of the matrix.

2. With regards to the InAs/GaAs quantum dots (QD) the study aims in particular at elucidating QD formation by investigating samples grown with and without growth interrupt (GI). Diffraction contrast TEM shows formation of buried dots in the sample prepared with GI whereas for the sample without GI the immediate growth of GaAs after InAs inhibits diffusion and segregation of In adotoms, and no footprint of buried dots has been observed. HRTEM and HAADF show coherent QDs in the sample with GI and abrupt InAs/GaAs interfaces in the sample without GI. In executing energy electron loss spectroscopy (EELS) and geometric phase analysis (GPA) the distribution of In in InGaAs/GaAs QDs has been obtained in samples grown in the critical thickness regime for quantum dot formation. The highest In percentage achieved in the dots grown with a nominal fraction of 100% was ~70%. EELS shows variations in the In concentration within the QD structure and wetting layer

3. In the case of Er-doped Si-NCs in silica this research tries to provide an understanding of structure, composition and position of excess Si and Er in the silica matrix of materials prepared under different growth conditions and to correlate this information with the PL emission, all with the aim to find preparation routes for optimum optical efficiency for applications of this materials system in silicon photonics. High spatial correlation between Si-NCs, Er and O in the Er and Si co-implanted sample with strong indication of an Er-oxide/Si core-shell structure had been found. The lack of an Er-oxide plasmon indicates, however, that the shell structure and its interface with the SiNCs is highly defective and a likely cause for non-radiative recombination. The sample with similar excess Er and Si concentrations but prepared in a two-stage implantation and annealing process shows a 10 times improvement in the optical emission. Here no spatial correlation between Er and Si-NCs was found in core loss EELS. EELS and HAADF evidenced more highly, near-atomically dispersed Er in the matrix with no formation of a core-shell structure as compared to the co-implanted sample. No footprint of Er-silicide plasmon was observed by low loss valence band EELS investigation in the co-implanted sample.

Declarations

No portion of the work referred to in the thesis has been submitted in support of an application for another degree or qualification of this or any other university or other institute of learning.

Copyright

List of publications

1. Iain F. Crowe, Reza J. Kashtiban, Ben Sherliker, Ursel Bangert, Matthew P. Halsall, Andrew P. Knights and Russell M. Gwilliam. "*Spatially correlated Er and Si-nanocrystals in co-implanted silica after and a single high temperature annealing*" Journal of Applied Physics **107** (2010) 044316

2. M. Buljan, S. R. C. Pinto, R. J. Kashtiban, A. G. Rolo, A. Chahboun, U. Bangert, S. Levichev, V. Hol´y and M. J. M. Gomes *"Size and spatial homogeneity of SiGe quantum dots in amorphous silica matrix"* Journal of Applied Physics, **106** (2009) 084319

3. R. J. Kashtiban, S. R. C. Pinto, U. Bangert, A. G. Rolo, A. Chahboun, M. J. M. Gomes and A. J. Harvey. *"Ge-nanocrystals in Al_2O_3 matrix: a structural study"* Journal of Physics: Conference Series **209** (2010) 012060

4. R. J. Kashtiban, U. Bangert, B.Sherliker, M. P. Halsall and A. J. Harvey. *"Study of InGaN/GaN quantum dot systems by TEM techniques and PL spectroscopy"* Journal of Physics: Conference Series **209** (2010) 012038

5. R. J. Kashtiban, U. Bangert, I. Crowe, M. P. Halsall, B. Sherliker, A. J. Harvey, J. Eccles, A. P. Knights, R. Gwilliam, M. Gass *"Structural and compositional study of Er-doped silicin nanocrystals by HAADF, EELS and HRTEM techniques in an aberration corrected STEM"* Journal of Physics: Conference Series **209** (2010) 012043

6. S. R. C. Pinto, A. G. Rolo, A. Chahboun, Maja Buljan, A. Khodorov, R. J. Kashtiban, U. Bangert, N. P. Barradas, E. Alves and M. J. M. Gomes *"Multilayers of Ge nanocrystals embedded in Al_2O_3 matrix: structural and electrical studies"* Microelectronic Engineering (2010) article in press

7. R. J. Kashtiban U. Bangert, I. Crowe, M. P. Halsall, A. P. Knights, R. Gwilliam, M. Gass. **"***Structural and compositional study of Er-doped silicon nanocrystals"* (Accepted for publication in Inst. Phys. Conf. Ser.)

8. R. J. Kashtiban, U. Bangert and M. Missous *"The Investigation of the effect of growth interruption on structural formation of InAs/GaAs quantum dots superlattice structures grown by molecular beam epitaxy"* Microelectronics Journal **40** (2009) 479

9. S. C. Davies, D. J. Mowbray, F. Ranalli, P. J. Parbrook, Q. Wang, T. Wang, B. S. Yea, B. J. Sherliker, M. P. Halsall, R. J. Kashtiban and U. Bangert *"Optical and microstructural studies of InGaN/GaN quantum dot ensembles"* Applied Physics Letters **95** (2009) 111903

10. S. R. C. Pinto, A. G. Rolo, A. Chahboun, R. J. Kashtiban, U. Bangert, M. J. M. Gomes *"Raman study of stress effect on Ge nanocrystals embedded in Al_2O_3"* Thin Solid Films **518** (2010) 5378

11. S R C Pinto, M Buljan, R J Kashtiban, A G Rolo, A Chahboun, U Bangert, N P Barradas, E Alves, M J M Gomes (2010*) "Structural study of $Si_{1-x}Ge_x$ nanocrystals embedded in SiO2 films"* Thin Solid Films **518** (2010) 2569

12. R. J. Kashtiban U. Bangert, I. Crowe, M. P. Halsall, A. P. Knights, R. Gwilliam, M. Gass. ***"****Pin-pointing Er and O in Er-doped silicon nanocrystals in Silica"* (in preparation for submission to Ultramicrocopy)

Acknowledgements and dedication

I am heartily thankful to my supervisor, Dr Ursel Bangert, whose outstanding encouragement, supervision and support from the preliminary to the concluding level enabled me to develop an understanding of the subject.

Many thanks goes to our group members, Iain, Ashley, James, Recep for their fruitful discussions and specially Dr Alan Harvey who shared his knowledge of electron microscopy with me.

I would like also to thank and express my appreciation to Dr Matthew Hallsal for his great support and Iain Crowe for PL results of Er samples, Dr Anabel Rolo from the University of Minho for helpful discussions and growth of Ge-NCs sample and Sara Pinto for Raman and XRD data.

I offer my regards to Prof. Mohamed Missous for fruitful discussion in his well organised group meetings, and his group members for providing excellent InAs/GaAs samples and PL and XRD data.

Many thanks go to all the SuperSTEM team specially Prof. Andrew Bleloch and Dr Mhairi Gass for their assistance with measurements and constructive discussions.

I offer my special regards and blessings to my parents and parents in law who supported me in any respect during the completion of the project.

Words fail to express my appreciation for my wife Somayyeh whose dedication, love and understanding has taken the load off my shoulders. I give my greatest thanks to my daughter Ana for coping with holidays and weekends spent without dad, and my little son Ali who inspired hope and commitment in me to build a brighter future.

...dedicated to my parents!

1

Introduction

1.1 Background and Motivation

In bulk semiconductors the band gap energy is governed by the composition of the material. However when the size of semiconductor approaches the size of an exciton (e.g. a quasi-particle consists of a photo-excited electron and a hole bound to each other by a Coulomb interaction) in the bulk crystal, known as Bohr exciton radius, quantum confinement effects occur. Emission from a bulk semiconductor is a result of recombination of optically or electrically produced electron-hole pairs. When the size of a semiconductor is reduced to less than the size of an exciton further energy is needed to confine the electron-hole pair within the semiconductor. This results in a shift towards shorter wavelengths of light emission. Quantum Dots (QDs) are semiconductors which are smaller than the size of the Bohr exciton radius in three dimensions. Confinement of the excitons within the QD leads to a shift in the band gap to higher energies. By tuning the size and the composition of the QDs, wavelength tuneablity of excitation and emission processes can be achieved, and this makes QDs unique objects for scientific and technological applications. InAs/GaAs QDs and Er-doped Si-NCs in silica are favourable candidates for photonics and optical communication technology at around 1.55µm. Ge and SiGe NCs in alumina and silica dielectric oxides have been proposed as propitious structures for future long retention time memory devices.

In order to implement these structures for practical use a number of problems and points of interest are currently arising, some of which will be addressed in this thesis.

(i) InAs/GaAs QDs are promising candidates for applications such as high temperature photo-detectors and fibre optic communication repeaters [1]. Despite much research in

the last 15 years QD formation mechanism and structural and compositional properties of such nanostructures are not clearly understood yet.

(ii) The advantage of integration into current electronics devices based on cheap Si technology makes small-size fibre amplifiers a profitable research field. Current erbium doped fibre amplifiers (EDFA) use expensive lasers to pump erbium ions to produce 1.54 μm emissions [2]. On the other hand the low absorption cross section of the Er makes larger active volumes necessary to achieve the desirable intensity, which then leads to a larger device size. Introducing Si-NCs into Er-doped silica [3] leads to a significant increase in intensity of 1.54 μm emissions with the benefit of reduced device sizes. Furthermore a 10^4 times increase in the absorption cross section due to the presence of Si-NCs enables the use of cheap LEDs instead of expensive lasers as pump sources. This enhancement in the performance and reduction in the size and cost of Er-doped Si-NCs based structure makes it a potential platform for future optoelectronics devices [4]. In this system Si-NCs act as sensitizer of Er ions [5]. Excited Si-NCs relax by sensitizing Er Ions through a dipole-dipole interaction [6]. As this sensitization is a short range mechanism the position and chemical compound of the Er ion and the size of Si-NCs are important.

(iii) Among devices for optoelectronic and nano-electronic, the use of Metal–Insulator–Semiconductor (MIS) structures using Si and Ge semiconductor NCs have also been reported to show good memory effects and low power operation at room temperature [7]. In fact, one of the most common structures used for memory or LED purposes consists of Si-NCs embedded in a SiO_x layer grown on a Si substrate. However, alumina is also used as a dielectric matrix, and Ge and SiGe NCs are also often formed inside those matrices [8]. Still, in most of the works found in the literature the NCs have been grown inside a SiO_2 matrix. Constant shrinking of the thickness of gate dielectrics to below 2-3 nm has led to a search for alternative materials, whose dielectric constant is higher than that of SiO_2, but whose other properties remain similar to SiO_2 [9]. Because of its similar band gap (9eV) and more than twice as high dielectric constant ($k_{Al_2O_3}$=9 and k_{SiO_2} =3.9), Al_2O_3 is a good candidate to replace SiO_2 as a gate dielectric

material and is starting to be used in today's modern electronic technology [10, 11]. Moreover Al_2O_3 presents good mechanical properties, which leads it to be, at least in theory, an ideal material for device application.

The research carried out here employs a battery of analytical and imaging TEM techniques to study structure and composition of semiconductor QDs for photonics, optical communication and memory device applications. Specifically, aberration corrected scanning transmission electron microscopes (STEM)s are used to scrutinise the structure and composition of the samples.

Potential photonics and optical telecommunication application of QDs and NCs have been encouraging materials scientist and physicists for the last 15 years. A clear understanding of QD formation will allow researchers to establish growth parameters to achieve QDs with certain compositions and well defined size distributions e.g., in order to obtain emission wavelengths of particular interest together with high intensity emission.

1.2 Outline of Research

A brief survey of characterization techniques and methods used to study the materials in this research is given in chapter 2. In section 2.2 and 2.3 basics of electron optics are presented and some key points of image formation mechanisms are described. Fundamentals of high resolution electron microscopy (HREM) and geometric phase analysis (GPA) are presented in section 2.4 and 2.5. The STEM is a powerful analytical instrument for the exploration of nanostructured materials. A brief explanation of this instrument is given in 2.6. The electron energy loss (EEL) spectroscopy technique as the core investigation method of this research as well as the features in the EEL spectrum are summarised in section 2.7 together with the EEL spectrum imaging (SI) technique and schematics of the SI acquisition. Data analysis methods, i.e., non linear least square fitting and Kramers-Kronig (KK) analysis are explained in sections 2.7.2 and 2.8. Non-destructive photoluminescence (PL) and X-ray diffraction (XRD) methods and the relationship between these techniques and the physical properties of nanostructures are

briefly discussed in parts 2.9 and 2.10. In the final section of chapter 2 transmission electron microscopy cross sectional sample preparation is explained.

Chapter 3 describes important background theories of low dimensional materials and semiconductor nanostructures, their structure and gives a summary of growth techniques. This chapter starts with the physics behind semiconductor heterostructures and low dimensional system, i.e., quantum wells, wires and dots, explaining how quantum confinement leads to modification of band structure and density of states. Also growth modes of heterostructure semiconductors and critical thickness in the growth of lattice mismatched structures are briefly described. In section 3.4 Frank-van der Merwe, Volmer-Weber and Stranski-Krastanow growth modes are explained. QD formation mechanism and NC growth in matrix are briefly described in sections 3.5 and 3.6. Molecular beam epitaxy, ion implantation, sputtering growth techniques to provide the materials is discussed in the final section of chapter 3.

Chapter 4 includes experimental results for the Ge-NCs in alumina samples. After a brief introduction and description of samples in the opening of this chapter XRD results and discussions related to these experiments are highlighted and the relationship between XRD results and structural properties of the two main samples are described. Section 4.4 is dedicated to findings of Raman spectroscopy regarding the existence of strain in the samples through shifts in the Raman spectra of the sample with the bigger NCs size. Conventional dark field and bright field transmission electron microscopy (TEM) results are illustrated in section 4.5 and the existence of crystalline Ge in alumina matrix is evidenced by dark field TEM images. HRTEM images of the matrix including Ge NCs are presented in section 4.6 and the possibility of utilization of Fourier method to study the strain in the bigger NCs is discussed.

Chapter 5 is dedicated to the InAs/GaAs structure, and experimental results of this material are presented. After an introduction and explanation of the sample architecture PL, XRD, conventional TEM, high angle annular dark field (HAADF) and EELS results are presented. In section 5.3 PL results of the sample with and without growth interrupt

and the role of growth interrupt in the optical properties of the sample are discussed. In section 5.4 findings of XRD about the structural properties and arrangements of the samples are presented and evidence of QD formation in the sample with growth interrupt (GI) is presented. Conventional BF and DF TEM images are depicted in section 5.5 and formation of QDs in sample #12 is shown. In this part it emerged that there is no evidence of buried QDs in sample with no GI. Results of STEM including HAADF and EELS are presented in the final parts of this chapter, and qualitative elemental maps are provided using a state of the art STEM (SuperSTEM II). The KK method is applied to extract the imaginary part of the dielectric function as powerful analytical approach to provide high resolution elemental maps in section 5.3. The well known GPA method has been employed to examine HRTEM images and provide strain maps in order to extract compositional information of sample XMBE#12 in section 5.4.

Er and Si-NCs doped silica samples are the cases under investigation in chapter 6. After an introduction to the topics and presentation of the schematics of the samples, PL results of the three main samples including solely Er doped silica, Er and Si co-implanted and annealed silica, and sequentially Er and Si implanted and annealed silica samples are discussed, including the role of Si and of the growth/implantation sequences in the optical properties and the 1.54 μm emission intensity. The next section emphasizes TEM, HRTEM, HAAD and EELS results of the silica sample co-implanted with Er and Si. TEM and HRTEM images of this sample acquired in a Tecnai FEG30 instrument are illustrated and the formation of NCs in silica matrix has been proven. HAAD images of the sample taken with SupeSTEM II are presented and O, Si and Er elemental maps presented. The spatial correlation of Er, Si and O and the role that excess Si plays in the agglomeration of Er as a shell surrounding NCs is highlighted. In the next section of this chapters (6.5) structural and compositional properties of solely Er doped silica sample are discussed and qualitative elemental maps of Er and O presented. In the final section of this chapter results of sequentially Er and Si implanted and annealed systems are evaluated. HAAD, HRTEM and EELS measurements were employed to study the structure and composition of this sample and results are presented. The composition of the matrix is investigated via the Er, Si and O signal to

give an understanding of the difference in the optical properties of this sample in comparison to the co-implanted sample.

Chapter 7 provides valence band EELS investigation to address the composition- and structural relationship of Er and Si-NCs, especially regarding the possibility of Er-silicide phase formation in the co-implanted sample, where strict co-location of Er and NCs was observed. In the final chapter an overall conclusion is drawn, followed by some recommendations for prospective future work.

2

Characterization Techniques and Methods

2.1 Interaction of electrons with matter

When high energy electrons hit a specimen they can be scattered elastically, without energy transfer to the sample, or inelastically by transferring energy to the sample. As a result of inelastic interaction cathodoluminescence, X-ray, and back scattered, Auger and secondary electrons may be produced. Figure 2.1 shows a schematic diagram of interactions of high energy electrons with the sample resulting in the production of electrons and electromagnetic waves.

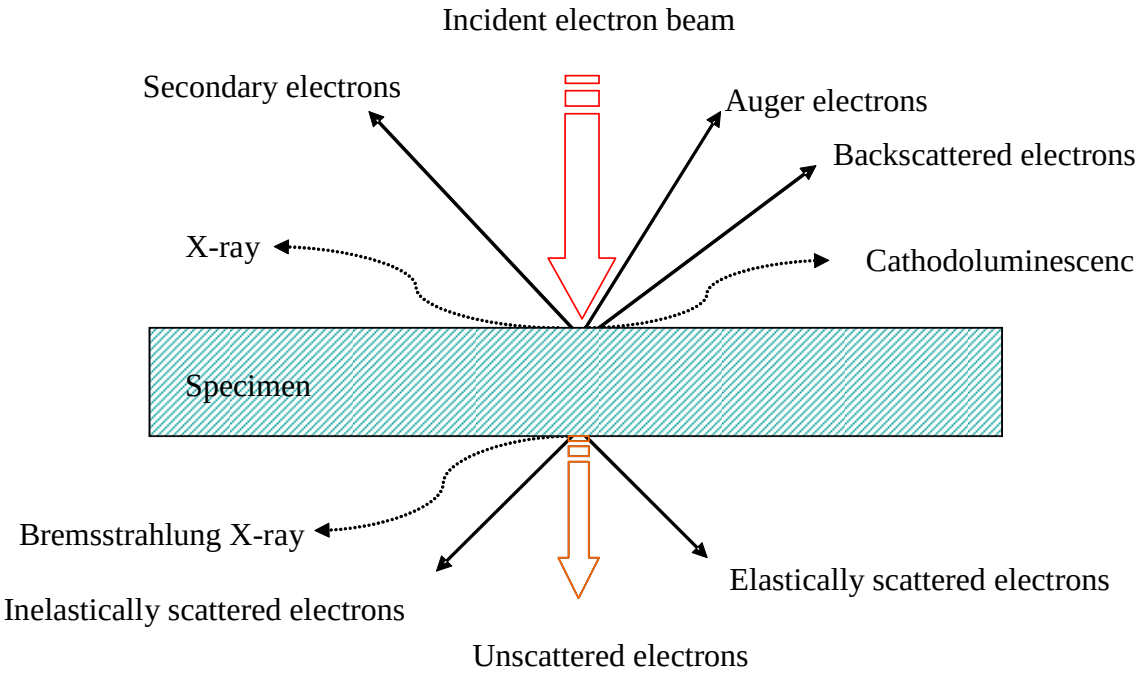

Figure 2.1 Interaction of electron beam and sample (D.B Williams)

Elastically and inelastically scattered as well as unscattered primary electrons are used to extract high resolution structural and compositional information of thin samples in a TEM or a dedicated scanning transmission electron microscope (STEM). Spatial resolution is the most important factor when imaging materials on the nano-scale. The spatial resolution of current state of art TEM instruments is about 1 million times better than that of the human eye and about ten thousands times that of the best current optical microscopes. The resolution of current TEMs is about a few angstroms which makes TEM a powerful investigation technique on the atomic scale. Despite some draw backs for the TEM: small sampling area, artefacts and interpretation of the images, structural and compositional changes during sample preparation and sensitivity of materials to the electron beam resulting in damage, it is the most powerful and useful machine in the study of nanostructured materials.

2.2 TEM

A TEM consists of illumination and imaging systems. The illumination system in standard operation mode launches a nearly parallel beam of electrons on the specimen

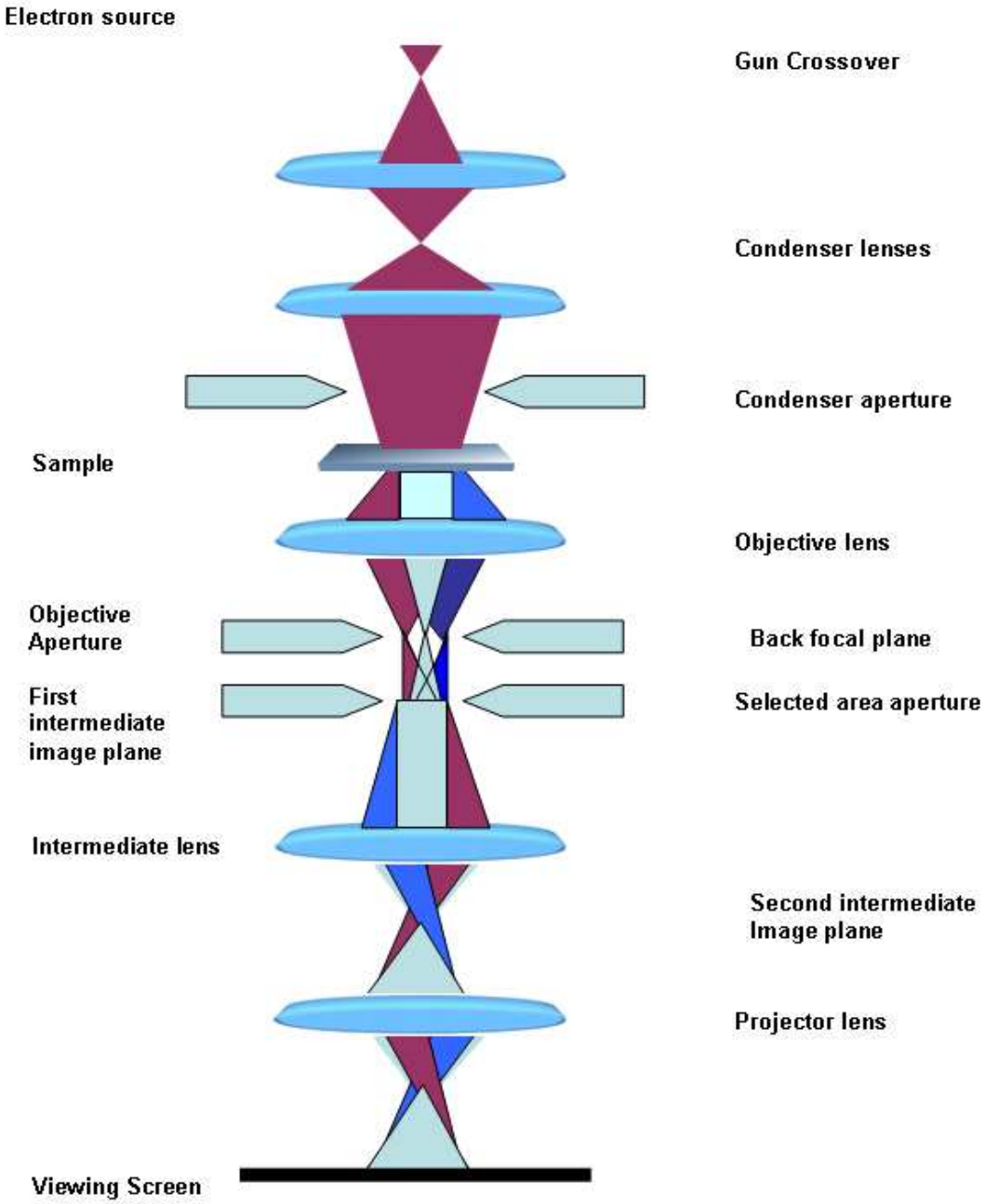

Figure 2.2 The electron optics and configuration of a TEM. A series of apertures and lenses are used to focus accelerated electrons to a nearly parallel beam on the sample. The beam is magnified by a series of lenses and viewed on the viewing screen or detected by CCD or TV.

by using apertures and magnetic lenses. There are two types of electron source, the field emission gun (FEG) as used in the Tecnai, and the thermionic source (heated filament) as in the Philips CM200 in this study. The condenser lenses illuminate the specimen by using the image of the gun cross over as the object. The size of the beam on the sample is normally on the order of several micrometers for medium magnifications (20-100 kX). A more parallel beam gives better coherence and is well suited for diffraction studies. The imaging system collects transmitted electrons by magnetic lenses and apertures and directs the electron beam toward a viewing screen to produce an image or diffraction pattern. The objective lens produces a diffraction pattern from the transmitted electrons in the back focal plane of the microscope. A selected area aperture, inserted in the first image plane is used to provide diffraction patterns of specific areas of the sample. The direct beam is selected for bright field imaging by inserting an objective aperture in the back focal plane. The aberration of objective lens can to a certain extent be controlled by the size of objective aperture which controls the collection angle, β. The magnification is controlled by the strength of the intermediate lenses. The magnified diffraction pattern or image can be viewed on a ZnS coated viewing screen or detected by charged-coupled device- or TV-cameras set below the viewing screen. Figure 2.2 shows the optics and schematics of a TEM.

2.3 Image contrast in TEM

There are three contrast mechanisms in the TEM.

i) Mass-thickness contrast: Regions of specimen with high thickness and/or high atomic number species scatter electrons into higher angles which are then deflected away of the optical axes of the microscope. By inserting a small objective aperture these beams are blocked and higher thickness and/or high atomic number area of the specimen appear darker in BF and brighter in DF images, whereas regions with low thickness and/or low atomic number scatter electrons into lower angels and are the origin of high intensity regions in the BF and vice versa in DF images.

ii) Diffraction contrast: When the size of objective aperture is chosen so as to exclude the diffracted beams, the resulting contrast is diffraction contrast. This is employed for

low-resolution defect studies; In this case the image is sensitive to changes in specimen thickness, distortions of the crystal lattices due to defects, strain and bending.
iii) Phase contrast: If there is no objective aperture or the size of it is chosen as to allow many diffracted beams to pass through, the main contrast mechanism is phase contrast, enabling high resolution TEM (HRTEM) imaging. When electrons are scattered their phase changes. These changes in phase depend on the atomic structure of the sample (atomic potential). The variation of the atomic potential produces the phase change.

2.4 High Resolution Transmission Electron Microscopy (HRTEM)

Phase contrast imaging is an effective technique to study defects, grain boundaries, interfaces and changes in lattice structure of a material at atomic resolution. Phase contrast imaging is performed in a TEM by aligning the electron beam parallel to one of the zone axes of the specimen whilst removing or inserting a big objective aperture to include both, transmitted and scattered electrons of a thin specimen. Intuitively explained the contrast in the images results from interference of scattered and transmitted beams of electrons. Interference of each pair of beams will give rise to a series of fringes in the image plane. Contributions of more diffracted beams of electrons will result in intersecting lattice fringes and appearance of spots at the intersection points. These spots in ideal circumstances can be expected to be located at positions of atomic columns.
However, this is a simplification, because the phase of a complex function (like the electron wave function) is not preserved upon squaring (to obtain the intensity) and hence would not affect image contrast. Intensity in HREMs acquired in a microscope with perfect lenses is constant and lens imperfections could cause intensity variation throughout the image.

Apertures and aberrations of lenses in the imaging system affect the electron beam passing through the microscope. These effects can be described by a complex contrast transfer function (CTF), acting upon the exit wave. The mathematical outcome of this process is an altogether real function, containing the phase. This means that now the

phase information is ‘preserved’ upon squaring, i.e., it shows up in the intensity. The CTF for a thin sample can be written as:

$$CTF(u) = A(u)E(u)\sin(\chi(u)) \quad (2.1),$$

where u is the spatial frequency of the electron beam and high spatial frequencies corresponds to large distances from the optic axis in the diffraction pattern. The A(u) is the aperture function, E(u) the envelope function describing the attenuation of the exit wave, and aberrations of the electron optics system are represented by $\chi(u)$. $\sin(\chi(u))$, the sinusoidal term determines the sign (negative, dark or positive, bright) of the image contrast. The function $\chi(u)$ depends on the spherical aberration C_S, the defocus Δf and the wavelength of the electrons:

$$\chi(u) = \frac{\pi}{2} 2\ C_S \lambda^3 u^4 + \pi\ \Delta f\ u^2 \quad (2.2)$$

The envelope function, which is a product of specimen drift, angular spread of the electron source, specimen vibration, chromatic aberration and detector performance, describes the attenuation of the exit wave. The specimen vibration and drift can be minimised by providing suitable working environment. Spherical aberration limits the spatial resolution and chromatic aberration and current and voltage instabilities determine the stability of the microscope.

2.5 Geometric Phase Analysis (GPA)

Hÿtch et al. [12] developed a method to study strain by analysing HREM images, known as the GPA. In this section [12] the principle of the GPA is described. An HREM image of a crystalline structure is assumed to be constructed of sets of periodicities. Every periodicity has a related Fourier component, which is a function of position. For a perfect crystalline structure these Fourier components will appear as sets of periodicities related to Bragg reflections. Indeed a HREM image of a crystalline structure is never perfect due to changes in the imaging condition and inhomogeneities in the crystallinity of the sample. The intensity of Bragg spots in the Fourier transform of the image in such circumstances will be diffuse due to changes in the structure caused by defects, strain, grain boundaries, etc. The GPA is a method to gain a better

understanding of the position and distribution of defects, shape of grains, strain distribution, lattice distortion and deviations from a perfect lattice in real space. A HREM image of a perfect crystal can be expressed as:

$$I(r) = \sum_{\mathbf{g}} H_{\mathbf{g}} \exp\{2\pi i\, \mathbf{g}.\mathbf{r}\} \quad (2.3)$$

Where I(**r**) is the intensity of the image at the position r, and g is the periodicity of corresponding Bragg reflection. H_g is the complex Fourier coefficient:

$$H_g = A_g \exp\{iP_g\} \quad (2.4)$$

Where A_g is the amplitude and P_g is the phase.
If we consider the Fourier components as a function of position in the image, H(r), we will have:

$$I(r) = \sum_{\mathbf{g}} H_{\mathbf{g}}(\mathbf{r}) \exp\{2\pi i\, \mathbf{g}.\mathbf{r}\} \qquad (2.5)$$

By using (2.3) in (2.4) and considering conjugate symmetry of Fourier components the following equation for I(r) is obtained; because I(r) is a real function, the complex parts should cancel in pairs, leaving the following expression:

$$I(r) = A_0 + \sum_{g>0} 2A_g(r) \cos\{2\pi \mathbf{g}.\mathbf{r} + P_g\} \quad (2.6)$$

By masking a specific **g** position in the Fourier transform the image will be a set of lattice fringes, the contribution $B_g(r)$ to the image can be written as:

$$B_g(\mathbf{r}) = 2A_g(r) \cos\{2\pi \mathbf{g}.\mathbf{r} + P_g\} \quad (2.7)$$

In the presence of a displacement field u, so that r→ r-u, we can rewrite equation (2.7) as:

$$B_g(\mathbf{r}) = 2A_g(r)\cos\{2\pi\mathbf{g}.\mathbf{r} - 2\pi\mathbf{g}.\mathbf{u} + P_g\} \quad (2.8)$$

This results in a change in the phase of:

$$P_g(\mathbf{r}) = -2\pi\mathbf{g}.\mathbf{u} \quad (2.9)$$

By selecting two non-collinear Bragg spots in the Fourier transform pattern, g1, and g2, and knowing that:

$$\mathbf{g}_1 = g_{1x} + g_{1y} \quad (2.10)$$

$$\mathbf{g}_2 = g_{2x} + g_{2y} \quad (2.11)$$

The phase change vector becomes:

$$P_{\mathbf{g}1}(\mathbf{r}) = -2\pi\ \mathbf{g}_1. \quad = -2\pi\{g_{1x}u_x(r) + g_{1y}u_y(r)\} \quad (2.12)$$

$$P_{\mathbf{g}2}(\mathbf{r}) = -2\pi\ \mathbf{g}_2. \quad = -2\pi\{g_{2x}u_x(r) + g_{2y}u_y(r)\} \quad (2.13)$$

This can be written in form of a matrix:

$$\begin{pmatrix} P_{\mathbf{g}1} \\ P_{\mathbf{g}2} \end{pmatrix} = -2\pi \begin{pmatrix} g_{1x}\ g_{1y} \\ g_{2x}\ g_{2y} \end{pmatrix} \begin{pmatrix} u_x \\ u_y \end{pmatrix} \quad (2.14)$$

For the displacement field we can show that:

$$\begin{pmatrix} u_x \\ u_y \end{pmatrix} = \frac{-1}{2\pi} \begin{pmatrix} g_{1x}\, g_{1y} \\ g_{2x}\, g_{2y} \end{pmatrix}^{-1} \begin{pmatrix} P_{g1} \\ P_{g2} \end{pmatrix} \quad (2.15)$$

By defining a two dimensional lattice with lattice vectors a_1 and a_2 and their reciprocal vectors g_1 and g_2 we can write their relationship with these equations:

$$\mathbf{a}_1.\mathbf{g}_1 = \mathbf{a}_2.\mathbf{g}_2 = 1 \quad (2.16)$$

$$\mathbf{a}_1.\mathbf{g}_2 = 0\,,\ \mathbf{a}_2.\mathbf{g}_1 = 0 \quad (2.17),$$

And their matrix form as:

$$\begin{pmatrix} g_{1x}\, g_{1y} \\ g_{2x}\, g_{2y} \end{pmatrix} \begin{pmatrix} a_{1x}\, a_{2x} \\ a_{1y}\, a_{2y} \end{pmatrix} = \begin{pmatrix} 1 & 0 \\ 0 & 1 \end{pmatrix} \quad (2.18)$$

Equation 2.15 then becomes:

$$\begin{pmatrix} u_x \\ u_y \end{pmatrix} = \frac{-1}{2\pi} \begin{pmatrix} a_{1x}\, a_{1y} \\ a_{2x}\, a_{2y} \end{pmatrix} \begin{pmatrix} P_{g1} \\ P_{g2} \end{pmatrix} \quad (2.19).$$

The strain is defined as:

$$e = \begin{pmatrix} e_{xx}\, e_{xy} \\ e_{yx}\, e_{yy} \end{pmatrix} = \begin{pmatrix} \frac{\partial u_x}{\partial x} & \frac{\partial u_x}{\partial y} \\ \frac{\partial u_y}{\partial x} & \frac{\partial u_y}{\partial y} \end{pmatrix} \quad (2.20)$$

and can hence be expressed as:

$$e = -\frac{1}{2\pi}\begin{pmatrix} a_{1x} & a_{1y} \\ a_{2x} & a_{2y} \end{pmatrix}\begin{pmatrix} \frac{\partial P_{g1}}{\partial x} & \frac{\partial P_{g1}}{\partial y} \\ \frac{\partial P_{g2}}{\partial x} & \frac{\partial P_{g2}}{\partial y} \end{pmatrix} \quad (2.21)$$

From this equation and by using the relation between local distortion and strain:

$$\varepsilon = \frac{1}{2}\{e + e^{T}\} \quad (2.22)$$

The strain field is then computable.

In the GPA method the strain is calculated as a relative distortion with respect to a reference crystal which is the Euler representation of strain and is different from the Lagrange representation of strain; the two expressions are:

$$e_E = \frac{a_l - a_s}{a_l} \quad (2.23)$$

and

$$e_L = \frac{a_l - a_s}{a_s} \quad (2.24)$$

In this research GPA was performed to study strain distributions and compositions of the InAs/GaAs QDs.

2.6 Scanning Transmission Electron Microscopy (STEM)

The principal of a STEM is very similar to a TEM in that both use transmitted beams of electrons to acquire information and images of thin samples. However the ray path of the electron beam in a STEM is the reverse of that in a TEM. Figure 2.4 shows a simple schematic diagram of a STEM. A cold field emission gun (G) produces a beam of electrons which is focused by electromagnetic lenses (L) onto a sample (S). The beam is

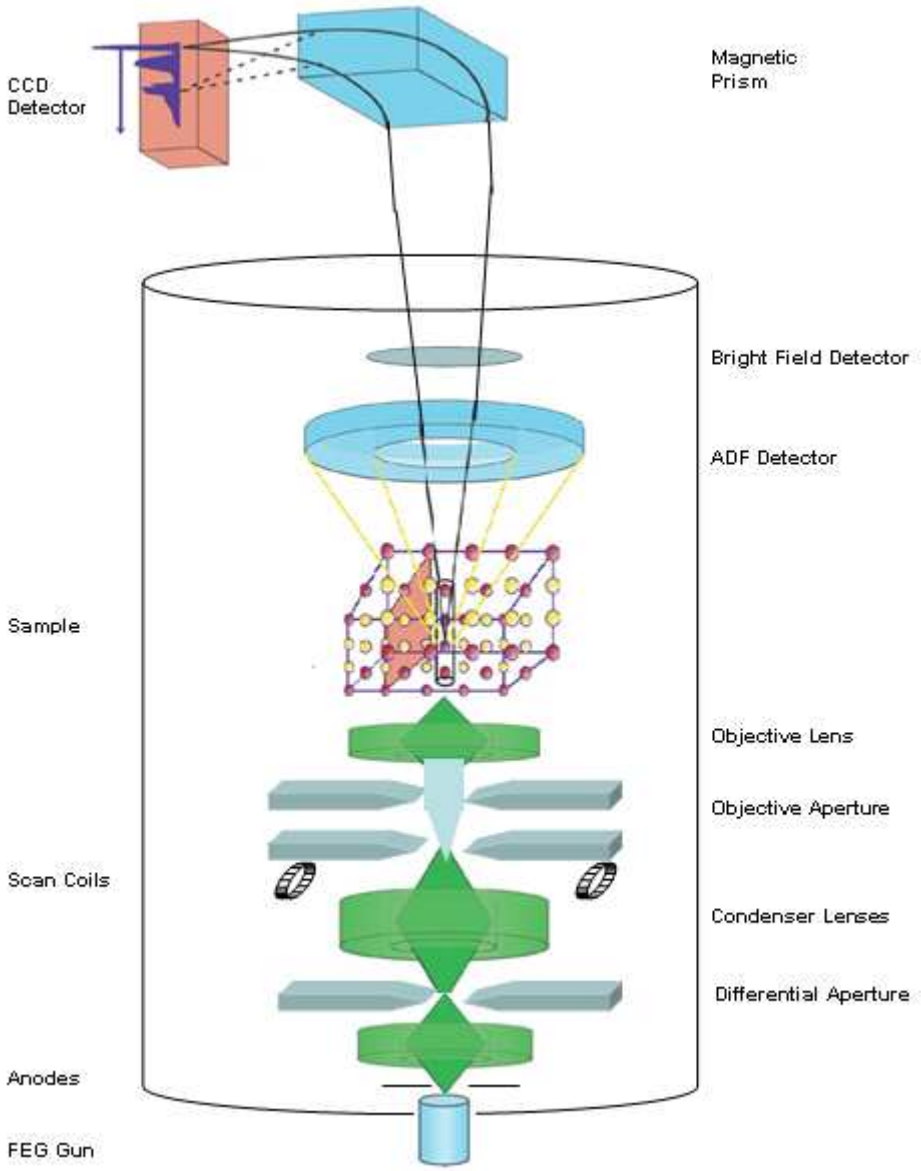

Figure 2.3 Electron optics and configuration of a STEM. A series of apertures and lenses are used to focus and scan accelerated electrons by user defined parameters on the sample. The data is collected by a BF and HAADF detector and/or an EELS spectrometer.

scanned over the sample by scan coils in a raster. The objective lens plays the same role as in the TEM and controls collection angle of electron beam. The magnification is changed by the objective lens via altering the raster size (e.g. the area of scan). The data collecting part is similar to that in the TEM and is located above the sample consisting

of an energy electron loss (EELS) spectrometer, a BF detector and a high angle annular dark field (HAADF) detector, which detects electrons scattered into high angles (>50 mrad). Other data collecting units like an energy dispersive X-ray (EDX) detector can also be annexed. In this research thinned cross-sectional samples were examined using an aberration-corrected STEM at the Daresbury SuperSTEM laboratory. This instrument is a 100 keV machine with a VG HB501 vacuum system employing a cold-field emission source, a high-resolution pole piece, and the Nion Mark II spherical aberration corrector. The angular range of the HAADF detector is 70 - 210 mrad. The STEM is also equipped with a Gatan Enfina EELS system.

2.7 Electron Energy Loss Spectroscopy (EELS)

Elastic scattering of incident electrons is employed for structural characterisation of materials. On the other hand inelastically scattered electrons are used for analytical

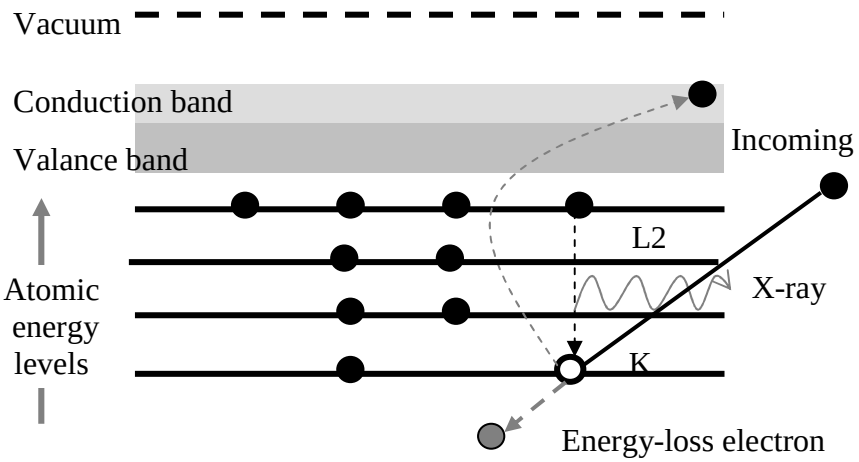

Figure 2.4 Schematic diagram of the ionization process. An inner-shell electron is targeted by a high energy electron and ejected from the atom. The scattered electron beam has lost a specific amount of energy and a characteristic x-ray is emitted as a result of the occupation of the free energy level by an upper shell electron

TEM and STEM investigations to gain information about chemical species and their distribution within the sample.

In EELS quantitative information of thin foils of material is obtained from inelastically scattered electrons, which have lost specific amounts of energy: these energy losses of incident high energy electrons occur due to interaction with the electron cloud surrounding atomic nuclei (figure 2.5). A magnetic prism and spectrometer inserted after the BF detector in a STEM, disperses the transmitted electrons from the specimen in terms of their energy before they enter a fibre-optic-coupled CCD detector array.

The most prominent feature in an EEL spectrum is the zero-loss peak arising from elastically scattered and unscattered transmitted high energy electrons. The different interactions responsible for energy losses of transmitted electrons are: Phonon excitation, outer-shell and inner-shell single-electron excitations and collective oscillation of the conduction and valance band electrons called plasmon. Energy losses because of phonon excitations are ~0.02 eV, which is below the resolution limit of current, conventional spectrometers. Inner-shell tightly bound electrons, by absorbing energies greater than the difference between their ground state energy and Fermi level, can move upward to unfilled states near Fermi level and the colliding high energy (100keV) electrons lose the same amount of energy and are scattered with a scattering angle of the order of 10 mrad [13]. Single-electron excitations are also probable for outer-shell weakly bound electrons. In the case of a semiconductor or an insulator a valence electron passes through the band gap, whereas for metals it happens via transition to a higher state within the same energy band. The primary high energy electrons will lose a few eV and will be scattered through 1-2 mrad. The primary electrons can also be scattered inelastically by production of collective excitation modes of conductive or valence band electrons. For the case of a free electron gas (like in a metal) the quantum energy of the longitudinal wave is [14]:

$$E_p = \hbar\omega_p = \hbar\left(\frac{ne^2}{m\varepsilon_0}\right)^{1/2} \quad (2.1),$$

where, ħ is Plank's constant, ω_p is plasmon frequency n is valence or conduction electron density,ε_0 is permittivity of free space, and e and m are the charge and mass of the electron, respectively. E_p is in the range of 10-30 eV for the majority of solids and, for 'bulk' materials often has a direct relationship with the square root of the conduction-electron density, n, as illustrated above. Two kinds of plasmon excitation, bulk and surface, are produced and a combination of surface and volume losses can be observed as several loss peaks in the EELS spectrum.

The plasmon peaks in some materials are in a similar energy regime to the losses of N and O shells; hence resolving these edges becomes difficult. In this research Er O in Er doped Si-NCs in silica and In N in InAs/GaAs QDs structures were dominated by plasmon peaks. Beyond the low-loss region (up to 50 eV) the spectrum intensity decreases smoothly.

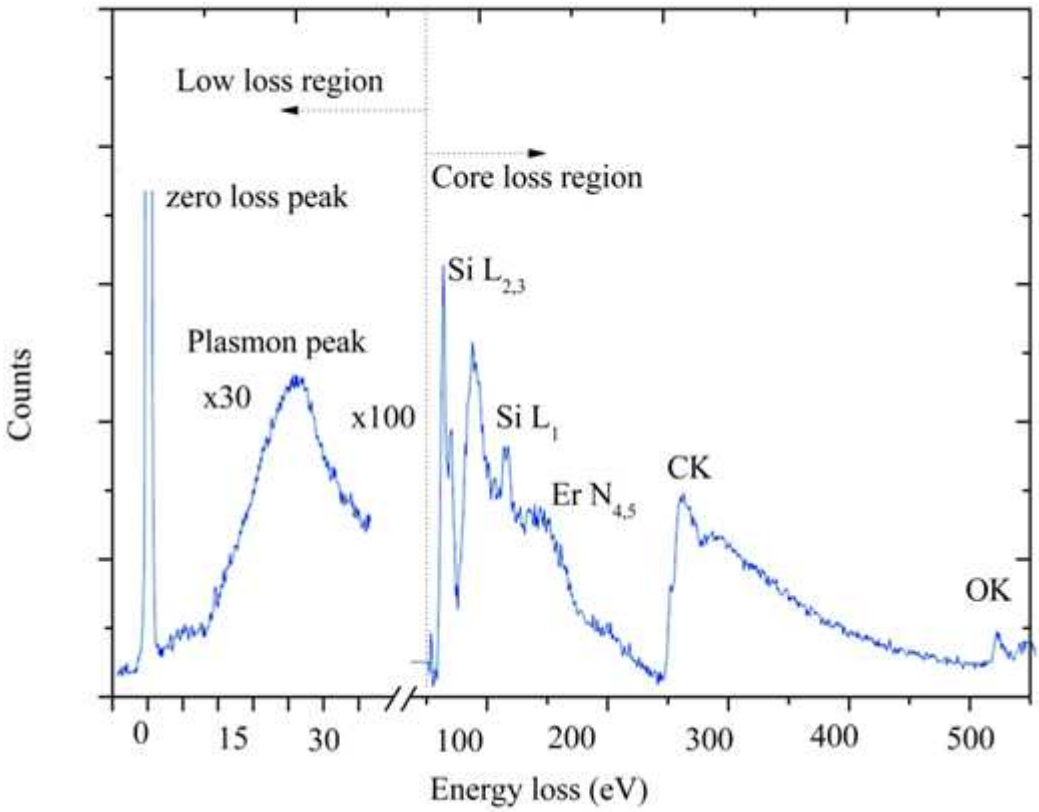

Figure 2.5 Energy loss regions of the EELS spectrum with assigned features

The features superimposed on the background intensity (the background intensity originates from the multiple inelastic scattering of high energy electrons and extension of previous edges) have the shape of edges, which rise sharply and fall slowly. These edges represent inner-shell characteristic excitations of the species responsible for the inelastic scattering. This region of the spectrum starts from tens of eVs and extends to thousands of eVs. This region of the spectrum is known as the high loss or core loss region.

In this report a Gatan Digital Micrograph (DM) software has been used to analyse the EELS spectra and EEL spectrum images (SIs).

2.7.1 Electron energy loss spectrum imaging

Figure 2.7 is a schematic representation of the spectrum imaging technique [15-17] in a STEM which provides a SI by stepping a focused electron probe from one pixel to the next. SIs contain EEL spectra recorded over a user-defined energy range and area (with sample thickness <30nm). A HAADF image can be obtained simultaneously. By this definition one can say that a spectrum image is a 3D image, containing 2D spatial information of the sample and the EEL spectrum in the third dimension. (In fact they are four dimensional data sets: two spatial-, one energy- and one intensity-coordinate). [15] Batch collection of EEL spectra over every single pixel of the selected area makes post-operation processing possible. This post-operation processing capability is the major advantage of the SI technique over the energy filtered transmission electron microscopy (EFTEM) and other analytical TEM techniques. In order to obtain optimum data quality of an SI in terms of spatial resolution and signal to noise ratio the pixel number and dwell time per pixel have to be negotiated: a longer dwell-time produces more counts but can be adversely affected by drift, contamination accumulation and beam damage. A high number of small pixels result in better spatial resolution and possibly reduced damage, but also in more contamination. The other user defined value for SI acquisition is the energy dispersion (eV/ch). The dispersion can be specified depending on the energy range of the EEL spectra. For example for extracting low loss or core-loss fine structure information, an energy dispersion of ~0.01-0.05 eV/ch is

useful, whereas including signals from a number of elements in one SI often requires dispersions of 0.3-1 eV/ch

The full width half maximum (FWHM) of the zero loss peak (ZLP) is often taken to represent the energy resolution of spectra. The position of the ZLP is used to calibrate the low loss spectra. For calibration of the core loss spectra the most popular and reliable feature is the π* peak of the C K-edge in the EEL spectra at ~285 eV. In this research the C K π* peak was used to calibrate the EEL spectra.

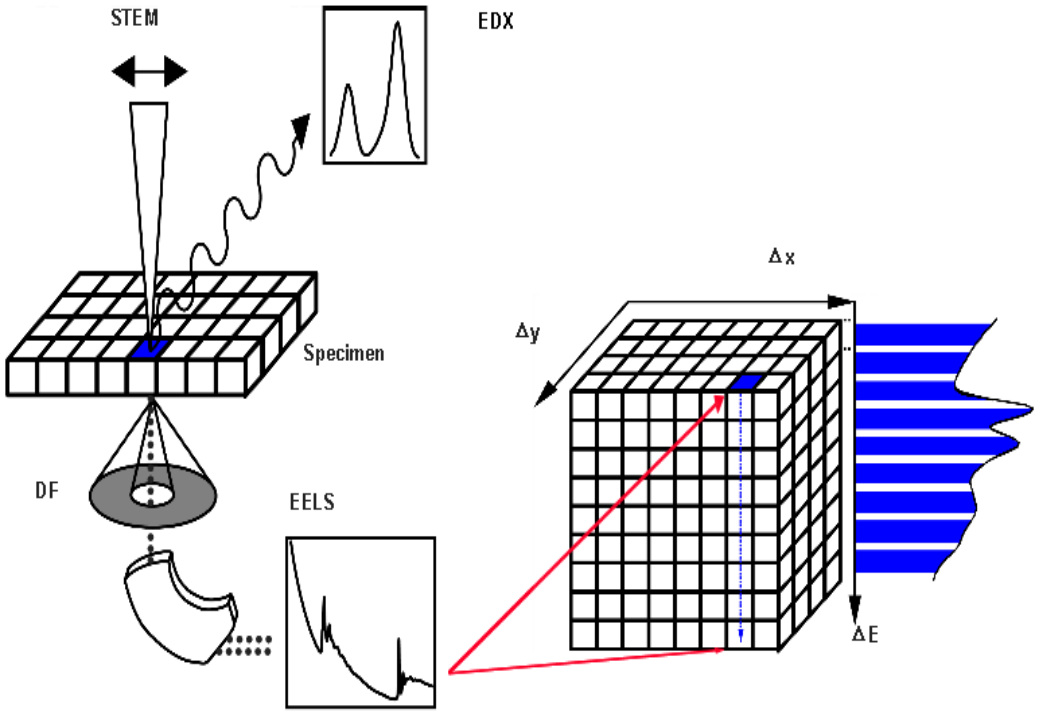

Figure 2.6 STEM spectrum image acquired by stepping a focused electron probe from one pixel to the next [15].

2.7.2 Non-Linear Least Square (NLLS) fitting

Analysis of spectral features (e.g. white line peaks) in EELS spectra by fitting single or multiple Gaussian models and by characterizing them by means of FWHM, amplitude and central dispersion of a fitted Gaussian peak can be performed by using the NLLS (non linear least square fitting) sub-menu in the Gatan DM software. Applying this fit to

the whole SI facilitates mapping of Gaussian model parameters in specified areas of the sample, and can for example reveal information about local bonding- and oxidation states via, e.g., width and position of the Gaussian. This method is described in more detail in the following and will be re-visited later in the result section.

As illustrated below a single spectrum can be selected from the SI by using spectrum picker tool. After selection of the region of interest (ROI) on the spectral feature NLLS fitting can be executed, and maps of values for the energy centre, the FWHM and intensity of the peak can be obtained. These outputs reveal characteristics of chemical phases in the SI area of the sample. Figure 2.8 shows details the NLLS fitting of the plasmon peak in the low loss region of an InAs/GaAs QD sample. The colour map (right) is the energy of the plasmon peak with yellow and red colours indicating higher plasmon energies for the GaAs phase and blue colours lower plasmon energies for the InAs phase.

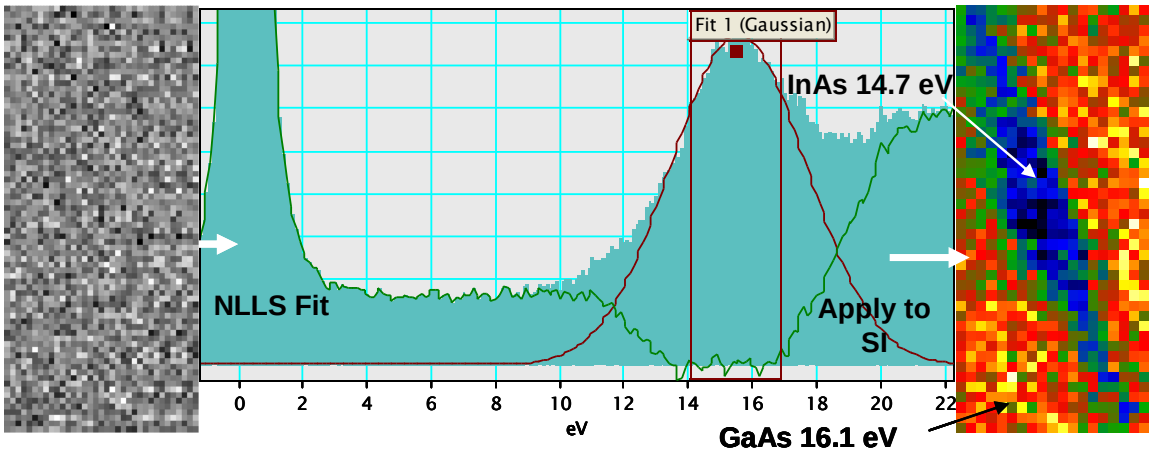

Figure 2.7 Plasmon energy mapping using NLLS applied to an SI obtained of an InAs/GaAs QD structure (left). The Gaussian fit to the plasmon peak provides a value for the plasmon energy (centre). On the right is the corresponding map of energy values, showing clearly the individual phases .

2.7.3 Kramers-Kronig (KK) Analysis

For analysing low-loss EEL spectra, removal of plural scattering and ZLP is a prerequisite. The single scattering distribution in the absence of surface effects is given as [13]:

$$S(E) = K\,\mathrm{Im}[\tfrac{-1}{\varepsilon(E)}]\ln[1+\tfrac{\beta^2}{\theta_E^2}] \quad (2.2)$$

Where K is a constant related to the speed of the primary electron, the intensity of zero-loss peak and the thickness of the specimen, S(E) is the single scattering distribution, θ_E and β are the characteristic scattering and effective collection angles respectively. K may be computed from the sample thickness, the primary electron beam energy, the zero loss intensity, θ_E and β. After computing K, the energy loss function, $\mathrm{Im}[\tfrac{-1}{\varepsilon(E)}]$ is retrievable from the single scattering distribution, S(E). Assuming that the sample is isotropic a KK transformation can be applied to obtain the function $\mathrm{Re}[\tfrac{1}{\varepsilon(E)}]$ from $\mathrm{Im}[\tfrac{-1}{\varepsilon(E)}]$:

$$\mathrm{Re}[\tfrac{1}{\varepsilon(E)}] = 1 - \frac{2}{\pi} P\int_0^\infty \mathrm{Im}[\frac{-1}{\varepsilon(E')}]\frac{E'dE'}{E'^2 - E^2} \quad (2.3),$$

where P represents the Cauchy principal part of the integral to avoid singularities at E′=E. ε_1 and ε_2, the real and imaginary parts of the dielectric function can be evaluated from the relationship:

$$\varepsilon(E) = \varepsilon_1(E) + i\varepsilon_2(E)\frac{\mathrm{Re}[\frac{1}{\varepsilon(E)}] + i\,\mathrm{Im}[\frac{-1}{\varepsilon(E)}]}{\{\mathrm{Re}[\frac{1}{\varepsilon(E)}]\}^2 + \{\mathrm{Im}[\frac{-1}{\varepsilon(E)}]\}^2} \quad (2.4).$$

In DM plural scattering is removed from a low loss spectrum by applying a Fourier-log routine. By applying the K-K analysis routine the energy loss function is extracted and then the imaginary and real parts of dielectric function. As will be explained in the

result section, K-K analysis can be conveniently used to extract low-lying absorption edges (e.g., M and N edges), which are notoriously obscured by plasmons, from the imaginary part of the dielectric function, rather then from the EEL spectrum directly.

2.7.4 EFTEM

EELS provides an energy loss spectrum, whereas EFTEM generates an energy filtered image produced by electrons of a certain energy loss. For this intention, a slit is placed after a magnetic prism to allow electrons with the particular energy loss to contribute to the image formation. The width of the slit defines the resolution and intensity of the data. Elemental maps can be produced by selecting electrons with an energy loss related to an edge of a particular element and maps can be produced with brighter regions in the map corresponding to higher concentration of the element. In order to correct for thickness effects and interference of close-by lower energy edges, it is necessary to remove the background (by using two pre-edge images) or to create jump-ratio maps (by dividing a post-edge by a pre-edge image).

2.8 Photoluminescence (PL) Spectroscopy

If a semiconductor material is exposed to light with energy larger than the band gap, electrons in the valence band are excited to higher energy states in the conduction band and form electron-hole pairs. These excited electrons will quickly relax to the lowest energy states of the conduction band (near the edge of the conduction band) by producing phonons. The relaxation towards the edge of the conduction band is known as thermalisation. An Exciton is a quasi-particle and consists of a photo-excited electron and a hole bound to each other by the Coulomb interaction. Excitons decay by recombination of electrons and holes and consequently produce photons with a characteristic energy related to the effective band gap of the structure. Figure 2.9 depicts a schematic diagram of the PL instrumentation. As shown a laser source produces a laser beam which is focused on the sample by a lens. PL emission of the sample is detected by a detector through a combination of lenses and a monochromator .After separating PL emissions in terms of wavelength in the detector and amplifying the signal by an amplifier a PL spectrum is obtained. As the band gap of nanostructured

semiconductors is related to their confined dimensions the PL spectrum gives information about the structure of the sample. PL peak intensity, line width and position reveal material quality, homogeneity, size and composition of quantum structures respectively [18]

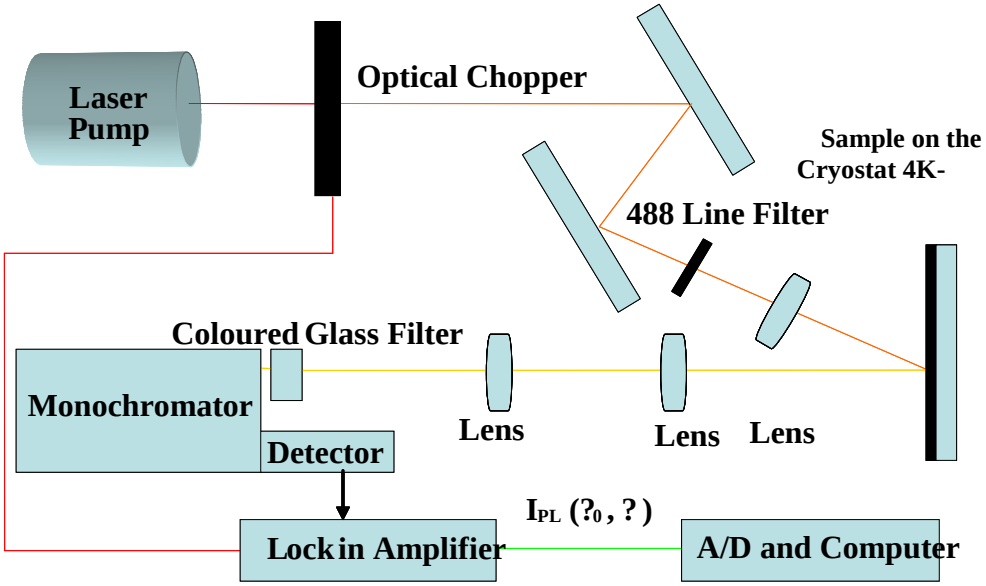

Figure 2.8 Schematic diagram of PL instrumentation [18].

2.9 Double Crystal -Ray Diffraction (DCXRD)

DCXRD is a non-destructive cost effective method which provides a precise assessment of crystallographic properties such as lattice spacings. X-rays with wavelengths of the scale of inter-atomic distances of the crystals (Å) diffract from a high quality perfect reference crystal which is used as a monochromator with lattice constant value close to the substrate of the sample, e.g. germanium with lattice constant of ~0.5646 nm in the case of the InAs/GaAs structure with substrate lattice constant equal to ~0.5653 nm. The diffracted X-rays from the reference crystal hit the sample with an angle of θ as

shown in figure 2.11. According to Bragg's law constructive interference occurs for diffraction angles, θ, equal to Bragg angle:

$$2d\sin\theta = n\lambda \quad (2.5)$$

In the above equation, d, θ, λ, and n are the atomic planes distance, the diffraction angle, the x-ray wavelength and the order of diffraction, respectively.

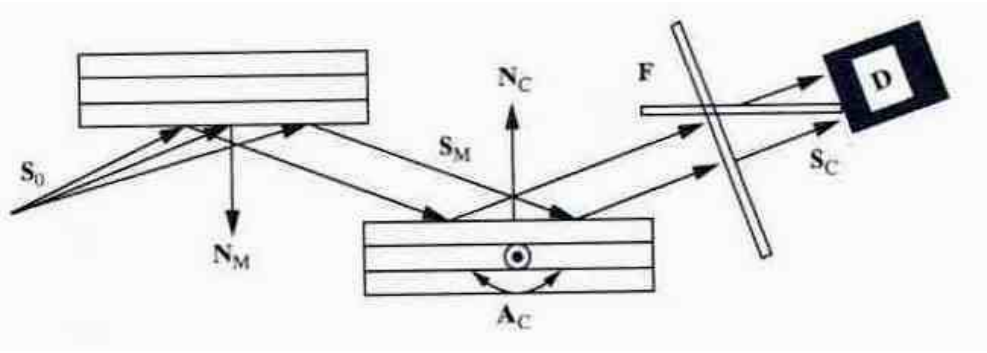

Figure 2.9 Schematic diagram of DCXRD [19]

As the sample is rotating and λ is constant, any change in composition of the grown materials leads to a change in the lattice constant and, according to Bragg's law, in the appearance of the peaks at different angles. As depicted in figure 2.11, there are two kinds of peaks in the XRD rocking curves of the epitaxially grown periodic multi-layer structures, the biggest peak corresponds to the substrate and some of the other peaks with smaller intensities are known as satellite peaks and correspond to the epitaxially grown layers. In each peak two visible features may appears. If the interface is abrupt one large peak related to the thick layer and one additional peak related to the thin layer stack will be visible as indicated with arrows in figure 2.11 the measure of angular differences between these two peaks represents the lattice mismatch.

The appearance of several satellite peaks is indicative of periodicity in the structure. Structural properties like interface and bulk dislocations and stacking faults, give rise to a shift in the positions of the peaks and also to broadening making it possible to

estimate dislocation densities [20]. Also inter-diffusion of layers leads to broadening of the XRD peaks. By using the equation below, the strain and misfit between substrate and film can be calculated [19].

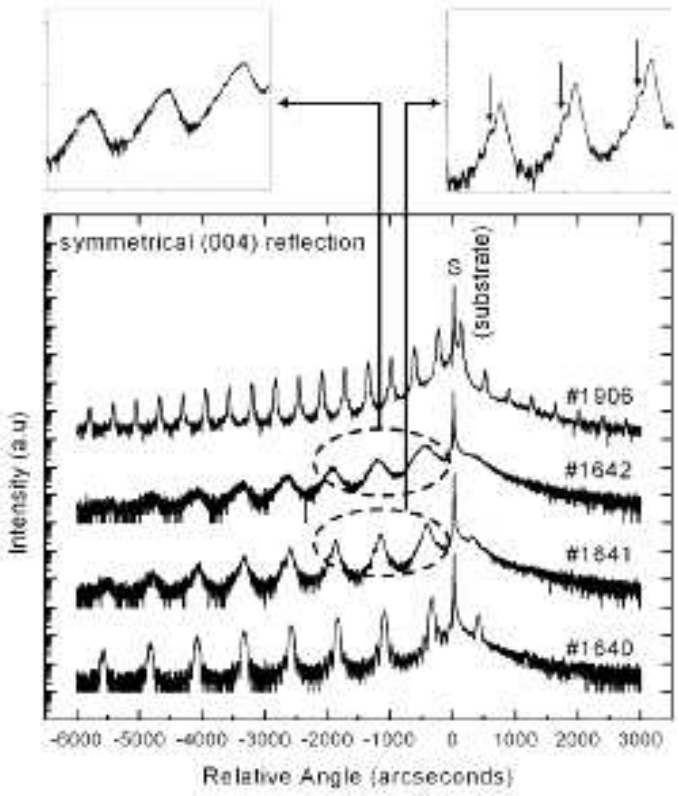

Figure 2.10 DCXRD experimental rocking curve of InAs/GaAs quantum dot samples [1]

$$\varepsilon = \frac{a_s - a_L}{a_l} = \frac{\Delta\theta}{\theta}\cot(\theta_B) \qquad (2.6)$$

In the above equation ε, Δθ and θ_B are the strain, angular difference between big and small peaks in the rocking curve and Bragg angle, respectively.

In this report the structure of the GaAs based samples in chapter 5 was characterised via double crystal x-ray diffraction (DCXRD) using a Bede QC200 diffractometer with a

source of 1.54056 Å wavelength and random polarisation. A Ge crystal was used as a reference crystal for the GaAs substrate, with all measurements being carried out using (004) reflection plane geometry.

2.10 TEM Cross Sectional Sample Preparation

In order to prepare electron transparent cross-sectional TEM samples a sandwich method was employed in this research [21]. Two millimetre wide slices were cut from the wafer with a diamond pen. Two pieces of these slices were glued together face to face with M-Bond 610 epoxy. To support the main sample, slices of the scrap material with similar mechanical properties were sandwiched on either side. Then the assembled structure was clamped and placed in a furnace at 175 ºC for 1 hour to cure the epoxy. Then the sample was ground mechanically down to ~150 µm. In the

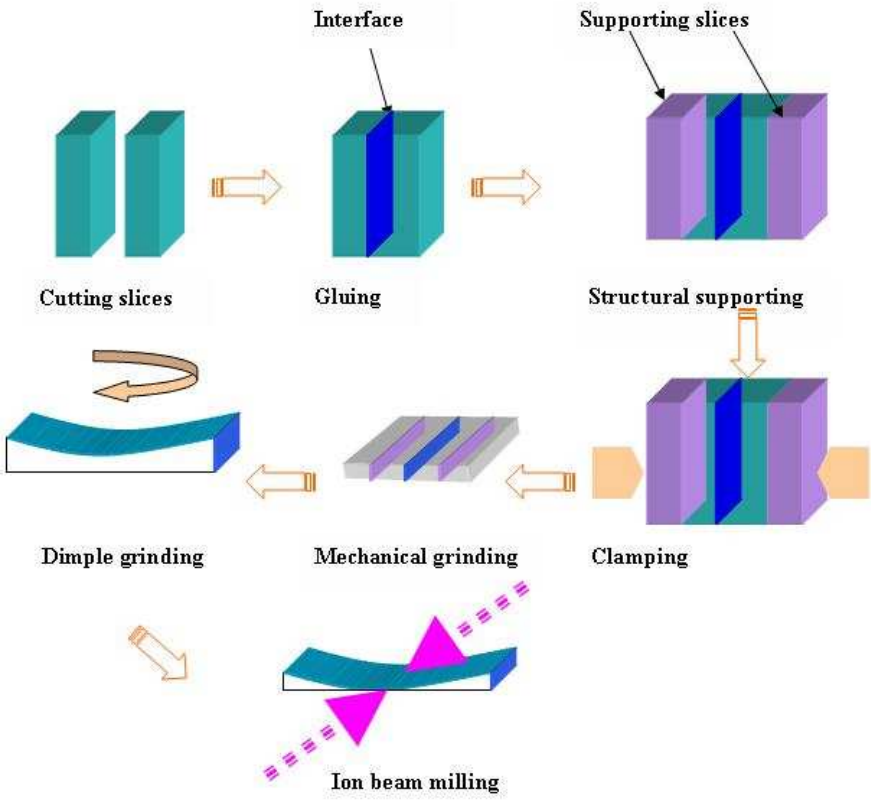

Figure 2.11 Schematic diagram of the cross-sectional sample preparation process.

For the next stage of the thinning process, a GATAN 656 dimple-grinder was used to thin the sample down to ~40 µm. A Gatan 691, Precision ion polishing system (PIPS) was employed to finalize the thinning process by ion milling to produce electron transparent area at the interface. During the milling the energy of the Ar ions and the angle of the incident beams were kept at 6 keV and 5-7 degree respectively. Figure 2.12 shows a schematic diagram of the TEM sample preparation process.

3

Low-dimensional Materials: Concept, Structures and Growth

3.1 Semiconductor Heterostructures

Electrons in an isolated atom have discrete energy levels. As an example the energy levels of an isolated hydrogen atom according to the Bohr model follow the simple relationship [22]:

$$E_H = -13.6/n^2 \, eV \quad (3\text{-}1),$$

where n is the principal quantum number.

If two isolated atoms are brought close together their energy levels will overlap. In a bulk semiconductor the inner shell electrons are strongly bound to the nucleus and the outer shell weakly bound electrons take part in chemical interactions and are called valence electrons with orbital radius bigger than the inter-atomic separation. In a crystal the energy levels of the atoms overlap and consequently bands of energy levels form. These bands are named valence and conduction bands. With particular view to semiconductors electrons excited into the conduction band and the empty spaces (holes) left behind in the valence band behave as free charge carriers and can move freely inside the crystal. Since these charge carriers are affected by the crystal potential their mass is different from the mass of the free electrons and is called the effective mass.

The effective mass of electrons in gallium arsenide and indium arsenide is in the range of 0.01 to 0.1 of that of free electron mass.

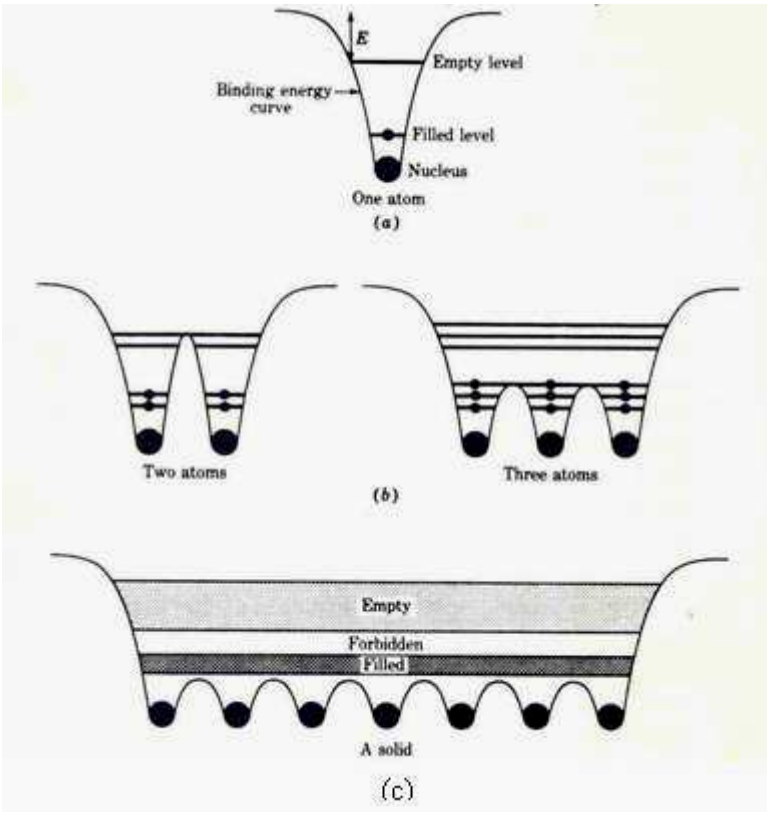

Figure 3.1 Energy levels of (a) one (b) two and three and (c) a combination of atoms and the formation of energy bands in a crystal with periodic potential.

The real shape of the band structure is very complex. Figure 3.2 illustrates the energy band structure of silicon with an indirect and gallium arsenide with a direct band gap. In the direct band structure the maximum of the valence band is located exactly below the minimum of conduction band and for electrons in the valence band there is no need to change their momentum to move to the conduction band whereas in the case of indirect band structure a change in the momentum is essential for electrons to move from the valence to conduction band.

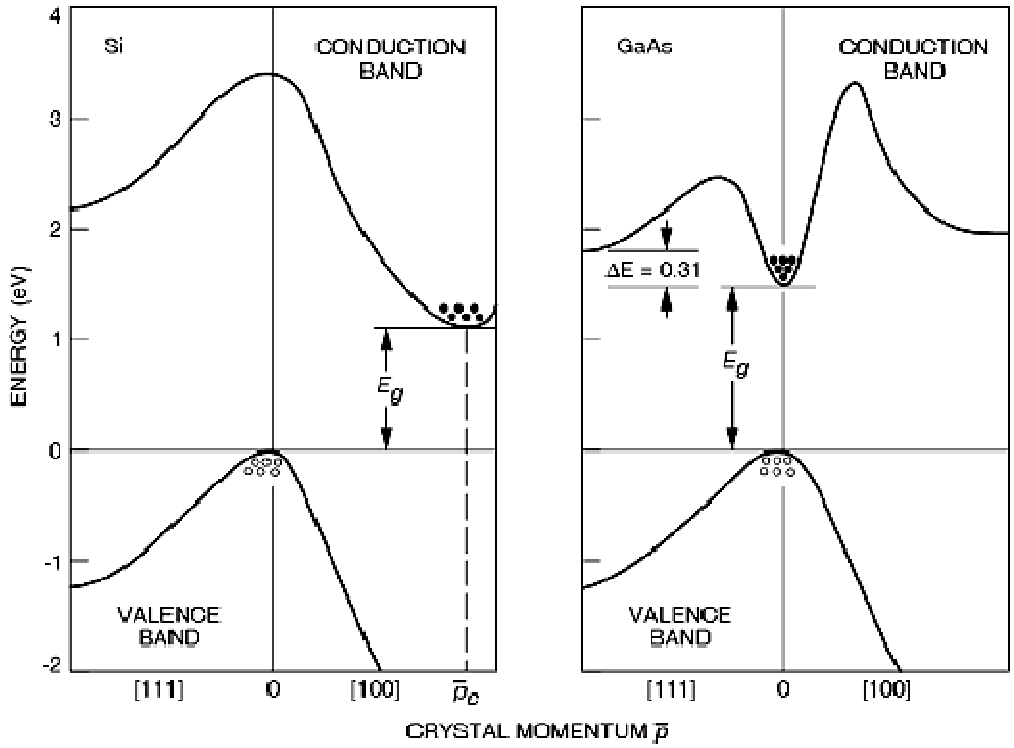

Figure 3.2 Energy band structures of Si and GaAs. Circles (○) indicate holes in the valance bands and dots (●) indicate electrons in the conduction bands [22].

3.2 Semiconductors with restricted dimensions

In a semiconductor, electrons in the conduction band and holes in the valence band can be bound to each other via Coulomb interaction forming a particle called an exciton. This model is similar to that of two bodies (e.g. electron and hole) forming a pair and orbiting around a common centre of mass. Electron and hole pairs can move freely in the crystal. The binding energy for an exciton is:

$$E_n = -\frac{m^* e^4}{32(\varepsilon\pi\hbar n)^2} \quad (3.2)$$

By comparing this with the Bohr energy model:

$$E_n = -\frac{e^2}{2\varepsilon n^2 a_B^*} \quad (3.2)$$

The effective Bohr radius is:

$$a_B^* = -\frac{\varepsilon h^2}{4\pi^2 m^* e^2} \quad (3.3),$$

where m^*, ε, h, and e refer to the effective mass of the exciton, the dielectric function of the material, the Planck constant and the charge of the electron, respectively. The overlap of the electron and hole wave function determine the binding energy of the exciton. In a bulk semiconductor due to less overlap of the wave functions and the resulting weak binding energy of the electron-hole pair, it can be broken by applying a weak electric field or by thermal excitation. By reducing the size of the material to smaller than the characteristic Bohr radius in any dimension the wave functions overlap and interaction between electron and hole is enhanced and the binding energy increases. Restriction of electron and hole pairs in one, two or three dimension to less than the Bohr radius, results in an increase in the binding energy, called the quantum confinement effect.

3.2.1 Quantum well and quantum wire

A quantum well is made of a thin layer of a semiconductor sandwiched between two thick layers of a semiconductor with wider band gap. The density of states for a quantum well (Dingle et al. 1974) is shown in figure 3.3. The energy levels of carriers are discrete along the confined direction and this causes the step-like density of states. In quantum wire structure carriers are confined to move in one direction and the density of states diagram shows sharp peaks.

3.2.2 QDs

Charge carriers in a QD structure are confined in all three dimensions this structure is called a zero dimensional structure. The confinement of electron-hole pairs in a QD is

stronger than in one or two dimensions resulting in more enhanced wave function overlapping, thus larger binding energies. This means that electrons and holes remain bound even in an external electric field and at room temperature, which enhances the probability of recombination via emission of a photon. The density of states is a Dirac delta function. The energy levels are completely quantized similar to atomic energy levels; hence QDs are sometimes called an artificial atom. Figure 3.3 shows the schematic diagram of the density of states (DOS) in the conduction band (CB) and the valence band (VB) for bulk material (a), a quantum well (b), a quantum wire (c) and a QD (d) functioning as the active layer in a semiconductor laser [23].

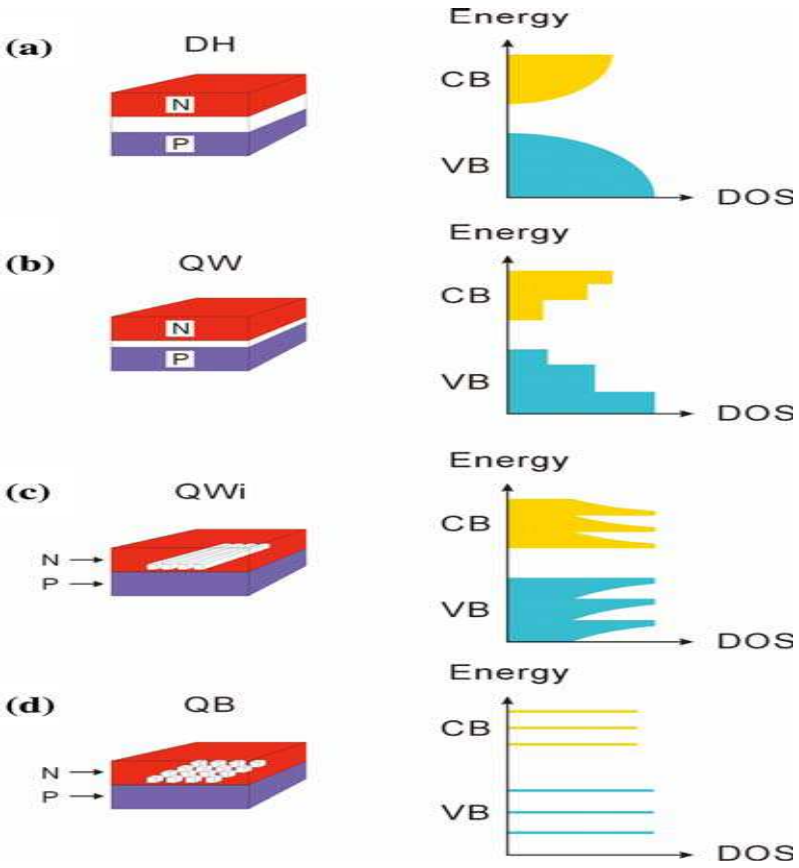

Figure 3.3 Schematic diagram of the density of states (DOS) in the conduction band (CB) and the valance band (VB) for bulk, quantum well, quantum wire and QD as an active layer in a semiconductor laser [23].

3.3 Coherent and Incoherent Epitaxial Structures and Critical Thickness

Epitaxial layers grown on a substrate with different lattice parameter are mismatched with respect to the substrate lattice. Hence these mismatched structures incorporate strain and are called strained structures. If the lattice constant of an epitaxially grown layer is considered as a_L, and that of the substrate material a_S, then the strain between them is defined as [22]:

$$\varepsilon = \frac{a_s - a_L}{a_l} \quad (3.4)$$

For thin over-layers the lattice mismatch causes elastic strain and for thicker layers as shown in figure 3.4b plastic deformation, i.e., after every 1/ε-th bond along the surface between the substrate and the over-layer there appears a missing or extra half-plane known as a dislocation. These structures are known as incoherent structures. For a small amount of ε (ε< 0.1) as illustrated in Figure 3.4c the monolayer grows perfectly on the substrate and the growth process, despite strain occurring between overlayer and substrate does not introduce structural changes and/or dislocations before relaxation occurs. Such a structure is called a coherent structure. The coherent layer is usually tetragonally distorted and the ratio of the out-of-plane and in-plane lattice parameters corresponds to the Poisson ratio. Nevertheless with increasing thickness of the grown layer on the substrate the strain increases and at a critical thickness of the overlayer the strain is relaxed via formation of dislocations. These misfit dislocations are energetically favourable and the presence of these has a significant damaging effect on the both electronic and optical properties of the structure[24]. According to simplistic theories this critical thickness is defined as [18]:

$$d_c \cong \frac{a_s}{2|\varepsilon|} \qquad (3.5).$$

Under realistic conditions the determination of the critical thickness is complicated and depends on many different parameters, such as growth and surface conditions, etc. After

the critical thickness and appearance of dislocations the overlayer grows without strain. Coherent epitaxial structures have interesting optoelectronic properties; whereas unstrained epitaxial layers with thickness greater than d_c can be used as new substrates for new overlayers. Above the critical thickness two situations can happen. If the dislocation is trapped in the substrate-overlayer interface and does not propagate into the subsequent layers, the epitaxial growth mode is useful for optoelectronic applications. If the dislocations propagate through subsequent layers, this has proven to deteriorate opto-electronic performance [24].

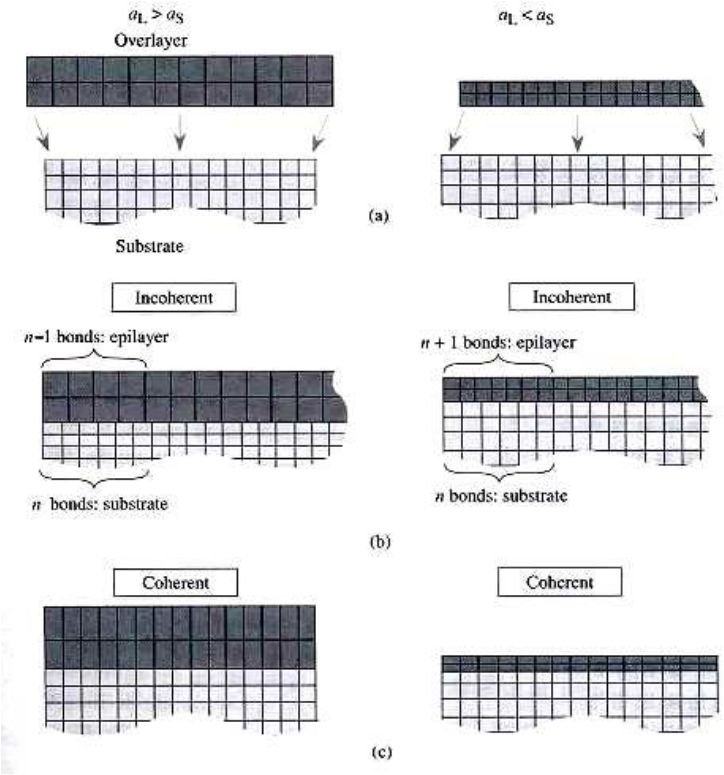

Figure 3.4: a) Schematics of overlayers with different lattice constants compared to the substrate leading to b) generation of dislocations in the interface and c) coherent tetragonally distorted epitaxial structure with no dislocations [18]

A variety of investigations were carried out in order to study the critical thickness of InAs on GaAs (001)[25-27]. Leonard et al. suggested by AFM investigation that the total InAs coverage is a critical parameter in the morphological change of 2D to 3D

phase of epitaxially grown InAs on GaAs (001). They found that the critical thickness of InAs was 1.5 MLs for samples grown at a substrate temperature of 530ºC and with a growth rate of 0.1 ML/s. Their data were fitted with a function of the form of:

$$\rho = \rho_0(\theta - \theta_0)^{\alpha} \quad (3.6),$$

where ρ and θ are the self assembled quantum dot (SAQD) density and InAs coverage, respectively. Their extracted quantities for the density ρ_0, and the critical thickness θ_c, were 2×10^{11} cm^{-2} and 1.5 ML respectively.

Kobayashi et al. reported in an AFM investigation a critical thickness of 1.57 ML for a sample grown on a substrate at 500ºC and with an InAs growth rate of 0.22 ML/s.

In a recent observation carried out by Wu et al. [28] a two stage evolution in the density and total volume of SAQDs with InAs coverage was observed. The authors observed a power function dependency for the density and total volume of 3D islands on extra InAs coverage ($\theta - \theta_c$) as had been observed previously by Leonard et al.[27] .

Both Kobayashi's and Wu's groups have discussed the mechanism behind the two stage evolution of 2D to 3D islanding process as follows: In the first stage the number and density of islands is low and they grow isolated and far from each other. When the island density exceeds a critical amount individual islands interact with each other and transportation of material between them becomes probable.

3.4 Heterostructure semiconductor growth modes

Depending on whether the systems are lattice-matched or lattice-mismatched and on the substrate and epilayers surface and interface free energies, three different modes can occur during the growth process. In a lattice-matched system, if the substrate surface energy is more than that of the sum of the epilayer and interface energies, growth occurs in Frank-van der Merwe mode [29] (see figure 3.5). If the sum of interface and epilayer surface energies is more than that of the substrate surface energy, atom to atom (or

molecule to molecule) bonding in the epilayer is stronger than atom to substrate (or molecule to substrate) bonding. Hence island structures appear on the substrate. This growth mode is known as Volmer-Weber mode [30].

For a lattice-mismatched (strained) system the strain induced energy becomes important. The growth mechanism can first be Van-der-Merwe growth, but as the layer thickness increases the strain energy rises and ultimately at the critical thickness, which depends on lattice constant of the substrate and the deposited material as noted already, relaxation can happen by formation of islands of the deposited material. This growth mode of self-organised QDs (SOQDS) islands on a two dimensional wetting layers is known as Stranski-Krastanov (SK) mode [31].

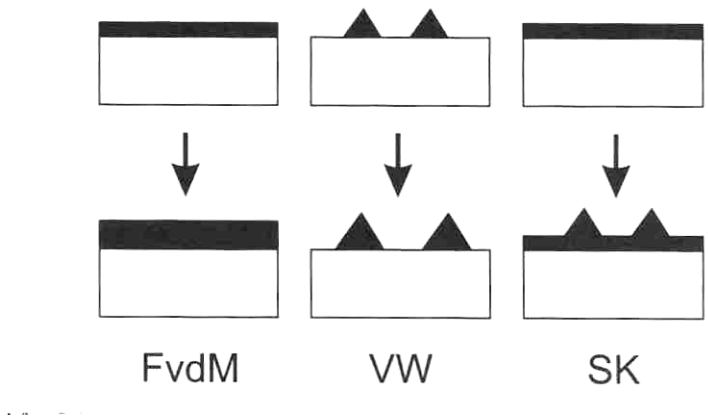

Figure 3.5 Schematic diagrams of Frank-van der Merwe, Volmer-Weber and SK growth modes [32]

3.5 QD formation mechanism

In SK growth mode before the growth of one monolayer, the growth process may start by deposition of a random distribution of atoms on the growth surface followed by formation of two dimensional islands. Then these islands coalesce and form big areas of two dimensional layers as shown in Figure 3.6 By continuing the growth process and depositing material on the growth surface a two-dimensional structure forms. This layer by layer growth mechanism continues until the critical thickness of the deposited material is reached. Because of less in-plane constraint the lattice can relax at steps and

corrugations, which can therefore act as sinks for the deposited material to migrate to; hence deposition is increased here leading to formation of three dimensional islands with or without dislocations.

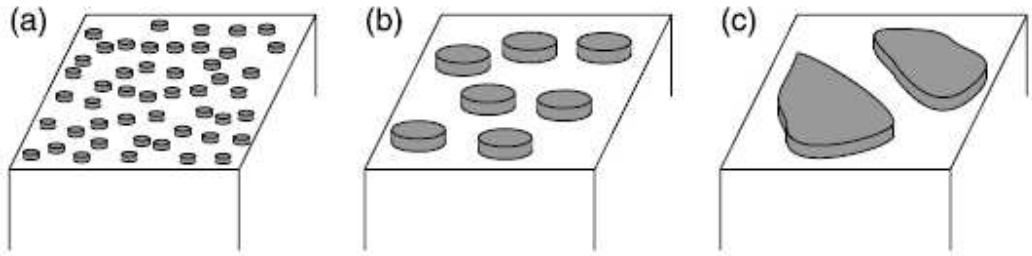

Figure 3.6 Schematic diagram of the evolution of growth before the formation of a monolayer in SK growth mode [33]

Three dimensional SOQDs were observed for the first time in a InAs/GaAs superlattice by Goldstein et al.[34]. The authors performed PL, STEM and XRD investigation and observed 3D islands of InAs in 2.5 ML of InAs. Later in the early 1990s further evidences of 3D SOQDs were reported by several groups in different structures [35, 36]. Despite plenty of practical investigations the mechanism of the 2D to 3D transition is not entirely clear yet.

In the epitaxial growth of InAs on GaAs (001) the transition from a 2D structure to a 3D structure of islands was explained in different ways. Scanning tunnelling microscopy (STM) observations of quasi 3D clusters as a precursor to 3D island formation was reported by Heitz et al. [37] and Ramachandran et al.[38]. The authors described re-entrant 2D to 3D change by appearance and disappearance of quasi 3D clusters and re-appearance through more deposition of indium prior to the formation of 3D islands. Patella et al. [39] proposed that after deposition of 1 ML InAs on GaAs (001) a ternary alloy layer of $In_xGa_{1-x}As$ (x=0.82) forms and then a ‘’floating’’ form of In deposits. Krzyzewski et al. [40, 41] observed by STM investigation the coexistence of large 2D islands, which do not evolve into 3D islands, with irregular small 3D islands (2-4 ML height) containing nearly 150 atoms. These small entities evolve to mature islands

containing an average 10^4 atoms after deposition of an incremental 0.05 ML InAs after the critical thickness. The two authors insisted on the important role of strain in the early stages of QD formation but not in their evolution.

3.6 NC growth in amorphous matrix

NC-embedded materials have great potential in, e.g., energy storage and harvesting, opto-electronics and IT applications; a famous precursor as far as the fabrication process is concerned, is stained glass. This type of material was fabricated by dissolving metals in molten glass. Then metallic NCs were formed by quenching and annealing. This procedure is the platform of production of semiconductor NCs in oxide matrices. The first stage is to produce excess semiconductor in the oxide host. This is followed by NCs formation which normally occurs by annealing at high temperatures.

Oxide matrices grown on Si wafer are a popular host for NCs, based on the compatibility with Si based CMOS technology. A variety of specialized techniques can be used to produce NCs in oxide matrices. Aerosol synthesis [42, 43], ion beam co-sputtering [44, 45], chemical vapour deposition [46, 47] and ion implantation [48-50] are the most common techniques to produce NCs. These techniques are based on low mobility of excess material in the matrix at high temperature which lead to coalesce of excess atoms or molecules into NCs.

In this research after growth of silica layers on Si by thermal oxidation, ion implantation has been used to introduce Si ions into the matrix followed by high temperature annealing to form Si-NCs (for more detail see 6.2). For the growth of Ge-NCs in alumina the radio frequency co-sputtering technique has been employed (for details of the growth procedure see 4.2)

3.7 Growth Techniques

Because of the importance of being able to control the size of semiconductor quantum structures in order to achieve quantum confinement properties, the growth technique

should be capable of achieving layer thicknesses with mono-layer precision. For growing epitaxial compound semiconductors different techniques, such as Chemical Vapour Deposition (CVD), Liquid Phase Epitaxy (LPE), Metal Organic Chemical Vapour Deposition (MOCVD) and Molecular Beam Epitaxy (MBE) are used. MBE and MOCVD which are two widely used techniques to grow high quality epitaxial nano-structured semiconductor materials will be briefly explained in the following sections.

3.7.1 MBE

MBE is an epitaxial growth technique using the reaction of a beam of molecules or atoms with a substrate in ultrahigh-vacuum (~10^{-10} Torr). An MBE machine consists of three main chambers, the growth chamber, a buffer chamber and a load-lock chamber. The load-lock chamber is the only chamber in direct contact with the atmosphere and is used to load and unload substrates and its pressure is around 10^{-8} Torr. The buffer chamber is used to avoid direct atmospheric contact of the growth chamber and also to clean the substrate by heating in ultrahigh vacuum before inserting it into the growth chamber for the growth process.

Figure 3.7 shows a schematic diagram of a MBE growth chamber. Sources of pure elements in the form of solids are stored in places known as effusion cells, which are independently heated to make thermal beams of atoms or molecules. For each cell there is a shutter to allow beams of atoms to enter into main chamber during grow process. In order to grow uniform epitaxial layers the substrate holder rotates with constant speed. High quality growth with little contamination due to the ultrahigh vacuum conditions and the possibility to perform growth at low temperature lowering the diffusion probability, are advantages of MBE compared to other techniques, despite the low growth rate process. By using in-situ Reflection High Energy Electron Diffraction (RHEED) and Auger Electron Spectrometer tools, growth rate and substrate temperature calibration as well as direct feedback about the growing layer morphology is possible. RHEED uses a beam of high energy electrons (~10keV) which hits the substrate at low angles (1-3 degrees) so that only surface features are observed.

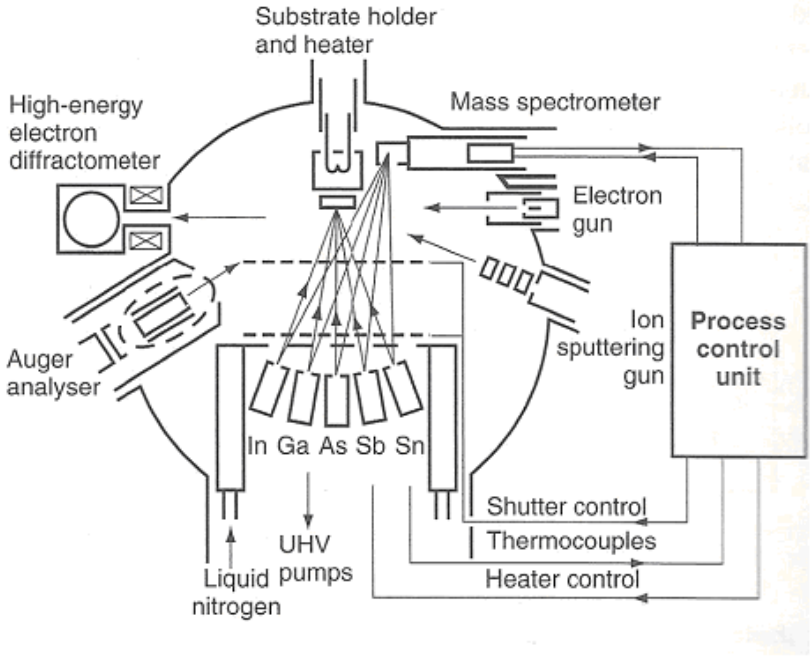

Figure 3.7 Schematic diagram of a MBE growth chamber [108]

The InAs/GaAs samples in this study were grown on (0 0 1) GaAs substrates in a RIBER VG V100HU MBE system. The samples consist of a 500 nm buffer layer grown at 580 °C, followed by 10 periods of a 24.5 nm thick GaAs spacer and InAs layer with a nominal thickness of 1.77 ML grown at ~ 450 C. One type of samples was grown with a growth interrupt of 60 s after deposition of the InAs in each period, whereas in the other one GaAs and InAs were grown continuously. This experiment was carried out in order to investigate the role of surface diffusion in releasing strain.

3.7.2 Ion Implantation

Ion implantation is a technique used to plant a specific dose of positive or negatively charged species at a specific depth in a substrate. Figure 3.8 depicts a schematic representation of an ion implantation system. Ion implantation is a low temperature process and allows accurate control of dopant dose and depth. The ion source consists of a filament which produces electrons to react with an elemental source. Electrons are accelerated in a spiral path by a magnet to enhance the ionization process. The produced ions are then extracted and accelerated towards an analysing magnet, by which specific

species can be selected to enter the ion acceleration column. The accelerated ions are guided to an electronic scanning section and scanned by magnetic lenses over a selected area of the substrate and implanted inside the targeted region.

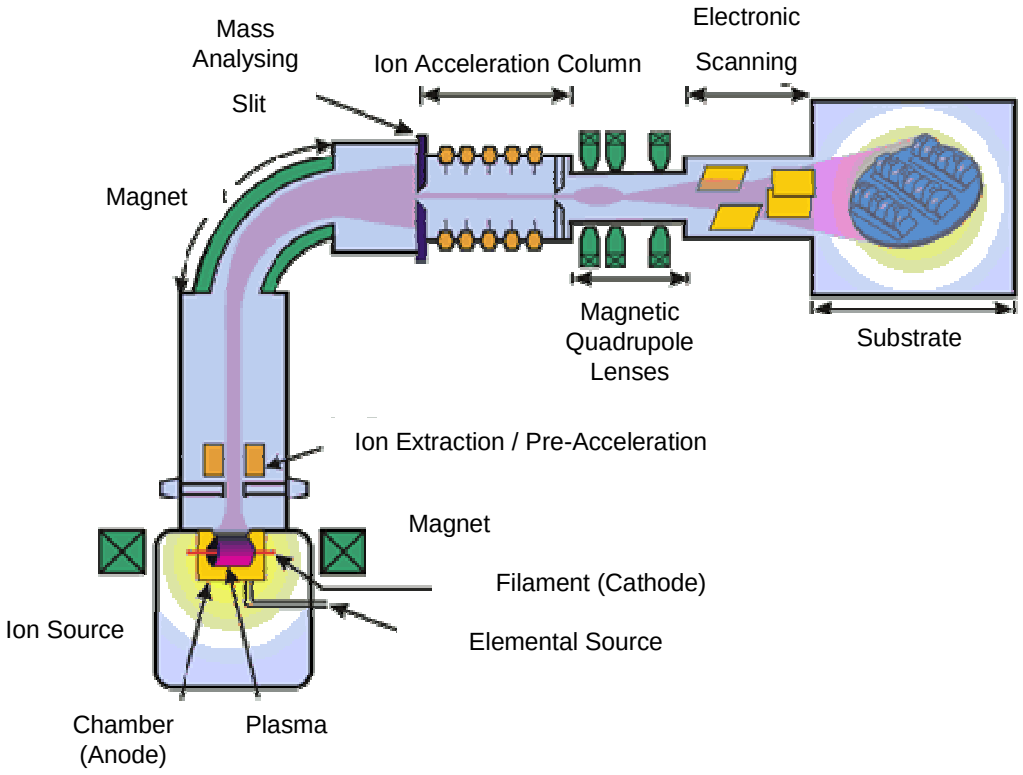

Figure 3.8 Schematic diagram of an Ion implanter unit used in semiconductor device technology (http://www.spirecorp.com/spire-biomedical/surface-treatment/index.php)

Er-doped Si-NCs in silica investigated in this research and corresponding reference samples were prepared by the ion implantation technique. A (100) Si substrate was thermally oxidized at 1000°C in order to produce a 500 nm SiO_2 layer. Er implantation was performed with a beam of ions at 300 keV to an areal density of 3×10^{15}cm $^{-2}$. Excess Si was implanted with Si^+ ions at 80 keV to an areal density of 8×10^{16}cm $^{-2}$. In order to obtain Si-NCs and treat implantation damage, samples were annealed at 1100°C for 1 h in an N_2 ambient. To passivate the "dangling bonds" (P_b), which

constitute SiO_2/Si-NC interface-type defects [51] thermal treatment in an N_2:H_2 (5%) ambient was performed at 500 °C .

3.7.3 Radio Frequency Magnetron Co-Sputtering

In a sputtering system a target material, which is mounted on a magnetron is hit by accelerated ions (normally Ar^+). Atoms are produced as a result of the impact of the ions with the surface of the target. The neutral, sputtered atom species are deposited on a substrate. A pulsed voltage is applied between the target and the substrate, producing a plasma. The pulsed current is used especially to discharge dielectric targets. The plasma enhances the sputtering rate, because Ar atoms collide with electrons which results in production of additional electrons and Ar^+ ion. A magnetic field is applied underneath the target, which forces Ar^+ to move in spiral paths thereby enhancing the sputtering rate and providing homogeneous deposition on the substrate. Figure 3.9 illustrates the sputtering method.

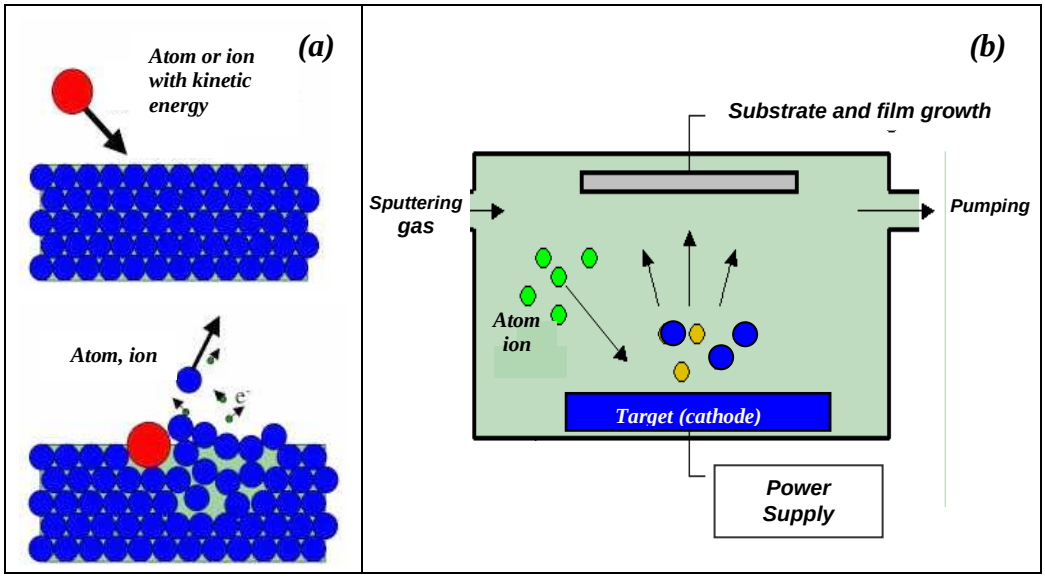

Figure 3.9: a) Atomic interaction in the sputtering target; b) basic schematics of the inside of a vacuum chamber showing the sputtering process[109]

Ge-NCs in alumina were grown by a conventional co-sputtering method using an RF-magnetron Alcatel SCM 650 machine. The target was a 50 mm diameter alumina plate with a purity of 99.99. For the Ge doping an unpolished polycrystalline sheet of Ge with purity of 99.99% was placed at the centre of the Al_2O_3 plate. Si(111) wafers were used as substrates and kept at 500 °C during the deposition. The pre-sputtering pressure of the growth chamber was at least 1×10^{-6} mbar. In order to clean the surfaces of both, target and substrate, in situ argon plasma treatment was performed. The as-grown samples were annealed at 800 °C and 900 °C, for 1 h in air in order to improve the crystallinity of the Ge phase and to control the size of the NCs. [52].

4

Germanium NCs in Alumina

4.1 Introduction

Undesirable charge leakage in modern flash memories based on polycrystalline silicon prohibits the use of thin tunnel oxide layers Conventional thick tunnel oxides require a comparatively high operating voltage, which is a major disadvantage. For device application the use of Metal–Insulator–Semiconductor (MIS) structures using Si and Ge semiconductor NCs have been reported to show good memory effects and low power operation at room temperature [7]. In fact, one of the most common structures studied for memory or LED purposes is Si-NCs embedded in SiO_x. Ge and SiGe NCs embedded in an alumina dielectric matrix have also been studied for potential device applications [10], however, in most works in the literature NCs have been grown inside a SiO_2 matrix.

Since Al_2O_3 has a high dielectric constant, twice that of SiO_2, the thickness of the oxide layer can be reduced to 2-3 nm. Moreover, Al_2O_3 exhibits good mechanical properties and can endure high temperatures; this makes it a good candidate for replacing silica as a gate dielectric material in flash memory systems and thereby improve their performance.

In this work, structural properties of Ge-NCs embedded in an alumina matrix were investigated with conventional diffraction contrast TEM, HRTEM, Raman spectroscopy and XRD to give an understanding of the material and the size and distribution of the NCs.

Crystallographic investigations were performed with XRD, in conventional $\theta-2\theta$ geometry (Philips PW1710) using Cu K_α radiation. The identification of the crystalline phases was made using the JCPDS (Joint Committee of Powder Diffraction) database.

The microstructure of the samples was examined using a Tecnai F30 FEG transmission electron microscope. The HRTEM cross-sectional specimens were prepared by manual polishing followed by ion beam milling. Raman scattering spectra were obtained using a Jobin-Yvon T64000 system with an Olympus BH2-UMA microanalysis system and a CCD detector, in a backscattering geometry. Raman spectroscopy was performed at room temperature using the 514.5 nm and 488.0 nm lines of an argon laser at a power of 50 μW and an area of the sample of ~ 1 μm^2.

4.2 Sample design

Figure 4.1 represents the schematics of the samples. The sample growth was presented in chapter 3.7.3. In order to improve the crystal structure of the Ge phase and achieve structures with small (sample A) and large (sample B) Ge-NC sizes, the as-grown samples were annealed at 800 ºC and 900 ºC, for one hour, under air pressures of $4.6x10^{-1}$ and $8.0x10^{-4}$ (Pa), respectively. Samples were grown in the Department of Physics, the University of Minho, Portugal. More details are presented elsewhere [53].

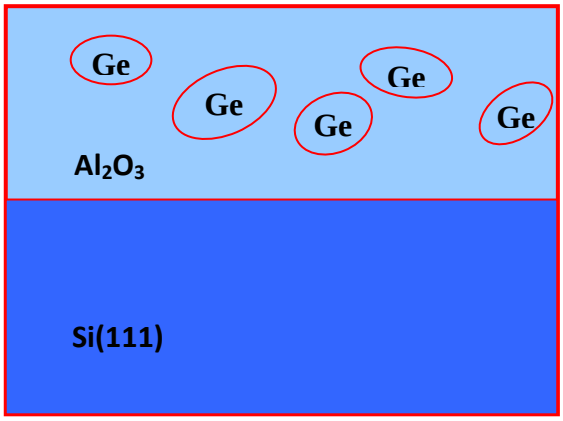

Figure 4.1 Schematics of Ge-NCs in alumina samples

4.3 XRD Results

The XRD experiments were conducted in the Department of Physics, the University of Minho by Miss Sara Pinto. For this study, we have measured two types of samples that were labelled A and B with small and large NC diameter, respectively. These samples presented different behaviours, as discussed below.

The XRD diffraction diagrams of samples A and B are depicted in figure 4.2. They clearly reveal (111), (220), (311) and (400) reflections related to peaks from the diamond structure of Ge. Annealing at higher temperature led to sharper peaks and a better crystallinity of the Ge NCs: while sample *A* shows broad peaks, sample *B* shows slightly shifted sharp peaks. The shift in the peak position of sample B probably could be explained by the stress exerted by the alumina matrix on the NCs. Using Lorentzian functions to fit each XRD peak of the samples, we measured the mean diameter values of the NCs. The NC sizes obtained for samples *A* and *B*, were 7 nm and 17 nm, respectively. Careful analysis of the XRD results of the *B* sample showed shift to larger angles (smaller lattice parameter) compared to the those of bulk Ge, which is an indication of compressive strain in the structure. The estimated strain was 0.8 % for the (220) planes in sample B.

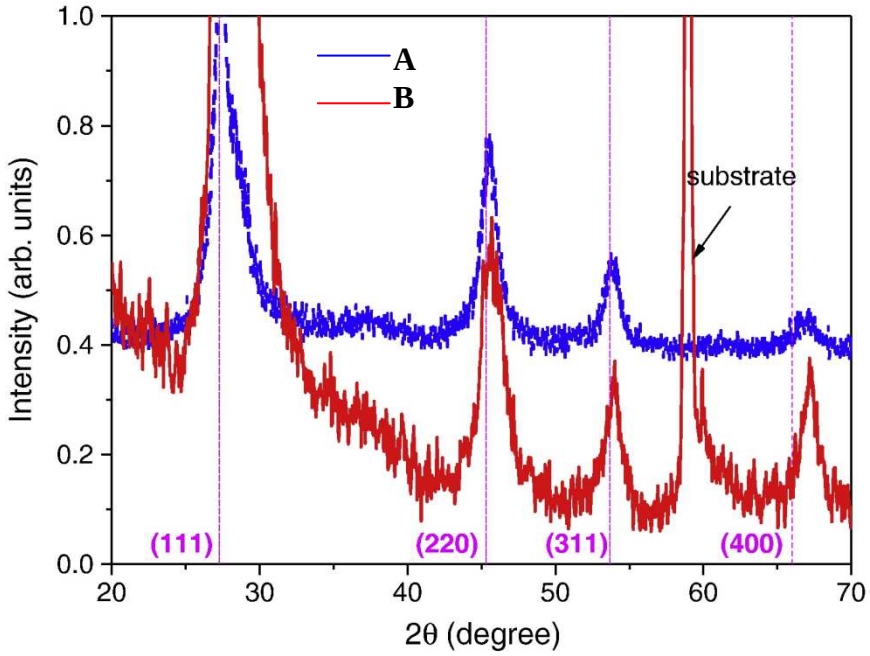

Figure 4.2 XRD diffractograms of sample A (blue) and B (red). Dashed lines denote the positions of the diffraction peaks in bulk Ge

4.4 Raman Spectroscopy

The Raman Spectroscopy was carried out in the Department of Physics, the University of Minho by Miss Sara Pinto. Room temperature Raman spectroscopy was implemented by means of the 514.5 nm and 488.0 nm line of an argon laser at a power of 50 μW centred on a ~1 μm^2 area of the sample to study crystallinity and size distribution of the Ge-NCs.

Figure 4.3 shows typical Raman spectra for samples A and B. The spectra show a red and blue shift for sample A and B, respectively, compared to bulk Ge (green line). For sample A, the broadening and red shift of the Raman peak is an indication of a reduction in the size of the NCs. The red shift and the broadening of the Raman have been explained by the quantum confinement effect on phonons in a finite volume of the NCs[54-57]. The Raman peak for sample B (larger NCs) is blue shifted which may be explained by the exertion of compressive stress by the alumina matrix. This phenomenon has been studied for stressed Ge-NCs in alumina [10, 55, 58, 59]

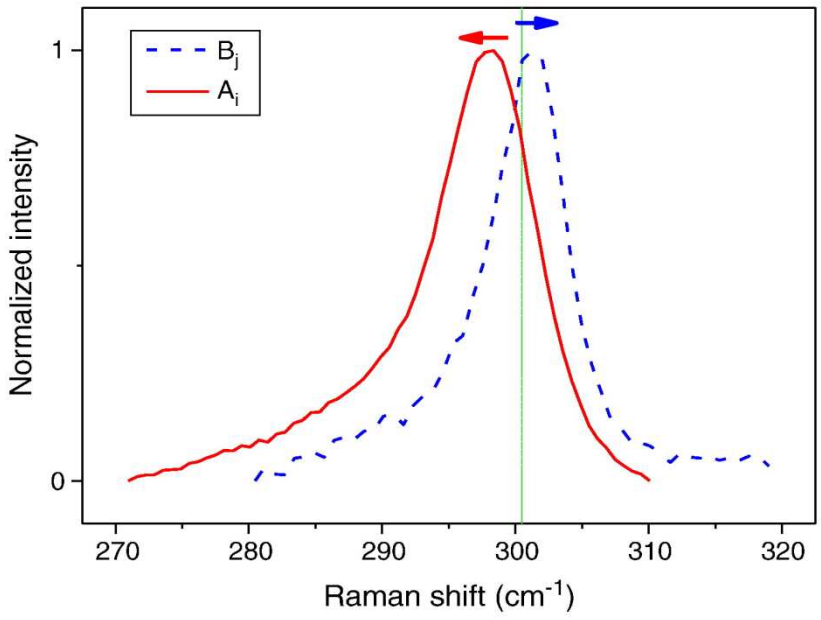

Figure 4.3 Raman spectra of sample A and B. The peak is red-shifted for A and a blue-shifted for B compared to the peak for bulk Ge (green line).

4.5 TEM Results

(a) Conventional TEM

In order to study the microstructure of the samples diffraction contrast dark field (DF) and bright field (BF) TEM imaging was carried out in a Tecnai FEG-30. Conventional DF imaging is a powerful technique to light up crystallites aligned in specific orientations. By aligning the electron beam close to a zone axis of the substrate and by selecting a certain diffraction spot, NCs with planes corresponding to this diffraction spot can be seen in the image. By imaging NCs under a number of different **g** vectors the majority of NCs can be revealed.

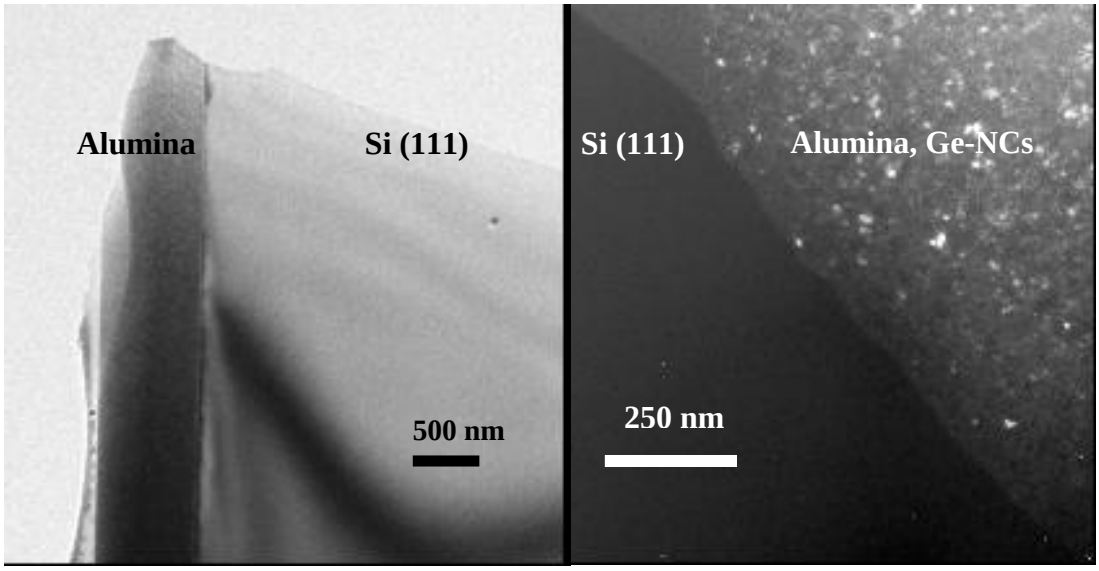

Figure 4.4 Conventional TEM-BF (left) and TEM-DF (right) image of the alumina layer containing Ge NCs, grown on a Si substrate. For the DF image the (111) reflection was selected with the beam aligned along the <110> zone axis of the substrate.

Figure 4.4 shows a TEM-BF (left) and TEM-DF (right) image of sample B. The silicon substrate, the 600 nm thick alumina matrix and the glue can be seen clearly in the BF image. The DF image clearly shows Ge NCs with the (111) plane-vector oriented parallel to the **g** vector.

The presence of a crystalline structure was proven by means of TEM-DF images. However diffraction contrast images cannot reveal atomic-scale structure of the NCs and the alumina matrix and neither can they show the exact NC sizes. In order to obtain this information, HRTEM images were acquired in a Tecnai. Figure 4.5 shows HRTEM images of the NCs in sample A, acquired at different foci revealing the polycrystalline nature of the matrix. The nano-scale polycrystallinity becomes apparent by the emergence and disappearance of lattice fringes in different positions depending on the defocus, whereas in the comparatively larger Ge-NC the lattice image prevails in all six images. Extensive twinning, observed in most of the NCs in this sample, indicates that stress relaxation has taken place and we therefore expect the NCs to be nearly unstrained.

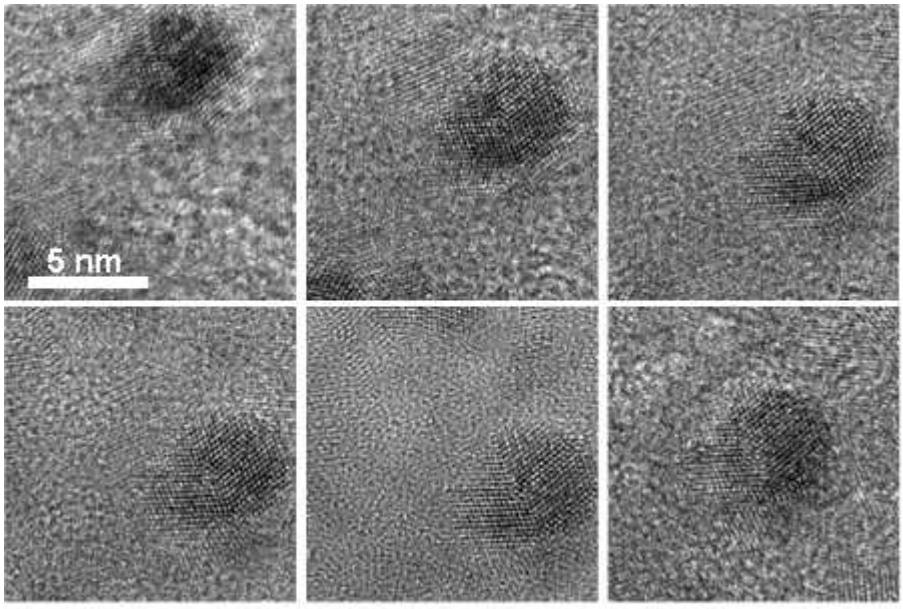

Figure 4.5 HRTEM images of sample A showing a relaxed NC with a planar fault at different focus conditions in the polycrystalline alumina matrix.

This is in agreement with the Raman spectra of sample A, which suggests unstressed Ge-NCs.

In order to ascertain, whether the un-faulted NCs in sample B are strained, lattice plane spacings were determined. Figure 4.6 shows an image of a big Ge-NC in sample B

together with its Fourier transform (FT) pattern representing the (211) zone axis pattern of the diamond crystal structure. Different diffraction spots of this FT pattern were used to measure lattice plane distances in this NC. To establish such strains in the Ge-NCs, HRTEM images of the Si substrate were taken as reference and, more importantly, to estimate the error in the determination of lattice plane distances from FTs of HRTEM images. The lattice spacing of the Si substrate was determined using FTs of HRTEM images with the sample aligned at the (110) zone axis for various reflections and in various locations and compared to values calculated from the silicon's lattice constant (a = 5.43 Å). Lattice spacing for the Ge-NCs were then obtained from FTs of HREM images taken at the same magnification as the Si substrate images.

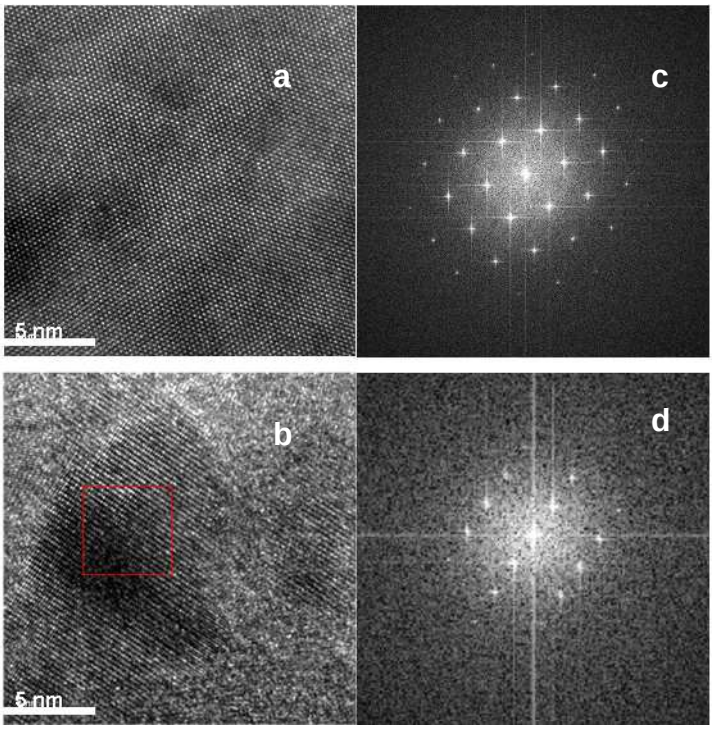

Figure 4.6 HRTEM images of (a) Si substrate, (b) a big NC in sample B together with the FT of the Si substrate (c) and the Ge-NC (d)

Table 1 illustrates lattice planes distances and error values for both, substrate and NCs. As can be seen changes in the lattice distances of the NCs are within the error limit, and hence the strains would be below 1%. The shifts in the XRD peaks towards larger angles in figure 4.1b arises from compressive strain around the 0.8 % mark for (220)

planes as mentioned in 4.3; this is the error limit of the HREM technique, and hence we would not be able to confirm this strain from lattice images.

Planes	Silicon substrate		% ($d_{Calc.}$-$d_{Exp.}$)	Ge-NCs		
	Exp.	Calc.		Exp.	Calc.	Displacement
111	3.110	3.135	+0.7%	3.240	3.262	+0.6%
220	1.890	1.919	+1.5%	1.970	1.990	+1.0%
113	-	-	-	1.690	1.700	+0.5%

Figure 4.7 differences in the calculated and measured values of lattice plane distances based on Fourier methods applied to HRTEM images, and percentages of evaluated stress in the sample B.

4.6 Conclusion

Ge-NCs embedded in Al_2O_3 films were successfully produced by RF-magnetron sputtering. Samples with two different NC sizes (on average ~5 and ~8 nm) were produced by changing the annealing temperature and gas flow pressure. Raman and XRD results indicate strain in the bigger NCs, however, peaks from the polycrystalline alumina matrix (not indicated in figure 4.2) obscure the exact position of the Ge-peaks in the XRD results. Furthermore, the shifts, if genuine, are concomitant with strains < 0.5 %, which is below the accuracy of HRTEM-based lattice constant determination. HRTEM suggests unstrained structures for the small NCs, because plastic relaxation and extensive nano-twinning have taken place. This explains red shift in the Raman peak position of the sample and is a sign of relaxed NCs. Through-focus HRTEM images show the polycrystalline structure of the matrix.

5

InAs/GaAs QDs

5.1 Introduction

In(Ga)As/GaAs QDs are attractive materials for device applications, including laser diodes [60], optical amplifiers[61] and detectors[62]. In(Ga)As/GaAs QD optical amplifiers operating at 1.3 μm wavelength have potential applications in optical communication and fibre optics amplifiers. Due to the low optical absorption of silica fibres in this wavelength, transmission of data is ideal in long haul data transfer. Despite low optical absorption it is essential to amplify the signals at intervals. InAs/GaAs QDs amplifiers are better candidates for this application compared to their expensive InP-based counterparts. For device applications control of size, distribution and homogeneity of the dots, as well as defects within, are very important. A profound understanding of the formation and evolution of SOQDs and also of the early stage of the 2D–3D transition and its mechanism will enable use of the best growth condition for optimum structures. There is a general agreement that the 2D–3D transition during growth of InAs on GaAs(0 0 1) by molecular beam epitaxy (MBE) occurs within a $\sim$0.2 monolayers (ML) incremental deposition of InAs after the critical thickness (1.6–1.8 ML) has been reached [63]. It has been shown that the amount of material in the islands when the substrate temperature is more than 400 °C is greater than the amount of material deposited after 2D–3D transition and, more surprisingly, greater than the deposited InAs at $\sim$500 °C, and the only exception for this effect occurs at low deposition rates ($\lesssim$0.02 ML s^{-1}) in which case the total deposited amount of materials is the same before and after the 2D–3D transition [64]. Most of the aforementioned

investigations were performed by AFM, STM, RHEED and TEM; however, there are few direct investigations by high resolution STEM of the early stages of InAs pseudomorphic growth.

Several investigations have shown that by deposition of pure InAs on the GaAs the resulting islands may consist of InGaAs due to In segregation. Evidence found for an alloying phenomenon in islands at growth temperatures above 420 ºC suggested significant mass transport from both the GaAs and the wetting layers into the dips produced by In segregation into the dots [65]. As is expected with increasing the substrate temperature, In segregation is enhanced, and therefore In and Ga adatom migration to the resulting dips increases and consequently the total QD volume rises with increasing substrate temperature with the same coverage on InAs.

In a study by Kegel et al. [66] X-ray diffraction investigations have been carried out to find the strain distribution in InAs/GaAs QDs. The study showed that the strain varied from 0% in the base of the QD to 7% in its top, confirming changes in composition of the QD from GaAs in the base to InAs in the top. It has been found by several groups [66-69] that the alloy composition within the dots is not homogeneous but that there is an In concentration gradient from the top to the base.

Sanchez et al. [70] carried out an high-angle annular dark-field (HAADF) measurements in an aberration-corrected STEM to acquire images of InAs/GaAs QDS and by application of strain mapping in the acquired images they investigated the composition of the dots. They found inhomogeneous strain distributions as a consequence of a varying composition in the QD.

Recently Wang et al. [71] carried out atomic resolution quantitative EELS spectrometry in an aberration-corrected STEM to measure the compositional distribution across the centre of a QD and adjacent wetting layer in a 10 period InAs/GaAs structure with 2.43 ML and 25 nm thicknesses of InAs layers and GaAs spacers, respectively. The authors extract a linear profile of the In density across the centre of a QD and nearby wetting layer from the single scattering distribution of the In M4,5 edge. They found a

significant depletion of In in the wetting layer as a result of the dot growth and also an In concentration (x) close to unity on the top of the dot, which indicates indium segregation in this region. Their investigation is in a good agreement with the strain mapping study [66]. Many investigations showed that there is a high content of In on top of QDs [66, 72].

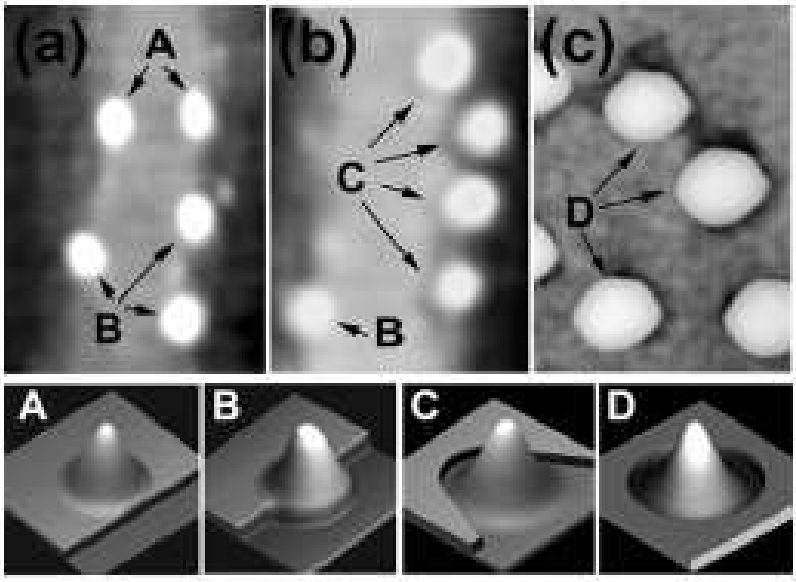

Figure 5.1 AFM images for coverages of 1.54 ML (a) and 1.61 ML (b). 'A' are QDs nucleated at the step edge, 'B' are QDs that have partially eroded, and 'C' are QDs that have completely eroded the step edge. (c) 80 × 120 nm^2 AFM image showing plane erosion occurring for 2.4 ML InAs growth at 522 ◦C ('D' are QDs after erosion). The bottom panels show schematic 3D views of QDs before and after the step or plane erosion [63].

It has been suggested that islands first nucleate at step edges as part of step erosion, owing to Ga-In intermixing and mass transport from the substrate to the islands and also subsequent erosion of steps by the evolving dot. The total volume of dots is 4.6 times the deposition in the 1.6-1.8 ML range [63, 73]. Figure 5.1 shows two areas of the surface of InAs with coverage, 1.54 ML (a) and 1.61 ML (b). QDs were observed to

nucleate at the upper side of step edges, as shown in panel (a). It can be observed that QDs close to the step edge, A, erode the step edge and evolve into B and C where they appear detached.

In this work we try to improve the understanding of the role of growth interrupts (GI) in the evolution of the microstructure of thin layers of InAs on GaAs (0 0 1) around the critical thickness for QD formation.

PL measurements were performed in order to investigate the role of GI in the early stage of 2D to 3D transition on the optical properties of the samples. This was complemented by XRD in order to obtain an overall view of related structural characteristics. HAADF- imaging was carried out in an aberration corrected dedicated STEM. The elemental distribution of In and Ga in the QDs was assessed by extracting maps of the relative intensity of the In–M_5 absorption edge in the low-loss region of electron energy loss spectroscopy (EELS) spectra (<35 eV). For this KK analysis was employed; the imaginary part of the dielectric function (ε_2) of the InAs/GaAs was extracted, which results in the suppression of the plasmon and hence in improved detectability of the In- (and Ga-) signal [74]. Furthermore, in order to quantify the In content in the QDs the sample thickness is required; the latter was obtained by applying the KK sum rule.

5.2 Samples design

Two different InAs/GaAs superlattices samples were studied. Samples were grown in a RIBER VG Semicon V100HU solid-source MBE system on (100) GaAs substrates in the School of Electrical and Electronic Engineering at the University of Manchester.
Sample XMBE#12 consists of a 10 period InAs superlattice with nominal thickness of 1.77 ML and a GaAs spacer layer with a thickness of 245 Å. The substrate temperature during growth of the stacked structure was kept at around 480-490 °C. The sample was grown with a growth interrupt (GI) of 60 s after the deposition of each InAs layer. Figure 5.2 (right) depicts the schematic sample structure.

Sample XMBE#11 consists of a 10 period InAs superlattice with nominal thickness of 1.77 ML and a GaAs spacer layer with a thickness of 245 Å grown without GI. The substrate temperature during growth of the stack was kept at around 480-490 °C. An illustration of the sample structure is given in figure 5.2 (left).

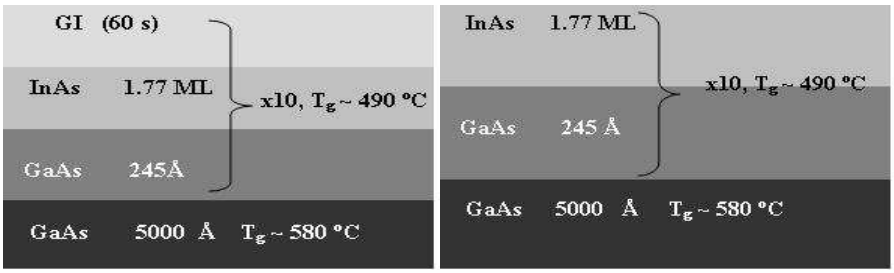

Figure 5.2 Schematic structures of XMBE #12 (right) and XMBE#11 (left)

Thus both samples are identical except for the introduction of growth interrupt after the deposition of InAs.

5.3 Results and discussion

5.3.1 PL

PL spectroscopy investigations were carried out on sample XMBE#11 (without growth interruption) and XMBE#12 (with growth interruption) in the Microelectronics and Nanostructure Group (M&N) by Dr Mohammad Alduraibi of the School of Electrical and Electronic Engineering of the University of Manchester in order to study the optical behaviour of the samples and the origin of this behaviour. PL measurements were performed at room temperature using the Accent RPM2000 system with a laser source operating at 532 nm with a power of 11mW. The laser spot was circular with a diameter of 01mm.

(a) Sample XMBE#11

Figure 5.3 depicts the PL emission spectra of sample XMBE#11detected by an InGaAs detector (left) and a Si detector (right). Note the difference in scale in the left and right panels. There is a strong emission at ~920 nm from the InAs QWs accompanied by a small peak at ~870 nm from the GaAs buffer. A broad peak at ~1510 nm is a sign of

formation of small QDs with inhomogeneous size distribution in the structure. As will be discussed later in the STEM results this small peak is related to small dots formed on the topmost InAs layer.

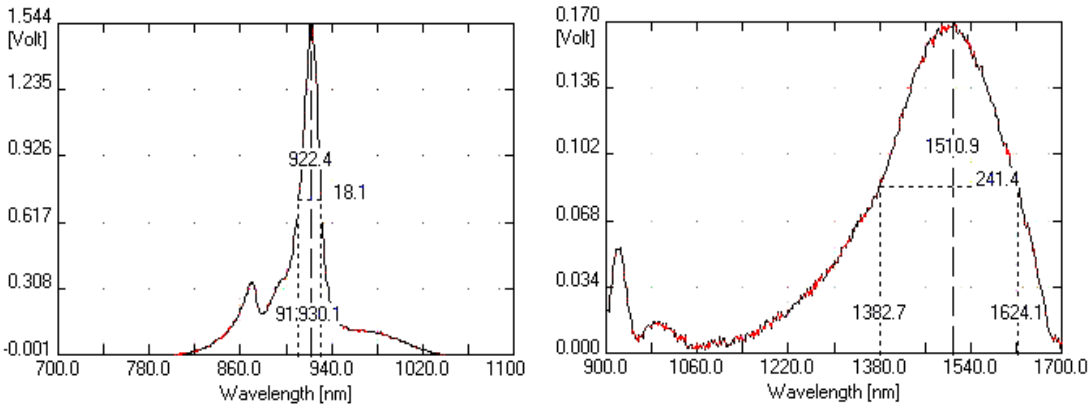

Figure 5.3 PL emission spectra of sample XMBE#11

(b) Sample XMB#12

Figure 5.4 shows PL emission spectra of sample #12 detected by the InGaAs detector (left) and the Si detector (right). A small bulk GaAs buffer layer peak at ~ 870 nm followed by very weak peak at ~1050 nm related to the wetting layer can be seen. In the right hand panel there is strong emission at ~1160 emanating from the QDs. Note again the different scales on the Y-axis. The disappearance of the 1500 nm emission peak maybe due to it being swamped by the much larger QD signal, and also might be attributed to a lack of small dots because the GI results in larger QDs.

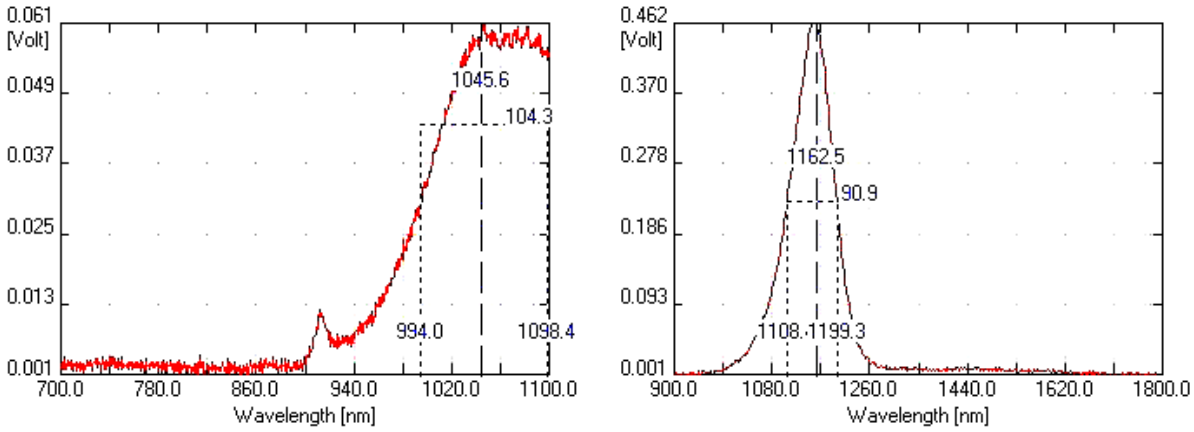

Figure 5.4 PL emission spectra of sample XMBE#12

5.3.2 DCXRD of samples #11 and #12

XRD measurements were carried out in the Microelectronics and Nanostructure Group (M&N) of the School of Electrical and Electronic Engineering of the University of Manchester by Dr Mohammad Alduraibi. Figure 5.5 shows DCXRD rocking curves of sample XMBE#11(top) and sample XMBE#12 (bottom).

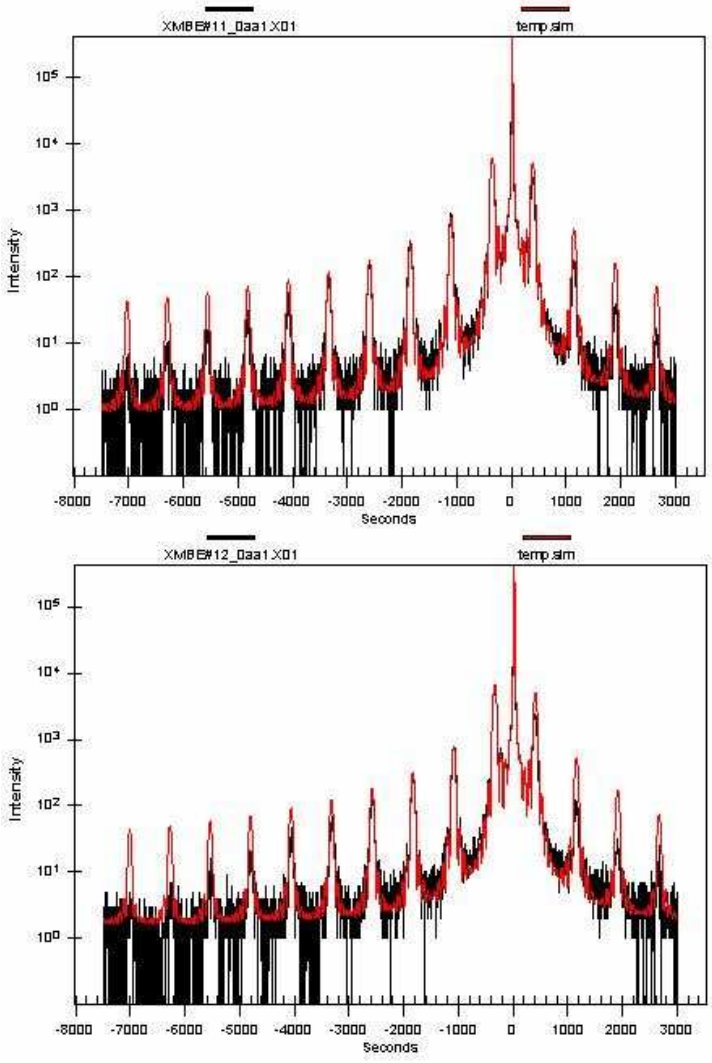

Figure 5.5 DCXRD rocking curve of sample XMBE#11 (top) and sample XMBE#12 (bottom).

As can be seen from curves there is a clear periodicity in both, and the experimental curves can be well fitted by the simulated curves (red). The results revealed that the thickness of the GaAs spacer layer was 24.7 nm and identical for both samples whereas

the InAs thicknesses were 5.38 Å and 5.20Å for samples XMBE#11 and XMBE#12 respectively. The difference in the thickness of InAs may be a result of the formation of QDs in sample XMBE#12.

5.3.3 TEM results

Conventional diffraction contrast TEM experiments were carried out in a Philips CM20 instrument operating at 200 keV with electron beam parallel to the <110> zone axis of the GaAs substrate. For both, samples XMBE#11 and XMBE#12, the BF and DF images are presented here. The strain in sample XMBE#12 appears to have relaxed by formation of QDS whereas in sample XMBE#11 there is no sign of QD formation in the buried InAs layer. However, we observed QDs in the surface topmost uncapped layer.

(a) Sample XMBE#11

Figure 5.6, right hand panel, shows a BF TEM image of sample XMBE#11 aligned with

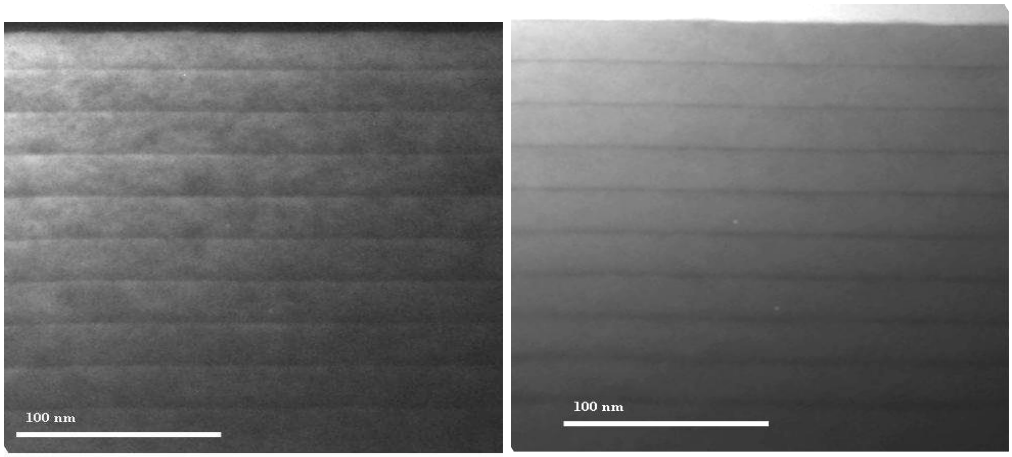

Figure 5.6 Conventional diffraction contrast TEM DF 200 (left) and BF (right) image of sample XMBE#11 taken with the beam approximately parallel to the <110> zone axes of GaAs substrate . The first InAs layer is just above the scale bar of the image

the <110> zone axes of GaAs nearly parallel to the electron beam. As can be seen the image does not show any contrast related to QDs in all of the ten InAs wetting layers. According to the PL results there may be small inhomogeneous dots on the surface

layer. These were not revealed in TEM images; however STEM images showed these small dots on the topmost InAs uncapped layer as will be discussed later. Figure 5.7, left hand panel, represents the same sample area imaged under DF conditions. The 10 period InAs/GaAs superlattice can be seen, and as in the BF image there is not any sign of QDs.

(b) Sample XMBE#12

In order to study the effect of GI on the critical thickness of the InAs layer TEM BF and DF images were taken. Figure 5.7 (left) shows a TEM BF image of sample XMBE#12. The parallel lines or stripes arise due to the strain in the wetting layers and the small speckle or dot-like contrast patches are related to embedded SOQDs within the whole ten periods of the structure. As the resolution in diffraction contrast images is restricted by the long range strain fields, it is difficult to make comments about the size of the features. The appearance of a higher concentration of dots in the layers near the bottom

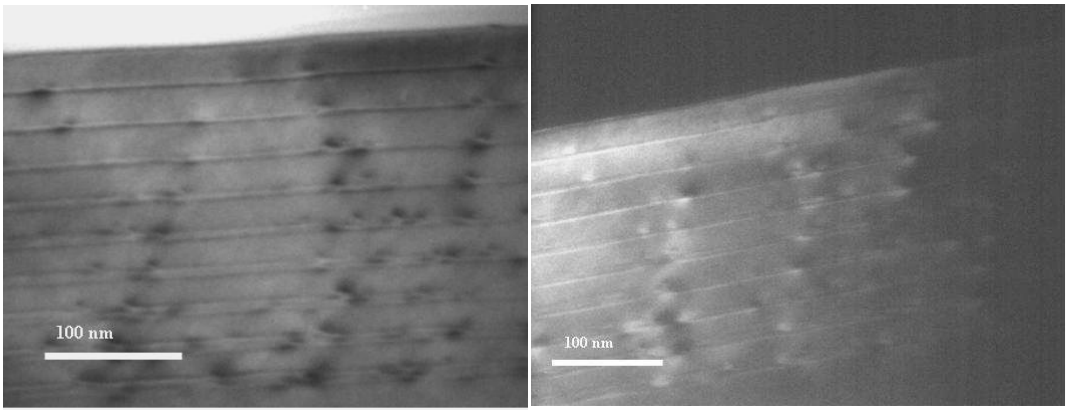

Figure 5.7 TEM BF (left) and TEM DF 200 image (right) of sample #12 with beam parallel to <110> zone axes.

of the image is due to the larger thickness of the sample in this region. Figure 5.7 (right) depicts a TEM DF image of a different area of the sample with the sample oriented at the same tilt angle as the TEM BF image. Bright spots are related to QDs.

5.3.4 STEM

In order to better understand the implication of the growth interruption for the formation mechanism, structural and compositional investigations were carried out via atomic resolution BF and HAADF imaging in an aberration corrected STEM.

(a) High Resolution STEM of sample XMBE#12

Figure 5.8 shows an atomic resolution BF STEM image (left) of a QD in sample XMBE#12, and the corresponding HAADF image (right). The images demonstrate that the dot height and lateral extent is 3-3.5 nm and 13-16 nm, respectively. Although small fluctuations in contrast arise partially from thickness variations or surface contamination there nevertheless appears to be some inhomogeneity of the In-distribution within the dot in the HAADF intensity. The latter is a function of Z^2 (atomic number) of the sample so that species with higher Z appear brighter compared to lighter species in the sample; this is why the In-containing QD in figure 5.8 (right) appears generally brighter then the surrounding GaAs environment. Fading of the intensity at the dot apex is due to the pyramidal shape and hence decreasing (increasing) amount of In (Ga) in the atomic columns. Areas of the wetting layer on either side (particularly on the left) of the QD are darker than the area joining the base of the dot; this may be due to the preferable migration of In adatoms from the wetting layer to steps at the island. This type of distribution of In around the QDs has been suggested as a result of the formation of dots on the top edge of steps and subsequent erosion of steps by the evolving dot [63, 73].

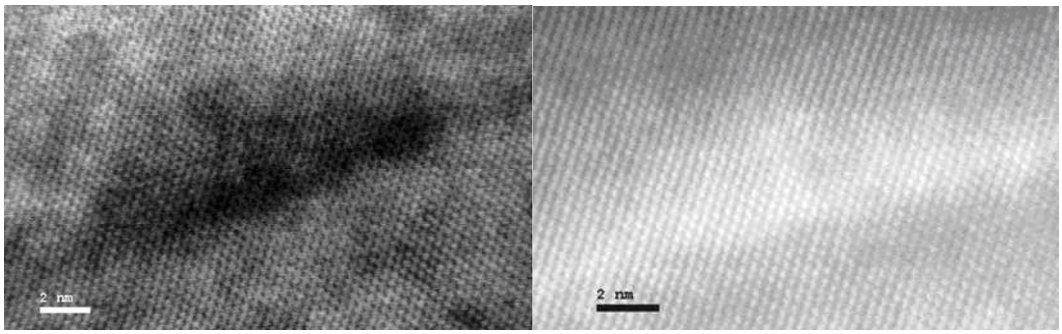

Figure 5.8 HREM BF (left) and atomic resolution HAADF (right) image of a QD in sample XMBE#12.

Close inspection of the HAADF image shows that the bottom interface of the wetting layer its sharper then the top interface, possibly caused by inter-diffusion with Ga as a result of migration of In toward QDs.

The following figure depicts the HAADF image of the entire 10 period QD stack in sample XMBE#12. The Z-contrast of the InAs wetting layers and QDs is clear. The QDs can also be seen as irregularities in the thickness of the wetting layers.

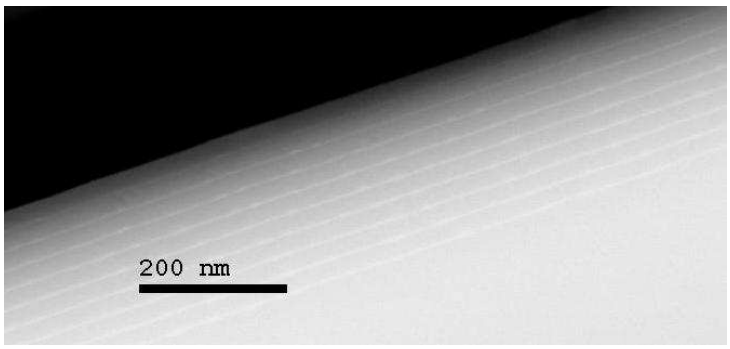

Figure 5.9 HAADF image of the entire 10 period QD stack in sample #12

(b) High Resolution STEM of sample XMBE#11

Figure 5.10 shows BF and HAADF STEM lattice images of a quantum well in sample XMBE#11. The Z-contrast indicates that wells and interfaces are far from mono-atomically flat and abrupt. The bottom interface has numerous atomic steps and the top interface is additionally diffuse. The dark areas in the GaAs spacer layers in the BF image are due to surface contamination.

As mentioned previously there was not any contrast from QDs observable in the diffraction contrast TEM images of sample XMBE#11 within the stack and neither was there strong evidence to suggest that QDs had formed on the topmost InAs uncapped layer, as would be expected according to PL results. However, in STEM such QDs were observed. Figure 5.11 represents an HREM BF STEM (top) and HAADF image (bottom) of QDs located on the uncapped top quantum well in sample XMBE#11.

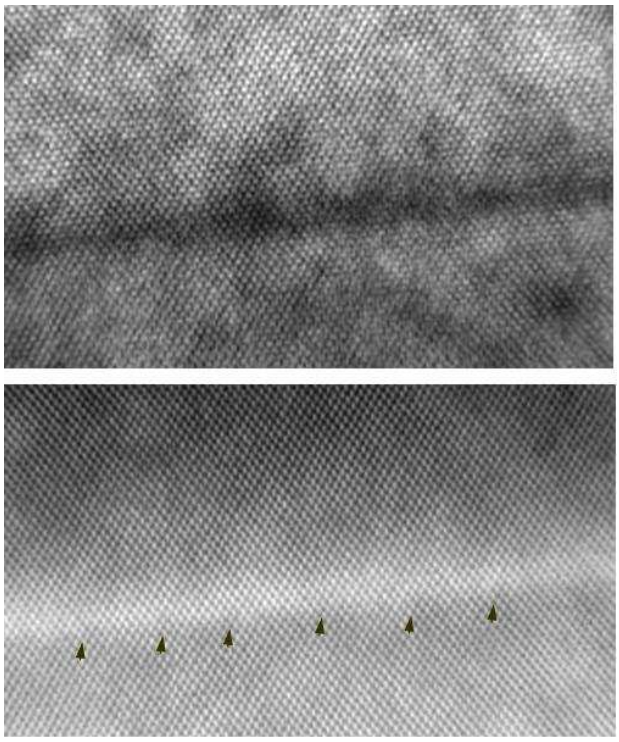

Figure 5.10 HREM BF (top) and atomic resolution HAADF (bottom) image of a quantum well in sample XMBE#11. The arrows indicate atomic steps in the bottom interface.

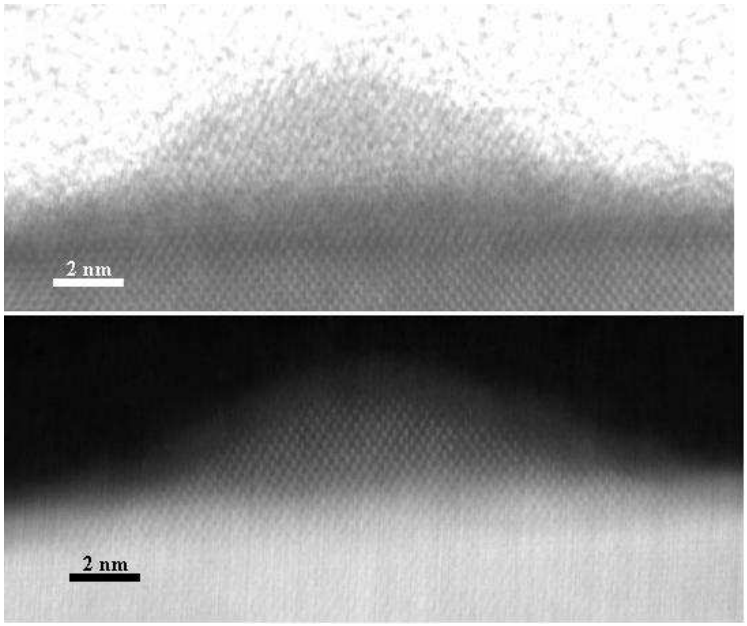

Figure 5.11 HREM BF STEM (top) and HAADF (bottom) image of a QD in the uncapped top quantum well in sample XMBE#11

5.3.5 EELS results of sample #12

In order to assess the composition of the QDs EELS was performed. The elemental distribution of Indium in the QDs was assessed by extracting maps of the relative intensity of the In-M5 absorption edge in the low-loss region of EELS spectra (<35eV). As mentioned in the introduction of this chapter KK analysis was employed to extract low-energy Ga- and In-edges as well as sample thickness from the imaginary part, $\varepsilon_{2,}$ of the dielectric function; NLLS fitting of a Gaussian peak with the energy window placed at 16-21 eV was employed to extract the In signal from the prominent feature, consisting of the combined In and Ga absorption peaks at 20 eV in ε_2. The In-intensity map was obtained by integrating the residual signal at 17.2-19 eV followed by dividing it by the integrated signal at 19.5-21.2 eV. Similar to the jump ration method, this procedure yields the relative In-distribution and removes thickness effects.

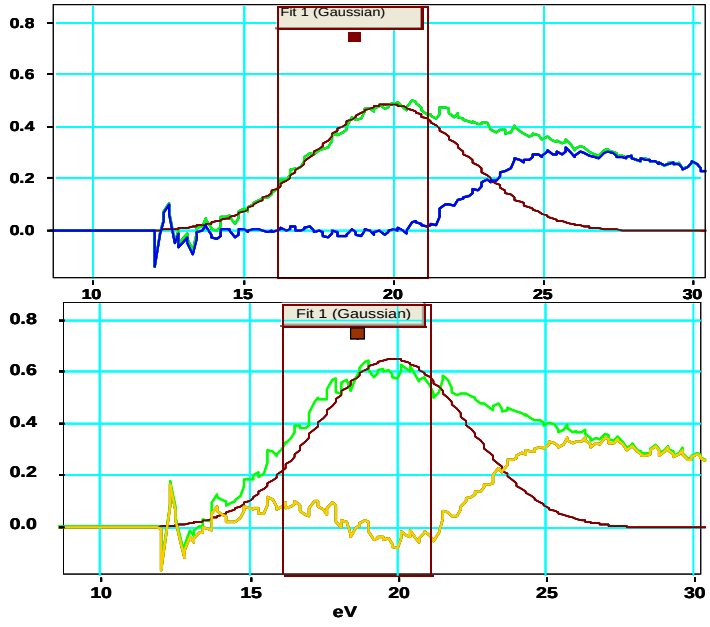

Figure 5.12. (top) ε_2 signal of GaAs (green curve) after applying KK and residual signal (blue) after NLLS Gaussian fitting on Ga 3d transition; (bottom) ε_2 signal of QD (green curve) and residual signal (yellow) with clear In 4d transition after NLLS Gaussian fit on Ga $M_{4,5}$ peak.

Figure 5.12 (top) shows ε_2 (green curve) obtained form KKA of an EEL spectrum from a GaAs region (blue square in figure 5.13 (top)) and figure 5.12 (bottom) shows ε_2 obtained from a QD-EEL spectrum (yellow square in Figure 5.13). NLLS Gaussian fitting was applied to the Ga $M_{4,5}$ edge in ε_2 to separate out the In feature. After NLLS Gaussian fitting the In-M4,5 edge in the QD is clearly visible (yellow curve in figure 5.12, bottom panel), whereas there is no sign of an In- edge in the GaAs barrier (blue curve in figure 5.12, top panel).

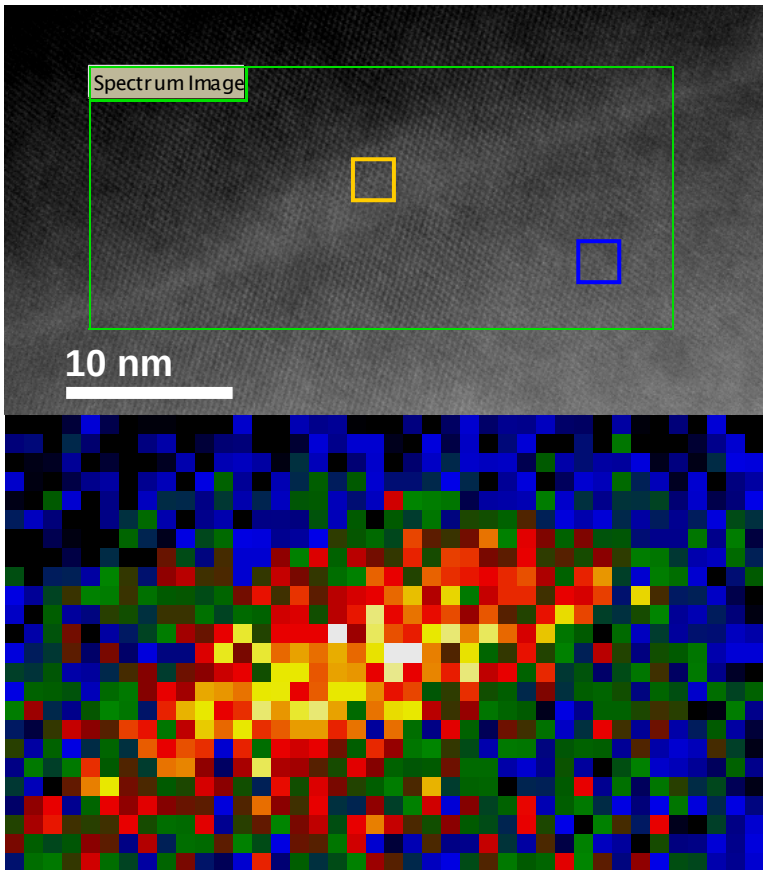

Figure 5.13 (top) HAADF image of a capped InAs quantum dot with green boxed area representing the SI area; (bottom) relative In-signal intensity in the QD after KK analysis and NLLS fitting applied to the related EEL SI.

Figure 5.13 (bottom) represents an intensity distribution of the In-M4,5 absorption edge relative to the Ga distribution, obtained from an EEL SI [15] of a QD shown in the

green boxed area in (top), where the In signal was extracted after applying KK analysis [74] as discussed above, to the entire SI. The contrast of the map is represented on the temperature scale with blue/black signifying low, and yellow/white high In concentration.

Occurrence of slight compositional fluctuations within is evident. The wetting layer adjacent to the dot appears to be 'pinched off', confirming the hypothesis that the In diffuses from some distance away into the dots thereby depleting the wetting layer.

We applied the KK sum role routine to obtain the thickness. Figure 5.14 represents the thickness profile in the area where the SI in figure 5.13 had been acquired. A value of ~80 nm for the absolute thickness (see Figure 5.15) of sample XMBE#12 can be derived. Assuming a pyramid-shaped dot [71] and using QD dimensions as derived, (lateral 16 and height 3nm), the volume of the dot is ~260 nm^3. From TEM images we furthermore derive a dot density of ~1 per 1000 nm^2; hence the dot volume is about 3-4 times the amount of the differences between the volumes of the wetting layers in the samples XMBE#11 and XMBE#12. This discrepancy in volume can be explained by additional material participating in the formation of QDs originating from the GaAs spacer layers as a result of In segregation, thereby forming a ternary alloy of InGaAs within the dots.

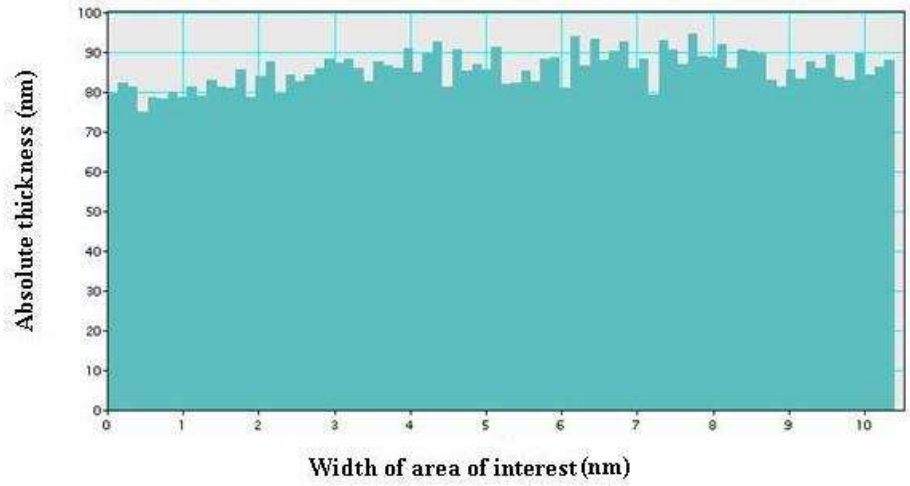

Figure 5.14 Absolute thickness of sample XMBE#12 in the dashed area of figure 5.14 after K-K analysis

5.3.6 EELS results of sample XMBE #11

Figures 5.15 and 5.16 present EELS low loss and HAADF investigations of sample XMBE#11.EEL SIs of this sample had been acquired in the same instrument and with the same acquisition parameter as sample XMBE#12. EELS evaluation techniques used to study sample XMBE#11 were the same as with sample XMBE#12. The In-signal map and atomic scale HAADF lattice image in figure 5.15 clearly show the diffusion of In into GaAs barrier layer. The interface in both sides of the well is far from abrupt and flat.

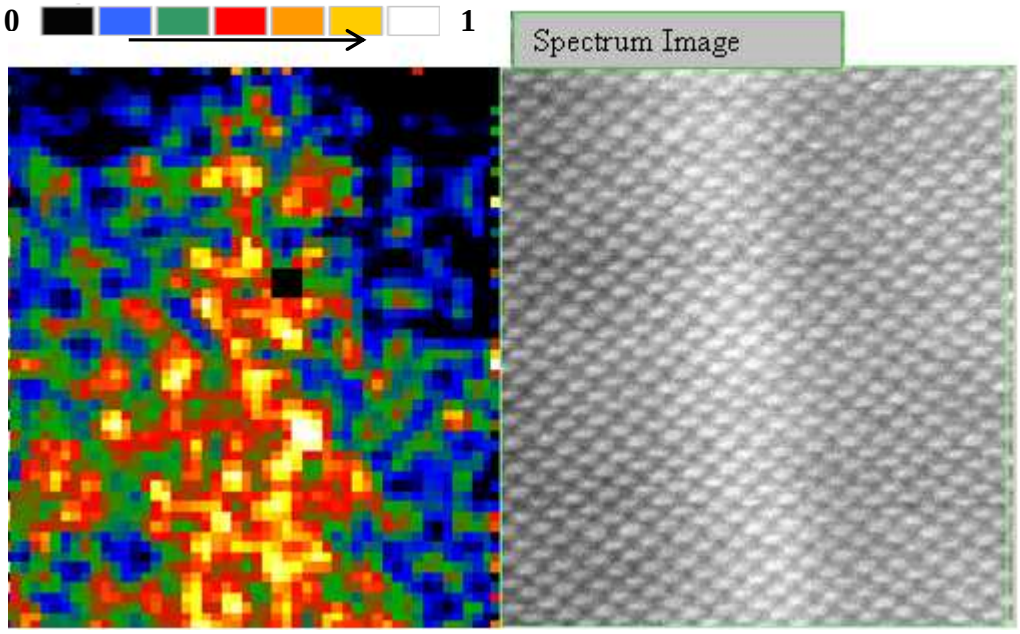

Figure 5.15 (left) In-signal intensity map obtained from an SI of the area of a In(Ga)As QW shown in HAADF image on (right) after KK analysis and NLLS fitting. The relatively weak In-EELS signal results in a small signal to noise ratio; hence the appearance of orange areas outside the QD, there is however a larger concentration of such areas in the wetting layer

PL indicates that there are possibly QDs in the uncapped top layer, which would have formed after growth stopped in a similar fashion as the dots in each layer of the sample XMBE#12 have formed after a GI. This is demonstrated in the HREM HAADF image

and the intensity map of the M4,5 In-edge in Figure 5.16, which reveal, indeed, the existence of small dots in the top InAs layer. This is more supporting evidence for the role of GI at the critical thickness in the formation of QDs: in the same sample there is no sign of QD formation in buried, continuously grown QWs, whereas at the end of growth, i.e., on the surface dots are formed.

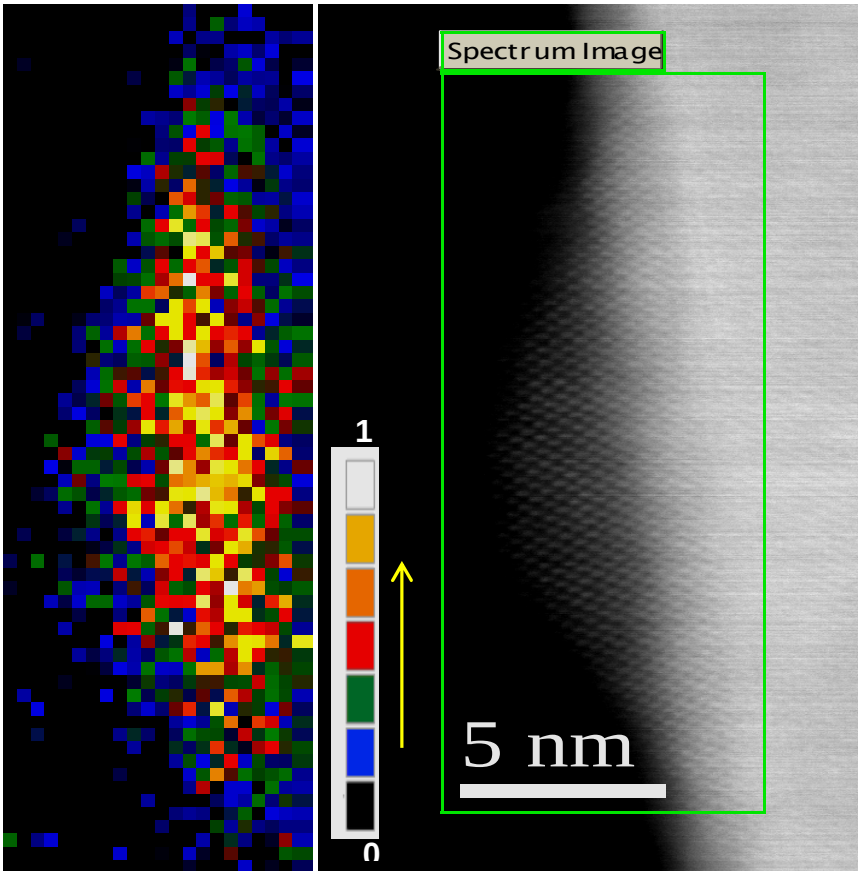

Figure 5.16 Atomic scale HAADF STEM image (right) of the uncapped top quantum well in sample XMBE#11 together with the intensity map of the In $M_{4,5}$ edge (left).

5.4 Geometric Phase Analysis (GPA) of InAs/GaAs QDs

In this section strain analysis of buried InAs QDs in GaAs layers using GPA is carried out. In this analysis the lattice spacing of the GaAs spacer planes is taken as reference.

In GPA HRTEM images are Fourier transformed and Bragg spots of interest are masked. As the structure is not a perfect crystal there are variations in amplitude and phase of the Bragg reflections. These variations are processed as a function of position in real space. Two Bragg spots of the GaAs (111) planes in the Fourier transform of the noise reduced HRTEM images (Figure 5.17a) were selected to carry out the analysis (Figure 5.17b). Other than (200) spots which are compositionally sensitive one can select any other Bragg spots [75]. To reduce the noise level in the HRTEM images a Wiener filtering technique which is a function of the GPA programme (STEM_CELL)[76] has been used. Noise is imposed by the CCD camera during digitization or by amorphous layers on the bottom or top side of the sample. To isolate the selected Bragg spots a mask was placed around these spots. The strain calculation using Equation (2.21) was performed. The resulting strain maps were calibrated against a reference region in the GaAs spacer.

Figure 5.17 (c, d) represents the resulting strain in the growth direction (figure 5.17c) and the in-plane direction (figure 5.17d). The InAs QD layer appears clearly in this direction with highest strain in the centre of QD. There is no significant in-plane strain. In growth direction a strain value of ~7% for the middle of the QD is derived, which corresponds to an In-fraction of 65% (see table 5.1), according to equations 5.1-5.4. In the vicinity of the QD in the QW the map represents ~3% deformation for the lattice parameter in growth direction.

The local lattice parameter $a_{AxB1-xC}$ for a ternary alloy $A_xB_{1-x}C$, and the resulting mole fraction, x, for element A according to Wegard's law is[77]:

$$a_{AxB_{1-x}C} = xa_{AC} + (1-x)a_{BC} \Rightarrow x = \frac{a_{ABC} - a_{BC}}{a_{AC} - a_{BC}} \quad (5.1)$$

here a_{AC} and a_{BC} are lattice parameter of the binary alloys InAs and GaAs respectively.

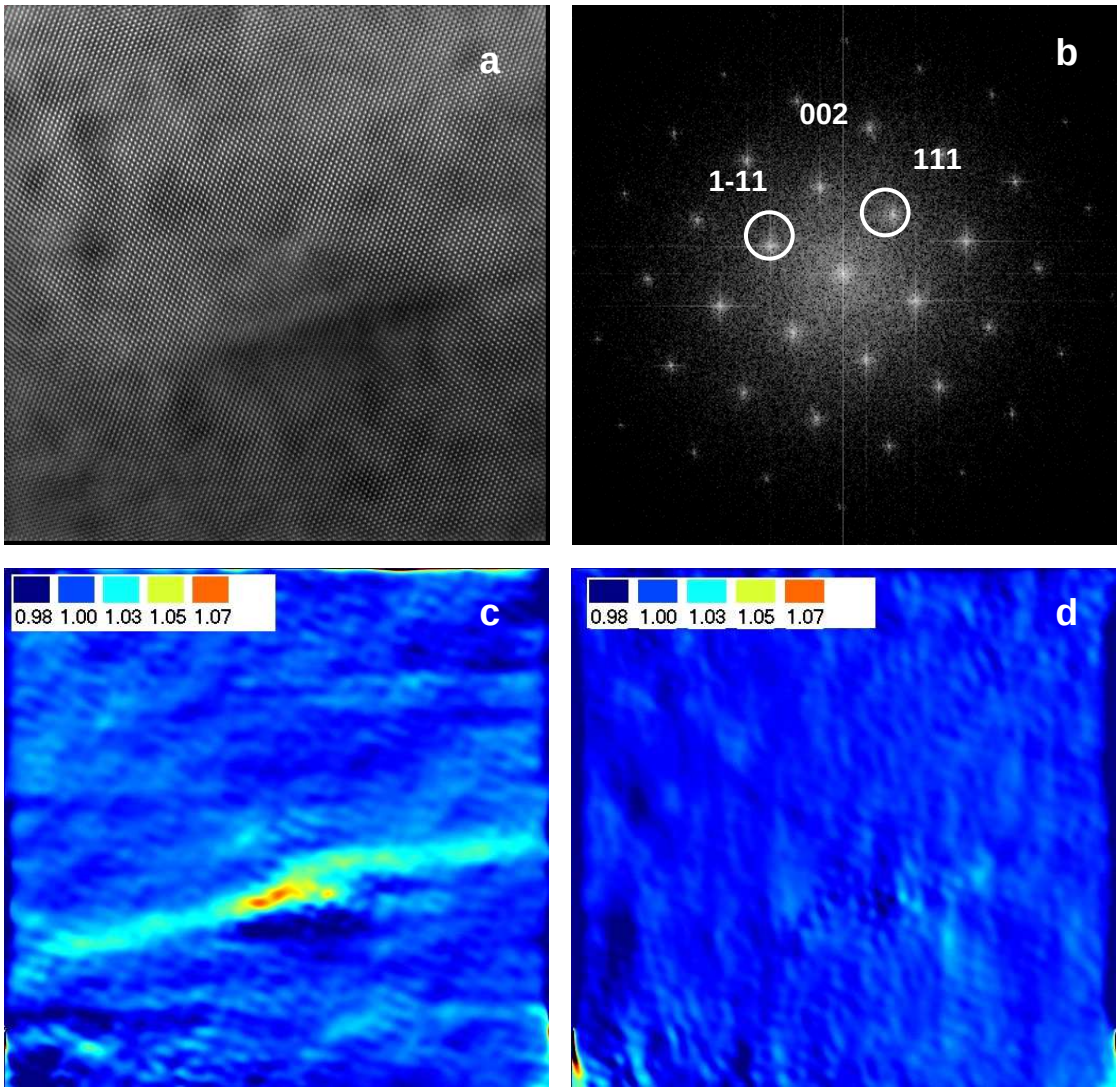

Figure 5.17 (a) HRTEM image of a buried QD after applying a Wiener filter, (b) FT of (a) with circled reflections used to calculate the strain map in growth direction (c) and in-plane (d). The colour scale represents the strain value with the value of 1 representing zero strain.

The lattice parameter of a unit cell parallel to the interface is imposed by the lattice parameter of the spacer layer, GaAs, whereas the lattice parameter in growth direction can vary locally due to the change in the composition of the material. The relationship between the calculated lattice parameter perpendicular to the interface and the local bulk lattice parameter is given by equation [77]:

$$\frac{a_S - a_\perp}{a_S} = A\frac{a_S - a}{a_S} \quad (5.2),$$

Where

$$A^{thick}_{<100>,<110>} = \left(1 + 2\frac{C_{12}}{C_{11}}\right) \approx 2 \quad (5.3)$$

$$A^{thin}_{<100>} = \left(1 + \frac{C_{12}}{C_{11} + C_{12}}\right) \approx 1.3 \quad (5.4)$$

$$A^{thin}_{<110>} = \left(1 + 4\frac{C_{44}C_{12}}{C_{11}^2 + C_{11}C_{44} + C_{11}C_{12} - 2C_{12}^2}\right) \approx 1.5 \quad (5.5)$$

In these equations a is the local lattice parameter and C_{ij} are the elastic constants of the strained InAs QD layer. As the sample in this experiment is sufficiently thin [77] for an electron beam parallel to the <110> zone axis we can use equations 5.5 and calculate the lattice parameter, a, and the In mole fraction, x, in the InAs QD layer represented in Figure 5.17. Table 5.1 shows a and x values in different locations of the Figure 5.17 represented in temperature scale.

Strain Value	**1.00**	**1.03**	**1.05**	**1.07**
$a_\perp$	5.6533	5.8229	5.9360	6.0490
a	5.6533	5.7664	5.8420	5.9171
x	0	0.28	0.46	0.65
Composition	GaAs	$In_{0.28}Ga_{0.72}As$	$In_{0.46}Ga_{0.54}As$	$In_{0.65}Ga_{0.35}As$

Figure 5.18 Calibration of the colour scale in figures 5.17 (c) and (d): lattice parameter in growth direction, $a_\perp$, calculated a using $a_\perp$ values and In mole fraction x.

5.5 Conclusion

Investigations using different electron microscopy methods were carried out on two kinds of sample, grown at the critical thickness (corresponding to 1.77ML InAs layers) by Molecular Beam Epitaxy on ~25 nm GaAs spacers with and without growth interrupt. It was found that applying a GI of 60s after the deposition of InAs leads to formation of self-assembled QDs in each wetting layer whereas continuous growth does not result in QDs in buried layers. Conventional TEM showed the formation of SOQDs in the sample with GI and revealed that there were not buried QDs in sample without GI. TEM did not reveal dots at the topmost InAs layer of sample without GI in contrast to PL spectroscopy investigations and STEM images that evidenced existence of QDs in surface layer of this sample.

Conventional TEM cannot reveal microstructure of such thin layers in sufficient detail; so in order to see atomic-scale distribution of In and to help explain the dynamics of the dot formation in the 1.77 ML sample after GI, atomic-lattice resolution HAADF images were acquired and EELS investigation performed to reveal the elemental distribution within the dots.

In the case of the sample with GI intensity profile investigation on HAADF images showed the dots height and lateral extent was 2.8-3.2 nm and 13-16 nm respectively.
KK analysis was applied to extract In intensity maps of QDs. The extracted map reveals an inhomogeneous distribution of In within the dots and revealed that the wetting layer near the dot is ‘pinched off’ because of migration of In adatoms from the wetting layer to the dots.

In the case of the sample without GI appearance of atomic steps in the bottom and also diffuse top interfaces of the wetting layer were observed. The immediate growth of GaAs after InAs inhibits diffusion and segregation of In adatoms, and In-Ga intermixing leads to reduction of the strain in the wetting layer. In support of the above conclusions the atomic resolution HAADF lattice images of nominal 1.77 ML InAs in superlattices

without apparent dot formation suggest considerable roughness on the scale of 1-2 monolayer and step separations of ~10 nm.

According to these results the suggestion for the formation mechanism is segregation of In adatoms to step edges which act as sinks and increase the strain in these areas and relieving strain by the diffusion of Ga adatoms from the substrate which leads to erosion at the edges of islands and evolution of dots of an InGaAs alloy with inhomogeneous composition.

GPA clearly shows lattice distortion in the InAs QD layer especially where the QD has formed. According to this evaluation method, inside and close to the top of QD the maximum In mole fraction is only 0.65 showing that no pure InAs dots were formed. The compositional findings of the GPA for the QD layer support the KK analysis leading to the qualitative EELS elemental maps of In distributions in the QD layer. The wetting layer in the vicinity of the QD is showed to be an $In_xGa_{1-x}As$ ternary alloy phase with maximum In mole fraction of 0.28.

6

Er and Si NCs doped Silica

6.1 Introduction

Silicon (Si) is one of the most abundant and used elements on the planet. It is the main ingredient of glass and one of the cheapest elements with excellent electrical and mechanical properties. Similar to other group IV elements Si has a face centered cubic (f.c.c) structure with a tetrahedral unit cell (see figure 3.8). Its lattice parameter is ~5.430710 Å Each Si atom has 10 core electrons (tightly bound), and 4 valence electrons (loosely bound) [78].

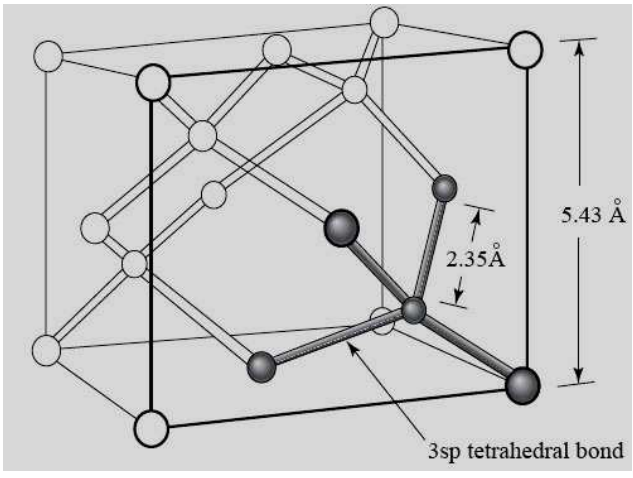

Figure 6.1 Unit cell of silicon [110].

Bulk Si is an indirect bandgap semiconductor with poor optoelectronics properties. It would be a most desirable property of this material to emit light efficiently and to be integrated with electronically and optically functionalized devices based on current mature Si technology. However, due to its indirect bandgap it has been recognised as

unsuitable for optoelectronics devices. First experimental results of room temperature Photoluminescence (PL) reported about two decades ago were of Si-NCs in silica implanted with Si [79] and of porous Si [80]. Furukawa *et. al.* were the first research group to observe excitation of visible light from Si in connection with the three dimensional confinement effect in silicon NCs [81]. The authors examined their samples by means of PL and Raman experiments and reported room temperature PL at 2.4 eV from 2-5 nm Si-NCs. This work was overlooked for a few years and after this, the observation of light emission from porous silicon [80] spurred huge interests in the study and synthesis of Si-NCs. The origin of the visible emission of Si-NCs in silica has been the subject of an intense debate for years. Causes other than the quantum confinement effect [80, 82, 83] were ascribed to highly localized interfacial defects [84]. Multiple Si=O bonds at the surface of NCs [85] have been proposed as the origin of room-temperature PL in Si-NCs in silica. In a very recent study conducted by Godferoo et. al., the authors have reported that quantum confinement and interfacial defects are the two main causes, with the latter one being the dominant source of the light from Si-NCs [86].

Apart from intrinsic visible light emission, it had been reported that incorporation of erbium (Er) in the bulk Si lattice resulted in infrared emission of 1.54 µm, which is characteristics of 4f shell transitions in rare earth elements. This sharp atomic-like emission can be produced by both optical [87] and electrical [88] excitations. The major obstacle in the progress of the Er-doped bulk Si for light emitting prospects is the dominant thermal quenching at room temperature [88, 89]. It has been reported that broadening of the band gap of the Si host, e.g., in porous Si, amorphous Si nanoclusters and Si-NCs can suppress room temperature thermal quenching [3, 90]. Auger recombination (decay via energy transfer to the free carriers [91]), and back-transfer (de-excitation by formation of new electron-hole pair [92]), are the two main causes of non-radiative de-excitation of Er ions by transferring energy to Si-NCs. This process is less efficient in NCs than in bulk Si because of the larger energy mismatch for the process. Indeed, widening of the bandgap reduces the concentration of free carriers, thus suppressing the Auger process.

On the economy/ industrial/ technical side the first transatlantic telephone line based on the analogue coaxial system was completed in 1956 between Scotland and Newfoundland. The signals had to be amplified every 10 km in stages called repeaters to result in sufficient electrical signal at the end of the line. This kind of line was not sufficient for the growing demand on telecommunication industry. The research on the first generation optical fibres started in the early 70's. Rapid growing demand for high data transmission rates such as the internet has excited global technological interest. Er-doped silica is the material used to produce fibre optics in telecommunication industry in order to achieve high data transmission rates. Silica fibres are the medium used for transmission of laser pulses in long-haul optical telecommunication networks across the globe to deliver huge amounts of data in a matter of seconds. Figure 6.2 shows the world's under-sea optical fibre network which consists of hundreds of thousands of kilometres in length. The transatlantic fibre optic length is about 6000-7000 km and that of the transpacific fibres is 9000-11000 km.

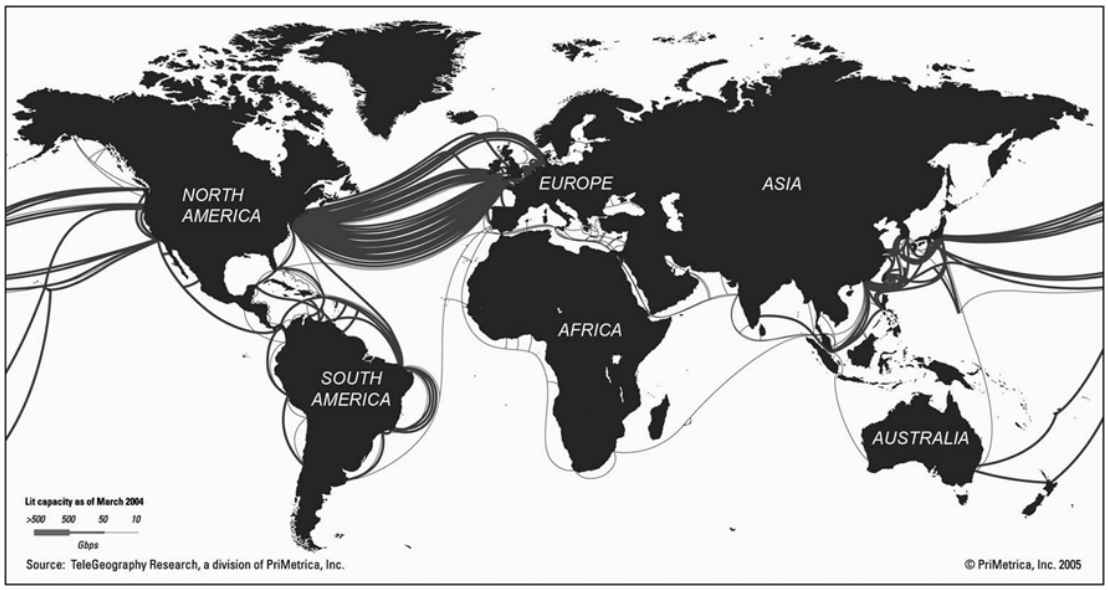

Figure 6.2 Global fibre optics network [93]

The main difficulty of optical data transmission is the absorption of light in the fibre. Figure 3.10a represents the optical attenuation of silica as a function of transmitted laser wavelength. As can be seen, silica has an absorption coefficient of few percent per

kilometre (~0.2 dB/km) at 1.54 µm which is the strategic wavelength in optical telecommunications. This wavelength is produced by intra band transitions in the 4f shell, ${}^4I_{13/2} \rightarrow {}^4I_{15/2}$, of rare earth ions. Figure 6.3b depicts energy levels of Er in silica and the bandgap of silicon. The amplification of this special wavelength, using current Si technology in terms of Er-doped bulk Si and SiO_2 is one of the most intense areas of research for semiconductor scientists.

As mentioned above, intense thermal quenching of the PL emission at 1.54 µm of Er

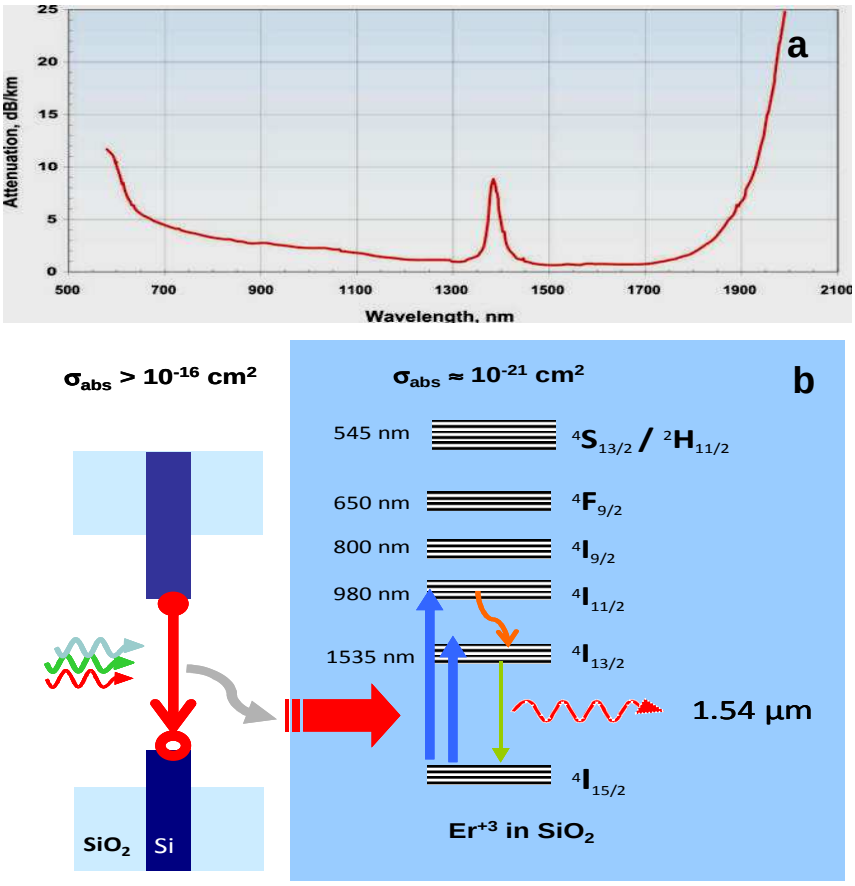

Figure 6.3: a) attenuation of silica glass; b) Energy diagram of 4f levels in Er^{3+}. On the left-hand side the band diagram for a Si NC is shown and on the right-hand side the splitting due to the interaction with the crystalline field in a solid is depicted [111].

ions in bulk silicon has hampered commercialization of this structure. Optical amplifiers based on SiO_2 doped with moderate concentration of Er ions are currently used [94].

PL spectra of Er in silica show a peak at 1.54 µm. This indicates that excitation of Er ions in silica takes place through a transition from the first excited state of Er ions to the ground state. By changing the pumping wavelength the resonance condition changes and the PL emission intensity at 1.54 µm dramatically reduces. On the other hand, the 1.54 µm emission of the Er-doped Si structure shows no significant intensity changes when tuning the pumping wavelength, which is indication of indirect excitation of Er ions by electron-hole mediated processes. Figure 6.4 shows low temperature PL emission of Er doped silica with the principal Er related luminescence peak at 1.54 µm.

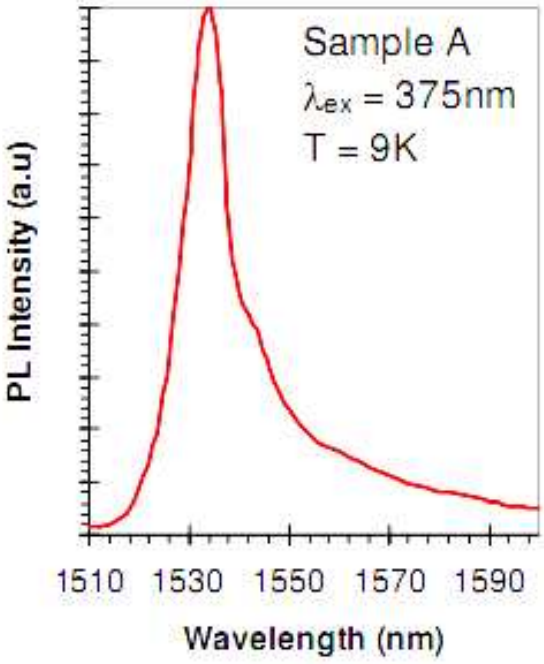

Figure 6.4 Low temperature Er PL spectrum from Er doped silica. The principal luminescence peak occurs at 1.54 µm.

The spacing between repeaters for Erbium Doped Fibre Amplifiers (EDFA) is 50-90 km and in current transatlantic fibres 75 repeaters have been installed to transmit data. Apart from economical disadvantages arising from higher numbers of low gain repeaters, there are also technical problem such as noise accumulation. Increasing the

gain of the amplifiers and reducing the number of the repeaters will lead to enhancement of the signal to noise ratio (SNR) and capacity of the optical network [93]. As Er has a low absorption cross section (~10^{-21} cm^2), in order to achieve strong emission at 1.54 µm high concentrations of excited Er ions are required. On the other hand high Er doping leads to Er clustering (leading to structural inhomogeneity and reduction of the excitable fraction of Er ions) and Er^{+3}- Er^{+3} up-conversion interactions resulting in a reduction of the gain of the devices [95]. To tackle these problems Si-NCs have been incorporated into silica, representing one of the most promising structures for future enhanced EDFA [3, 5, 96-98]. The Si-NCs in this system provide much larger absorption cross sections (~10^{-16} cm^2) in the visible range compared to Er and act as sensitizer for the Er^{+3} ions.

In an early study researchers observed that Er in Si-rich silica provides ~1.5 µm wavelength emission at room temperature even by using excitation wavelengths other than the characteristic Er absorption wavelength [99]. In their work they claimed a probable energy transfer from Si to Er ions. Intense research regarding this new structure continued and a few years later further evidence of coupling between Si-NCs and Er ions was reported [97]. In this later publication, strong correlation of the luminescence peak of Si-NCs at ~0.81 µm and that of Er 4f transition at ~1.54 µm has been observed. A rise in the concentration of excess Er in the structure resulted in an almost linear increase of the 1.54 µm and a rapid decline in the 0.81 µm emission. This suggests that Si-NCs are coupled with Er ions and quench through a non-radiative process by transferring their energy to Er ions. Kik et. al. studied a structure produced via ion implantation [100]. The authors claim that the excitation efficiency of Er ions by excitons confined in Si-NCs was more than 55% and every NC could excite only one Er ion. Hence Si-NCs with a much higher absorption cross section compared to that of Er, act as photo-sensitizer to Er ions [3, 101]. The sensitization of Er by Si-NCs has been modelled as dipole-dipole short range interaction [5, 102].

Further insight into silica doped with Si-NCs and Er will enable us to understand the composition and structure of the material and specify the site of Er and Si-NCs with respect to each other in order to determine the best growth conditions to achieve material with optical properties applicable to silicon photonics. To achieve an

understanding of the sensitization phenomenon a large body of work so far has focussed on optical properties of Er-doped Si-NCs. In these studies it has become clear that the Er environment and Si-NCs play a significant role in light emission. However, little research by means of analytical electron microscopy to understand compositional properties of such materials has been carried out up to now. In this part we will present a structural and compositional evaluation of this material using some of the most advanced analytical electron microscopy techniques.

6.2 Sample design

In order to study Er-implant related microstructure and composition three types of samples were compared. These consisted of (A) solely Er-implanted SiO_2, (B) an Er:Si-NCs system where Si and Er were co-implanted into a thermally grown oxide layer, followed by an annealing stage, and (C) an Er:Si-NCs system, where Er-was first implanted into a Si-substrate, which was oxidized and subsequently Si-implanted and annealed. The Si-ion energy and dose in cases B and C, were 80 keV and 8×10^{16} at/cm^2, respectively. In all samples Er^{+3} ion implantation was carried out at 320 keV and a dose of $3x10^{15}$ at/cm^2. Post implantation the samples were annealed at 1100 ^oC in an N_2 ambient for 1 hour in order to form the Si-NCs.

The Er peak concentration in the samples was $3x10^{20}$ cm^{-3}, the silicon peak concentration $8x10^{21}$ cm^{-3}. A short (10 minute) lower temperature (500^{o}C) treatment of the samples in an N_2:H_2 (5%) atmosphere was carried out to passivate 'dangling bond' (P_b) SiO_2/Si-NC interface type defects.

Figure 6.5 is a schematic representation of the three samples known as sample (A), (B) and (C).

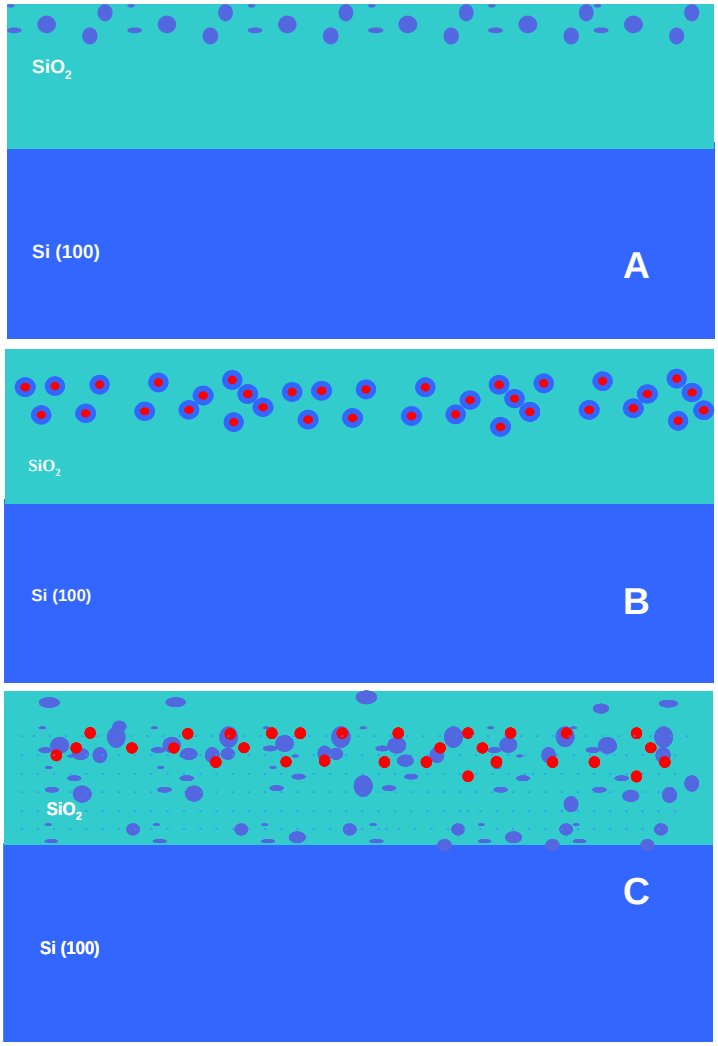

Figure 6.5 Schematics of the three samples with red circles showing Si-NCs and blue features representing Er rich areas: (A) solely Er-implanted SiO_2 (B) Er and Si co-implanted and (C) Er and Si sequentially implanted. Er-clusters are blue and Si-NCs red.

6.3 PL characterisation

The PL investigation was carried out at the Photon Science Institute of the University of Manchester by Dr Iain Crowe. PL measurements were performed on the three samples in order to investigate the best growth mechanism to achieve intense PL emission at1.54 μm, the wavelength of Er. Due to the short-range character of the Er-Si NCs interaction, the spatial distribution of Er in the matrix compared to the position of the Si-NCs is quite important. A high number of excitable Er ions for each NCs is the ultimate goal.

However Er-Er back transfer and possible non-luminescent $ErSi_2$ formation are major drawbacks of high-dose Er implantation.

To perform the room temperature PL experiment, the samples were excited with 0.02 to 10mW of optical power using a CW 375 nm solid state coherent cube laser diode, and the PL emission was detected with a N_2-cooled InGaAs array detector. Samples were mounted on the cold finger of a recycling helium cryostat for low temperature PL investigation and photo-excitation was provided by the 375 nm laser diode at 10.3 mW. The PL data were detected using an N_2-cooled Edinburgh Instruments EI-L single channel Germanium detector.

In order to study the sensitization mechanism and the role of excess Er in the optical properties, further to the samples for TEM measurements, samples with different Er concentrations and the same concentration of the implanted Si were provided for PL measurements. Figure 6.6 shows the effect of increasing Er concentration on (a) the nano-crystal and Er luminescence spectra and (b) their peak intensities. The broad peak

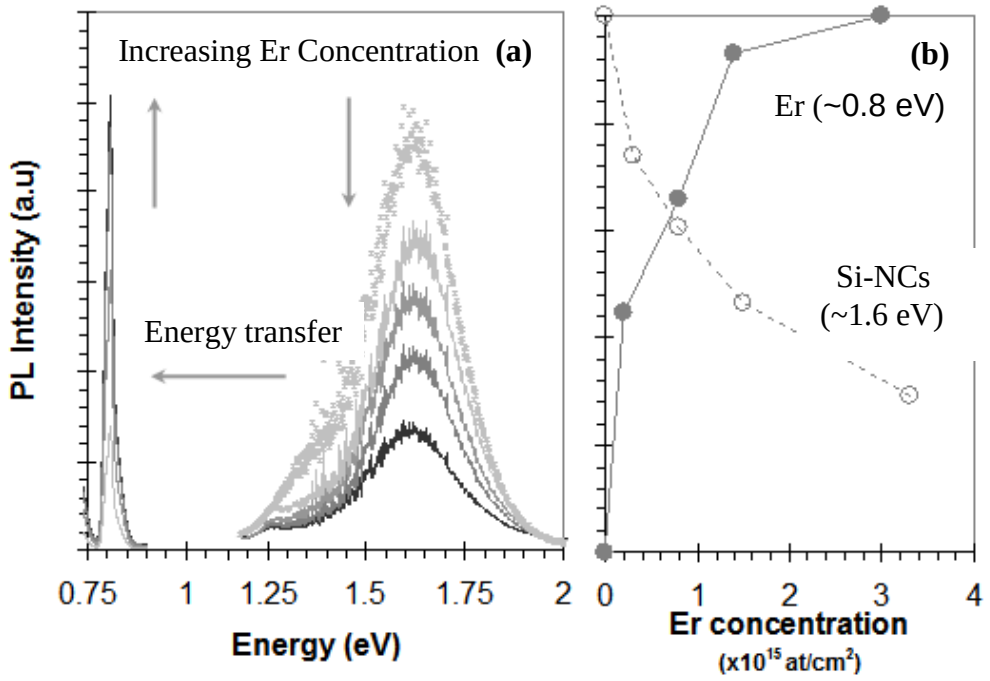

Figure 6.6 (a) PL spectra of Si NCs formed in SiO_2 containing different concentrations of implanted Er and (b) peak intensities of Er(~0.8 eV)and Si NCs (~1.6 eV) PL emission for different Er concentration.

at ~1.6 eV is caused by recombination of confined electron-hole pairs in the Si-NCs. The energy of these peaks is higher than the band gap of bulk Si as a result of confinement of the charge carriers within the NCs. The broadening of the peak is caused by the variation in the size of Si NCs. Sharp PL peaks for different Er concentrations at ~0.8 eV correspond to radiative transitions in the Er ions from first excited state to ground state. As the concentration of excess Er in the sample increases the intensity of luminescence emission of Si-NCs decreases and in turn the PL intensity of Er increases.

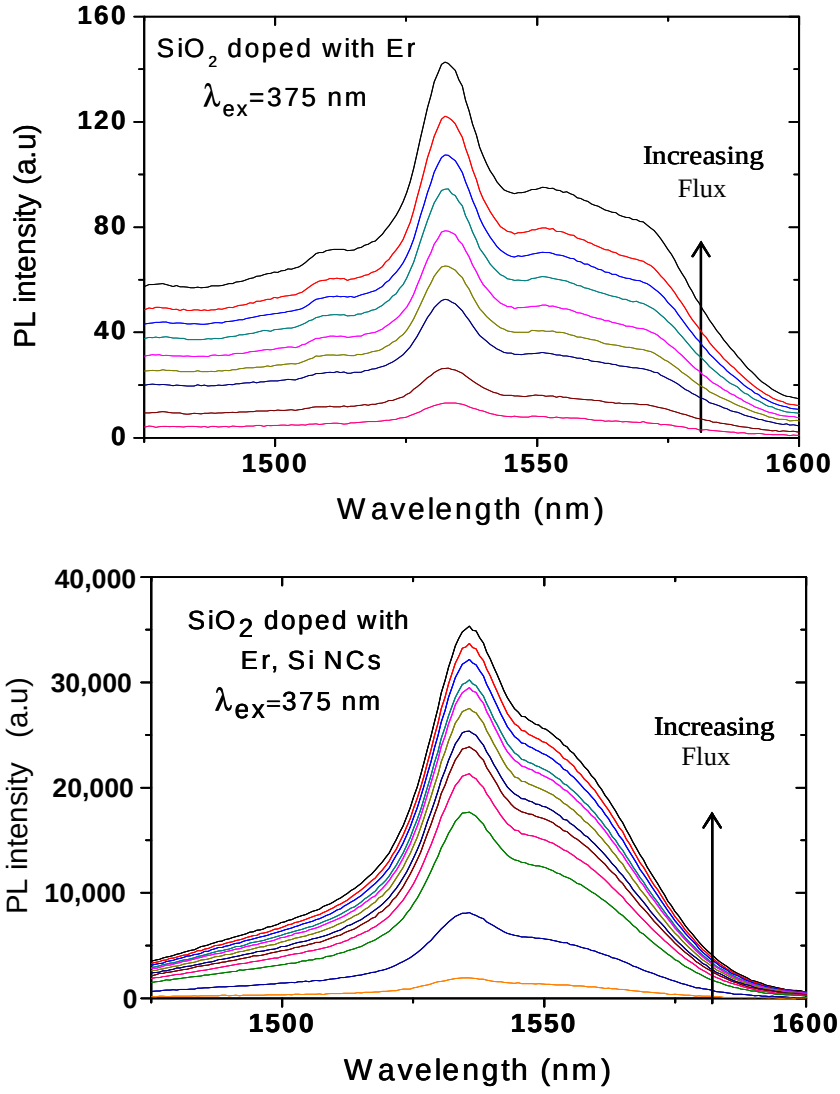

Figure 6.7 PL spectra of sample A (top) and sample B (bottom) as a function of excitation flux ($\varphi = 1\times10^{17}$–4.5×10^{19} cm^{-2} s^{-1})

In other words, increasing the Er ions in the structure leads to the coupling with Si NCs and this result in quenching of the NC PL by transfer of energy to Er ions and this makes the NC optically dark.

To study the effect of growth methods and parameters on the optical properties of the Er:Si-NC system, PL was then carried out for sample A, B and C. Figure 6.7 (top) depicts the flux intensity dependence of room temperature PL emission of sample A for fluxes φ in the range of 1×10^{17}–4.5×10^{20} cm^{-2} s^{-1}. The peak at 1.54 μm which is characteristic of the Er, $I^4_{13/2} \rightarrow I^4_{15/2}$ excitonic transition is clearly visible for all measured fluxes. A linear dependence of the Er emission on the flux intensity can be observed. The low Er absorption cross-section, on the order of ~$10^{-21}cm^2$ [6], results in a relatively low PL photo-excitation intensity

Figure 6.7 (bottom) shows PL measurements for sample B with a similar PL set up and pump flux. Er related peaks at 1.54 μm can be seen at similar wavelength to that of sample A.

Other than the nonlinear dependence of the 1.54 μm emission on the pump flux there is a significant enhancement in intensity of PL emission. The PL Er $I^4_{13/2} \rightarrow I^4_{15/2}$ emission in sample B appears to be ~400 and ~250 times more intense than that of sample A for the lowest and highest pump flux respectively. The only difference between the two samples was the implantation of excess silicon in sample B, resulting in the formation of Si NCs, otherwise the two samples had similar layout and growth conditions.

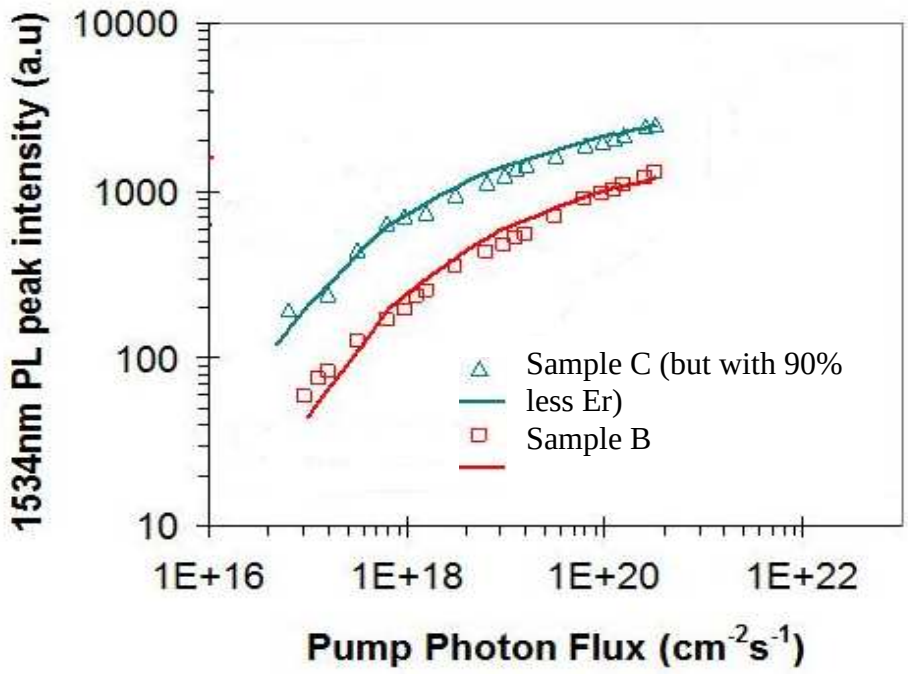

Figure 6.8 Comparison of Erbium emission from samples prepared by sequential and co-implantation

Figure 6.8 shows the Er PL peak intensity from a sample prepared with the same implantation and annealing procedure as sample C, but with 90% less Er in comparison with that of sample B. At lower pump flux the sequentially implanted sample shows ~5 times and at high pump flux still ~2 times more intense PL emission compared to that of its co-implanted counterpart. The Er-concentration was ~10% of that of sample C, which was used for TEM measurements, however, PL measurements (not presented here) proved that the higher Er concentration (in C) does not improve the efficiency of PL emission much. Overall it thus appears that sequential implantation and annealing led to improvement in optical properties of the material.

This improvement in the optical properties of sample B (co-implanted) compared to the solely Er implanted silica sample (A) as well as the enhancement in PL emission of the sequentially implanted sample (C) compared to that of the co-implanted sample (B) is addressed in more detail in the following paragraphs via structural and compositional

investigations in order to give a better understanding of the light emission process so as to optimise the design of these structures for potential device applications.

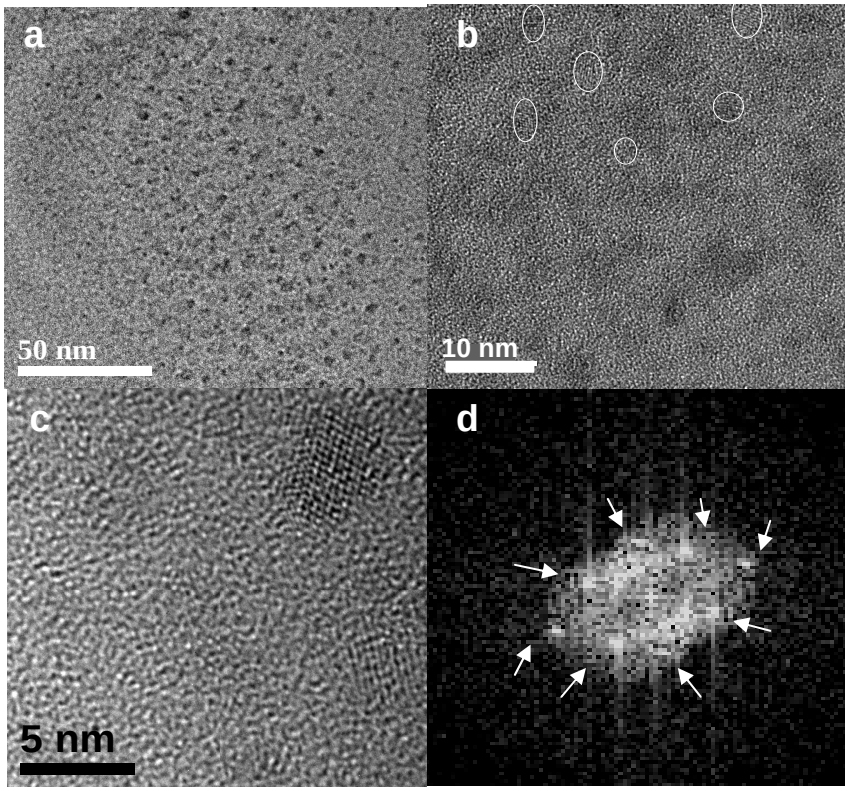

Figure 6.9 (a) low magnification diffraction contrast view of NCs in the co-implanted sample B. (b) HRTEM phase contrast image with NCs (in white circles), (c) close-up of a NC with clear lattice fringes . (d) FT of NC in (c) showing presence of eight diffraction spots of the 110 zone axis pattern Si.

6.4 Co-implanted Er and Si in silica (sample B)

Samples were firstly studied with diffraction contrast TEM and HRTEM in a Tecnai with field emission gun (FEG) operated at 300 KV with the sample aligned along the <110> zone axis of the silicon substrate. Figure 6.9a shows a low magnification diffraction contrast view of features located within a band inside the silica matrix layer. HRTEM image in figure 6.9b reveal the presence of Si-NCs in the band and figure 6.9c

represents one of the NCs with a clear view of different lattice fringes. The FT of the NC of figure 6.9d showing eight diffraction spots of the <110> zone axis proves the NCs has an fcc structure. No big Er-oxide clusters were seen in these images as was observed in solely Er-doped silica sample and will be discussed later. This is an indication of the role of excess silicon in the clustering or precipitation behaviour of the Er.

Further structural and compositional investigations were necessary to give a deeper understanding of the nanostructure of the sample. To assure overall crystallinity of the Si-clusters, diffraction contrast TEM-DF images were captured in different sample orientations. Examples are shown in figure 6.10. Bright spots in the images show lattice planes reflections of the NCs for g-vectors <022>, <111> and <200> over the dark background of the amorphous matrix.

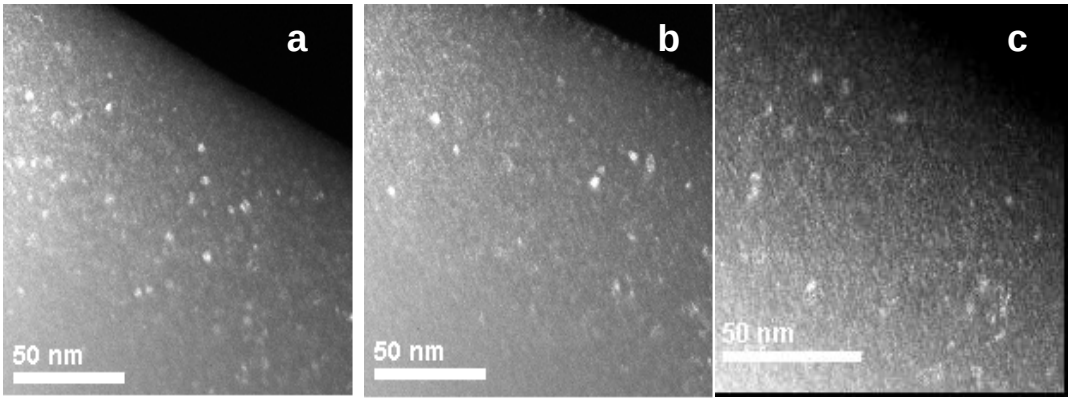

Figure 6.10 a)-c) DF images taken of the Er-doped Si NC region (sample B) with <022>, <111> and <200> reflections, respectively. The NCs appear crystalline, and are of the same density and size as revealed in the STEM-HAADF images (see figure 6.9).

Further investigation of the microstructure of this sample were carried out using the aberration correct STEM at Daresbury Laboratories, one of the world leading machines in the field, with <1 Å spatial resolution.

Figure 6.11a shows a low magnification HAADF image of the entire width of the silica film, revealing a ~110 nm wide band of Si-nano-clusters starting from ~75 nm below the surface of silica layer. This result is in agreement with the diffraction contrast observations of figure 6.10 and complements the idea of formation of crystalline nanostructures in a band deep inside the amorphous silica. No big clusters were observed as have been seen in the solely Er implanted sample (see later).

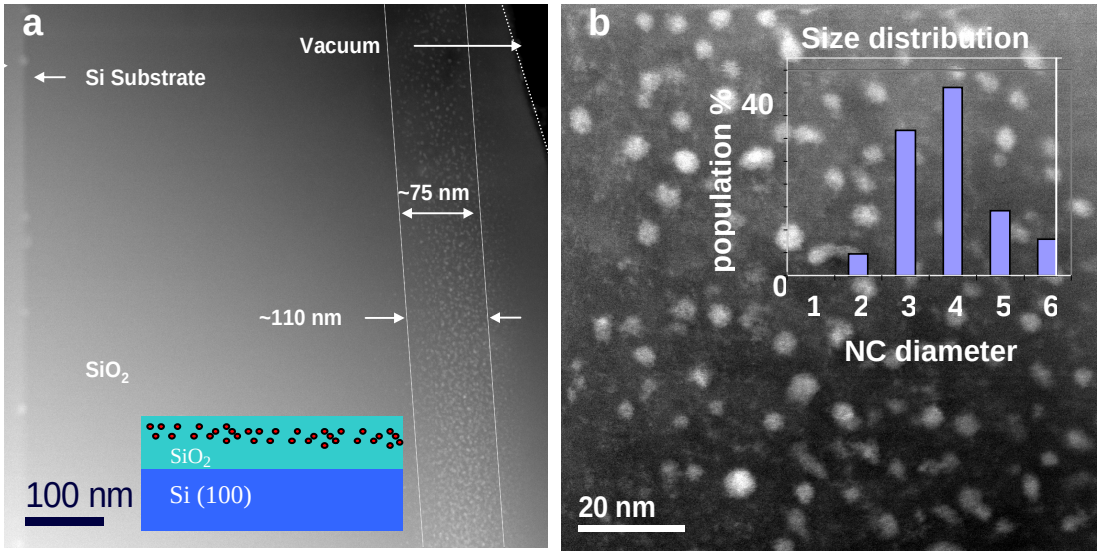

Figure 6.11 (a) low magnification HAADF image of the silica film showing the presence of a ~110 nm wide band of nano-clusters starting from ~75 nm below the surface of silica layer. (b) Higher magnification HAADF image illustrating a fairly homogenous distribution of NCs.

It should be re-emphasised that this proves the idea that excess Si acts as agglomeration centres for excess Er, which could be consumed under formation of metallic $ErSi_2$ or as an Er_2O_3 phase surrounding the Si-NCs. Based on the more intense 1.54 micron PL emission of this sample compared with Er-doped-only silica sample formation of metallic $ErSi_2$ is unlikely, and by considering the low solubility of Er in silicon the formation of Er_2O_3 surrounding the NCs is more likely. The higher magnification

HAADF image in figure 6.11b indicates a fairly homogenous size distribution of the NCs with about ~75% of their diameters lying in a band of 3-5 nm.

EELS was performed in SuperSTEM II in order to study the compositional properties of the nanoclusters shown in the high magnification HAADF image in figure 6.11b with near-atomic resolution.

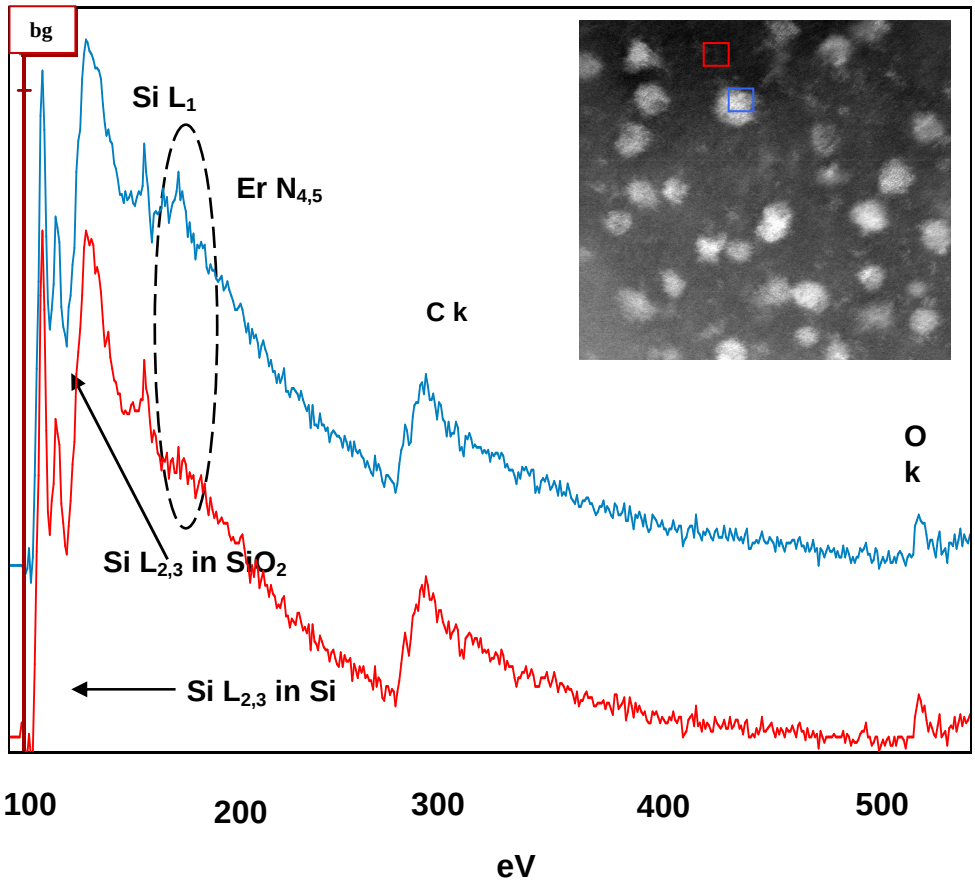

Figure 6.12 EELS spectra obtained with the STEM beam on (blue square and blue spectrum) and off (red square and red spectrum) a nano-cluster shown in the inset, high magnification HAADF image. An offset is applied for easier viewing of the spectra.

Figure 6.12 represents typical EEL spectra of (red) the oxide layer and (blue) a NC. In both the Si $L_{2,3}$, Er $N_{4,5}$ and O K-edges can be identified. The Er peak is clear (blue) in

the spectrum from the NC and missing (red) in the location off the NCs in the oxide layer. The C K-edge was used to calibrate the energy scale of the EEL spectra.

Figure 6.13 shows elemental maps extracted from an SI of the area of the HAADF image (figure 6.13a), of the Er-$N_{4,5}$ (~168-175 eV, figure 6.13b) and Si-$L_{2,3}$ (~99 eV, figure 6.13c) absorption edges, whose signal integral was obtained after power law background fitting close to the onset of the edge and subsequent background removal. There is a clear and strong correlation between the silicon and erbium distribution in the maps, which is further indication that erbium is more likely to accumulate within and/or around the Si-NCs. No substantial erbium clusters within the SiO_2 away from the Si-NCs exist, indicating that there is no sign of formation of separate Er_2O_3 clusters in between the Si-NCs.

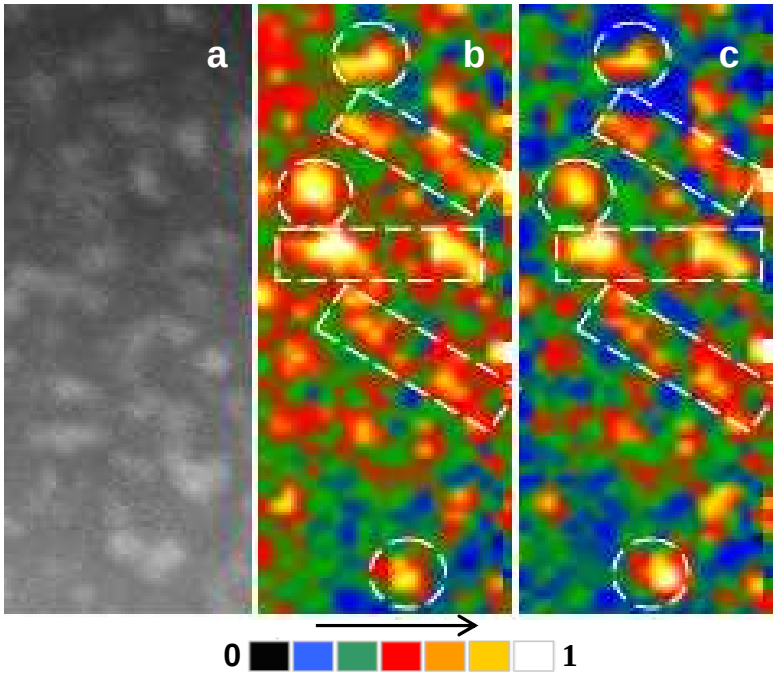

Figure 6.13 (a) HAADF image of the mapped area, (b) Si $L_{2,3}$ (98–101eV) and (c) Er $N_{4,5}$ (167–177eV) edge intensity maps. Dashed circles and rectangles indicate correlations in the features of the images and the contrast of the maps corresponds to a temperature scale.

To show any correlation between the distribution of excess Er and O in the structure to support the idea of formation of Er_2O_3 surrounding NCs, elemental mapping of O appears to be a possibility. However, as the area under investigation is dominated by SiO_2, direct mapping of O to reveal Er_2O_3 is not feasible.

Rare earth oxides exhibit a split O K-edge structure with an earlier onset compared to the onset and single peak characteristics of the O K-edge in SiO_2 [103]. Hence, fitting a Gaussian peak to the O K-edge helps to clarify the shape of the edge: fitting a single Gaussian envelope in regions with Er-oxide contribution would lead to a larger full width half maximum (FWHM) and lower energy than a Gaussian peak fitted to the single O K-edge peak of the SiO_2. Figure 6.14 illustrates such Gaussian fits to the O-K edge obtained from a NC (blue square in the HAADF image) and off the NC from the silica matrix (pink square in HAADF image). The fact that a larger FWHM and lower peak energy (blue trace) are indeed observed and spatially correlated with the Si-NCs indicates the presence of erbium-oxide in/near the Si-NCs. The smaller FWHM and higher peak energy (pink trace) belong to the pink square in an area from the silica matrix and away from the NCs.

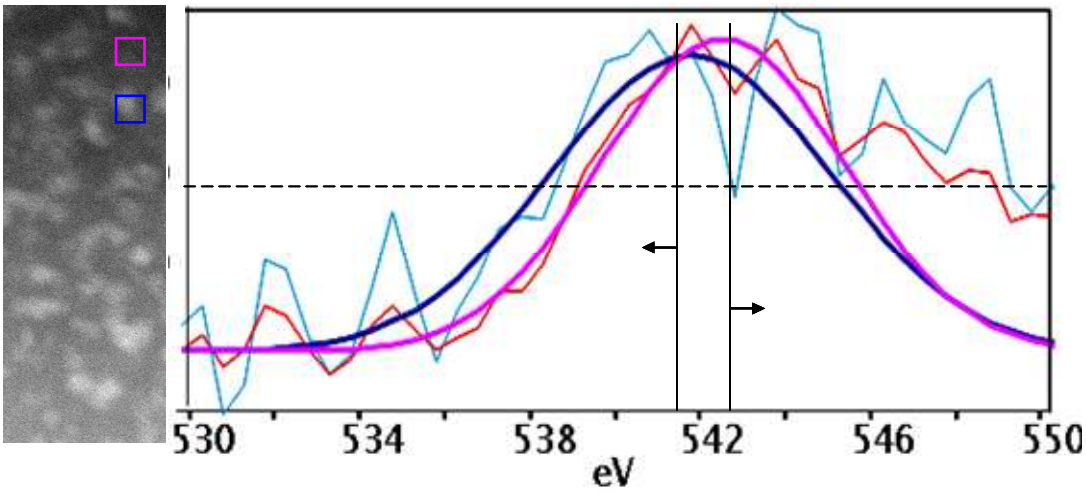

Figure 6.14 HAADF image (left) and Gaussian fits to the EEL O-K edges (blue on a NC and red from the matrix). The larger FWHM and lower energy of the fit (dark blue) to the NC spectrum and the smaller FWHM and higher energy of the fit (purple) to the matrix spectrum is obvious.

Figure 6.15 represent spatial distribution maps of the FWHM value (6.15b) and the energy value (6.15c) of a single Gaussian fit to the O K edge. The maps represent the same area as shown in HAADF image (6.15a) White/yellow colours signify a broader FWHM and higher energy and blue/black colours signify a narrower FWHM and lower energy Gaussian peak.

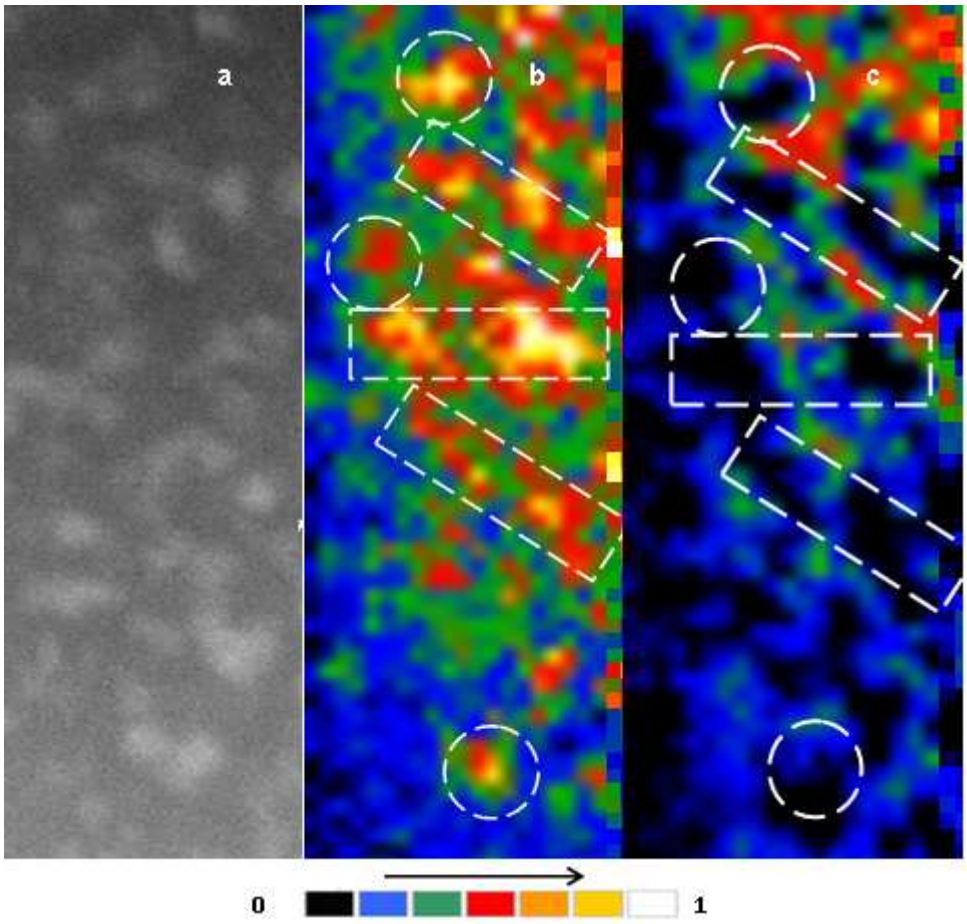

Figure 6.15 HAADF of the SI area (a) FWHM (b) and peak centre (c) of a single Gaussian fit to the O K edge. The white-framed boxes are drawn to guide the eye in correlating features across the three images

We find that the larger FWHM value of the O K edge Gaussian peak in figure 6.15b is spatially correlated with the Si-NCs in figure 6.15a (and also in figure 6.13b) which in turn are strongly correlated with the Er signal (figure 6.13c). These observations are indicative of the presence of Er–oxide, presumably in a shell, around the Si-NCs, in contrast to the narrower Gaussian, which appears elsewhere indicating the presence of pure SiO_2. Figure 6.15c reveals that the peak energy of the Gaussian fit is also lower in the locations of Er agglomeration supporting the presence of an Er–oxide complex.

6.5 Er doped silica (sample A)

In order to achieve a better understanding of the role of Si on the clustering and migration of Er, sample A with the same concentration of Er but with no excess Si was investigated via EFTEM, HAADF, HRTEM imaging and EELS SI. Diffraction contrast TEM, HRTEM, HAADF and EFTEM techniques were implemented using a Tecnai FEG microscope operating at 300 kV. EELS SIs of the previous core loss edges were acquired (in SuperSTEM II). SIs were analysed like all SIs before, using the DM software.

6.5.1 Structural study

Figure 6.16 depicts TEM-BF and HAADF images of two different areas in sample A. These images revealed that implanted Er ions agglomerate in Er rich clusters with diameters of 10–40 nm in a band near to and extending up to ~200 nm below the surface of the SiO_2. In order to understand the structure of the clusters HRTEM and EFTEM images were obtained. The HRTEM images showed that these big Er clusters have an amorphous structure as revealed by FFT.

Figure 6.17a shows an FT of one of big Er clusters shown in figure 6.16b. It is clear from the FT that these clusters are amorphous structures. Figure 6.17c depicts an EFTEM map of the Er $O_{2,3}$ EELS absorption edge (white signifies a high Er-signal), which reveals that the large clusters in the HAADF image are indeed Er-rich and most likely Er_2O_3. This distribution of Er is different from that of sample B and suggests that the excess Si atoms in B play an important role as agglomeration centres for Er ions, specifically after a single, high temperature annealing step. This is in contrast to the

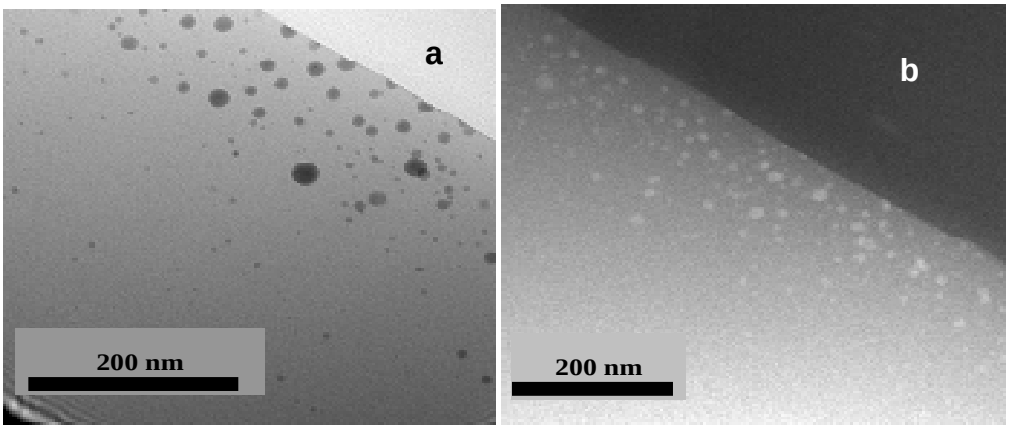

Figure 6.16 (a) Conventional BF and (b) HAADF image of sample A, showing formation of big clusters with tendency to move towards the silica surface . Images (a) and (b) are from different areas of the sample.

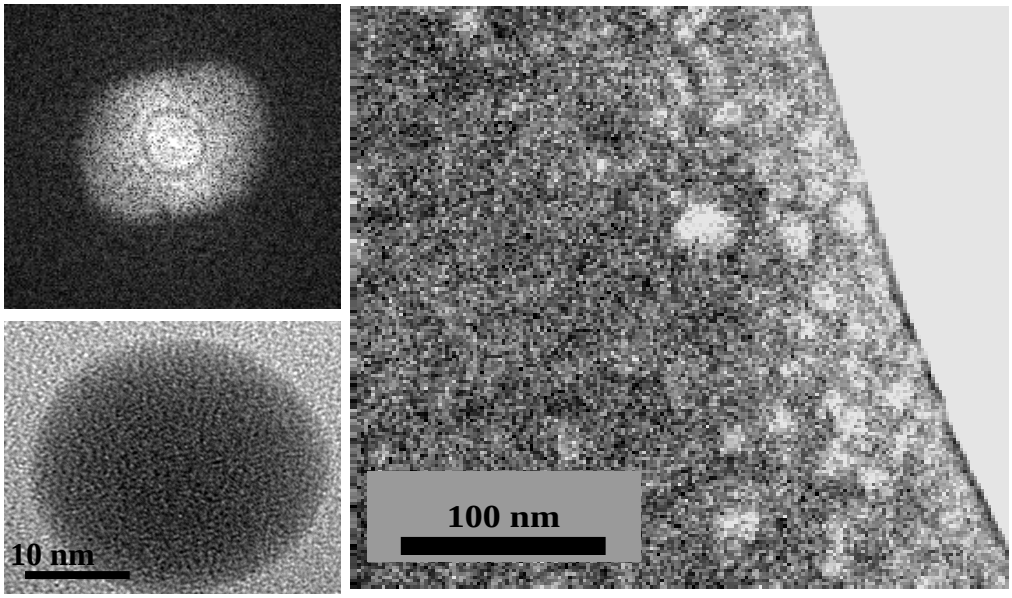

Figure 6.17 left) HRTEM image of a big cluster (bottom) as seen in figure 6.16(a) and its FT (top) indicating an amorphous structure; (right) EFTEM image using the Er $O_{2,3}$ edge intensity at 29 eV; Er-rich clusters are bright over the dark SiO_2 background.

findings of Pellegrino et al [104] in which the Si-NCs and Er were not found to be spatially correlated. This could be a result of the sample preparation, which the authors

employed: this involved a double annealing procedure, the first after Si implantation to obtain the Si-NCs and a second after Er implantation to activate the Er. This double annealing procedure is likely to alter the cluster formation mechanism compared with the single, high temperature annealing step after Si and Er co-implantation, as we have implemented.

6.5.2 EELS study

The big Er-rich oxide clusters in solely implanted Er material were further investigated. Core loss EELS studies were conducted in order to extract elemental maps of Er and O. Mapping of oxygen to distinguish the Er-oxide from the surrounding silica matrix is possible because the O-stoichiometry is different in both. EELS SIs of the core loss regime were acquired in SuperSTEM II.

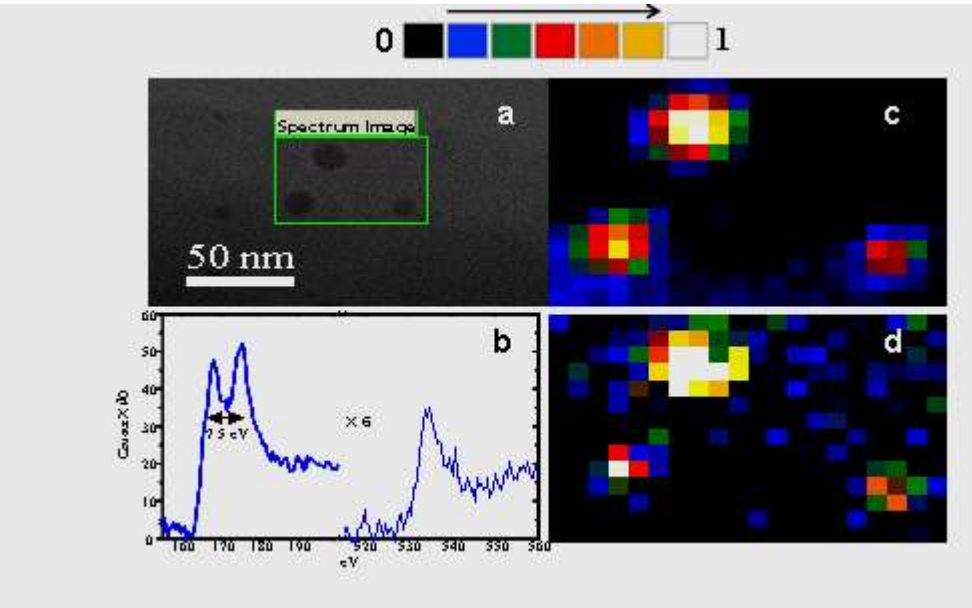

Figure 6.18(a) BF image of Er-clusters and (b) EELS spectra extracted from pixels of such clusters in the SI taken in the green area in (a). The double peak structure of Er $N_{4,5}$ located at ~168-176 eV and the O K edge at ~535 eV are clearly visible. (c) Er $N_{4,5}$ edge intensity map with energy window placed at 167-177 eV. (d) O K edge intensity at 532-538 eV. The spatial correlation between O and Er is clear from the provided maps.

Figure 6.18b shows EELS of the Er $N_{4,5}$ and O K core loss edges of sample A with the STEM beam on clusters shown in the green SI area in (a). A clear double peak structure of the Er $N_{4,5}$ located at ~168-176 eV and the O K edge at ~535 eV can be seen.. These edges were used to extract Er and O elemental maps. Figure 6.18c represents the Er $N_{4,5}$ edge intensity map in the energy window at 167-177 eV and (d) the O K edge intensity map by positioning the signal window at 532-538 eV, both obtained after background removal.

The Er and O distributions are strongly correlated. In the absence of excess Si large Er-rich clusters are formed. As PL-investigations indicate light emission from large Er-oxode clusters is unfavourable, because the probability of Er-Er back transfer is very high, hence Er-in more finely dispersed form, as occurs for example in the co-precipitation process with Si (sample B), is desirable.

5.6 Sequentially implanted and two-stage annealed Er and Si in silica (sample C)

Despite significant improvement in the intensity of PL emission at 1.54 μm of Er doped silica after doping with Si-NCs in sample B the intensity was still not sufficient for device applications. As nearly all excess Er was spatially correlated with NCs and presumably forms a shell around the NCs the probability of Er-Er interaction and quenching by up-conversion mechanism is still too high.

A way forward to avoid up-conversion or Er-Er quenching is to disperse less Er very close to the NCs. To achieve this, the Er and Si NCs doped silica samples were grown by a two stage implantation and annealing process as already explained in section 6.2.

Samples fashioned in this manner were likely to have the same concentration of NCs with similar size distribution to sample B but with lower concentration of Er surrounding the NCs. This will reduce up-conversion quenching of excited Er ions and also avoid the chance of formation of metallic silicide phases.

In order to investigate structural and compositional properties in sample C, which exhibited enhanced PL emission at 1.54 μm wavelength, like before, HRTEM, HAADF and EELS were performed. Figure 6.19 reveals formation of big Er clusters throughout the silica layer and a band of much smaller and less bright Si NCs starting from ~80 nm deep inside the SiO_2 layer and extending from there to ~120 nm below the surface. The distribution and size of the Si-NCs are comparable with those of sample B. NCs were formed around the implantation depth with no tendency to move towards the surface, in contrast to the Er-clusters. The Si-NCs, resulting from an excess silicon concentration of 8 at. %, could be resolved in both, HRTEM and HAADF. In contrast Pellegrino et al [104] were not able to resolve the NCs in samples prepared in a similar fashion with a similar Si excess concentration (5 at. %). We suggested that the excess silicon ions in sample B acts as agglomeration centres for Er ions.

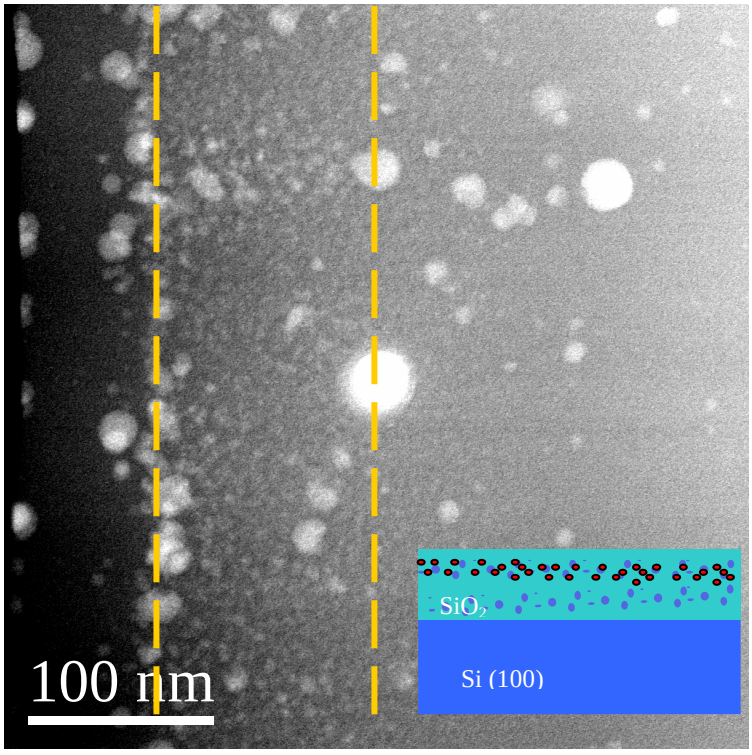

Figure 6.19 HAADF image of sample C displaying a band of Si NCs starting from ~75 nm below the surface of the silica with a width of ~120 nm (denoted by dashed orange lines). Big Er clusters are formed throughout the silica layer

Results of sample A (with no excess Si and big Er-clusters having formed throughout the matrix) support this idea. This is quite similar to results presented by other research groups [104]. They highlighted that Er clusters are not collocated with Si-NCs. It should be noted that their Er implantation was after the Si-NCs formation stage, which is further supportive evidence for the role of Si ions in the agglomeration of Er.

The BF image in figure 6.20 (left) shows lattice fringes within the NCs. The size of the NCs appears to be ~3 nm. The atomic resolution SuperSTEM HAADF image in 6.20(right)of the matrix between the NCs and away from the big Er cluster contains atomic size bright features. These features appear to be atomically dispersed Er within the matrix especially in the area where the NCs are located. EELS elemental mapping ascertained the HAADF findings of the area in the band of NCs. This is further supported by low magnification HAADF images of the NCs band, where the band area appears brighter than the area outside the band and close to the surface of the silica. This cannot be caused by thickness effects because it applies to the entire area of the HAADF image.

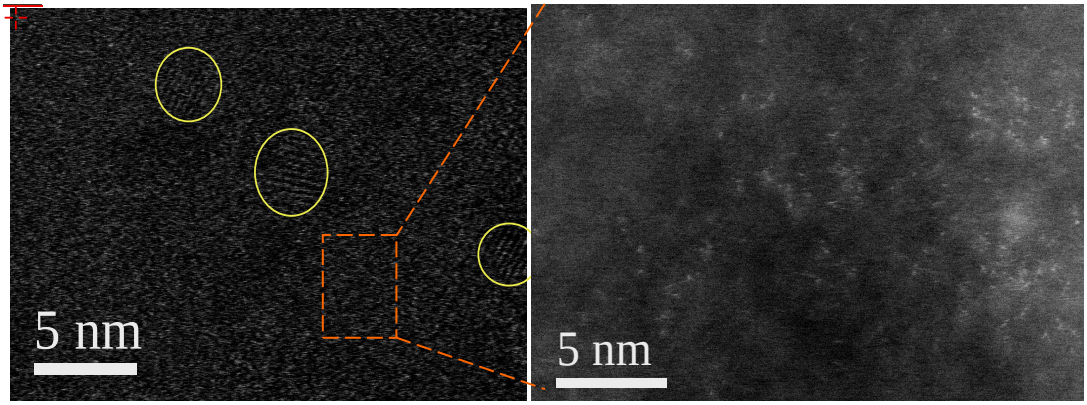

Figure 6.20 (left) HREM image of the matrix with clear view of ~3 nm Si NCs within the band; (right) high resolution HAADF image of an area in between Si NCs and away from big Er clusters showing a high density of atomic size bright features (probably atomically dispersed Er)

EELS core loss investigations were carried out to study compositional properties of sample C. Figure 6.21 depicts an EELS elemental map of the Er $N_{4,5}$ edge intensity in the area represented by the green box where an SI had been acquired. The brighter 'blobs' in the SuperSTEM HAADF image belong to Er rich clusters, several 10s of nm in size. The darker side of the HAADF image is the area close to the surface of the silica matrix; the brighter background on the right is where the band of NCs is situated in the matrix. The matrix here has more Er than the darker area outside the band. This supports the conclusions from the high resolution SuperSTEM HAADF image in figure 6.20, which showed atomically dispersed of Er in the matrix in between NCs. Carbon contamination build up hindered us from resolving the Si $L_{2,3}$ edge, however, Er intensity maps could be obtained and compared with HAADF images showing that there is significant spatial correlation between Er and the Si-NCs region although the Er is not directly co-located with the NCs.

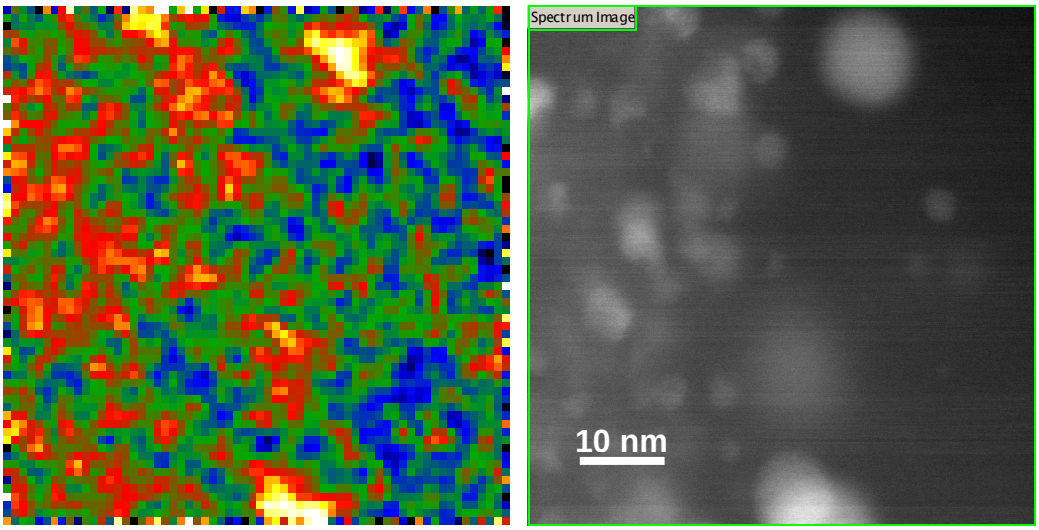

Figure 6.21 (right) HAADF image of the bright/ dark area interface (the starting point of Si NCs band), (left) Er $N_{4,5}$ edge intensity map of the same area with energy window placed at 167-177 eV

We ascribe the more intense PL emission at 1.54 μm compared to the single-stage annealed sample to atomic dispersion of Er in the matrix within the band of Si-NCs.

Despite the fact that there is no evidence of a core-shell structure of Si-NCs and Er_2O_3 in the two-stage implanted and annealed sample there are enough Er ions in the vicinity of the NCs to be sensitized. Also, as these Er ions are well separated and not agglomerated in a shell surrounding NCs the probability of Er-Er up-conversion interaction and quenching of sensitised Er by transferring energy to other excited Er ions is lower than in the single-stage annealed sample.

To gain a more detailed understanding of the chemistry of the matrix, the intensity of the core loss Er $N_{4,5}$, Si $L_{2,3}$, O K edge elementals maps of the all three sample was compared. For the Si $L_{2,3}$ maps the energy window from which the signal was extracted was placed at 107.5-110.5 eV. For the Er $N_{4,5}$ map, the Er signal window was placed at 165.0-177.5 eV and for the O-K intensity maps the energy window was placed at 532.0-542.0 eV. For all elemental maps and for all three samples a similar power law background model at similar positions of the spectrum was fitted close to the onset of the edge

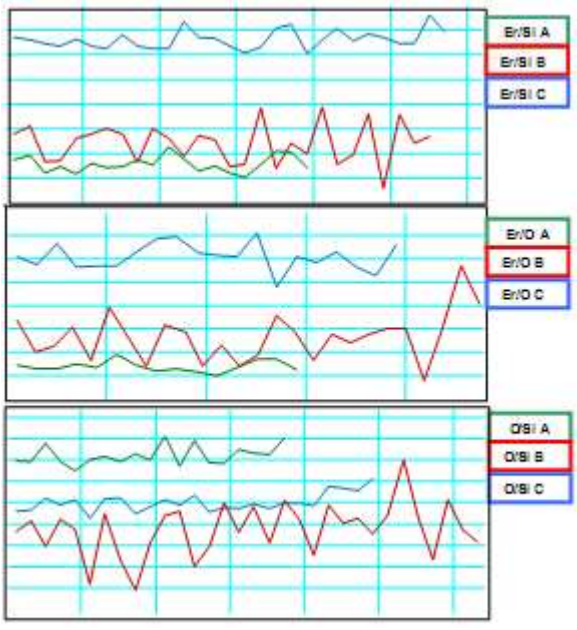

Figure 6.22 Intensity ratio profiles of (a) Er/Si, (b) Er/O and (c) O/Si ratio maps of sample A, B and C extracted from regions in between NCs and Er-clusters

Due to different experimental conditions (thickness, change in operational conditions in separate experiments) it is near-impossible to obtain absolute values, however relative values of O, Er and Si can be obtained by constructing Er/Si, Er/O and O/Si ratio maps. The ratios of the elements in the matrix in all three samples were then obtained by extracting intensity ratio line profiles in regions away from Er clusters and Si-NCs. Figure 6.22 represents Er/Si, Er/O and O/Si ratio profiles of all three samples. The x-axis in these plots represents a spatial coordinate, a distance.

As can bee seen from these line profiles the Er/Si ratio in the matrix of the sample with sequential Er and Si implantation and two-stage annealing is higher than in the other two samples. This shows that Er is dispersed in the matrix of sample C (rather then in NCs or clusters). The Er/O ratio in sample A is lower than in the other two samples, which show almost the same value. This means that most of the Er in sample A is in clusters. Figure 6.22 further shows a higher O/Si ratio profile for sample A compared to that of sample C and B. This is indication of a more stoichiometric oxide in A then in B and C, which is reasonable, since excess Si and post-oxidation in samples B and C are likely to lead to a sub-stoichiometric oxide. The O/Si ratio in sample C is slightly higher than in sample B. Again this is understandable as in sample B much O is ‘swept up’ into the Er-oxide shell around the NCs.

By considering a higher concentration of atomically dispersed Er in the matrix for sample C compared to sample B and A together with evidence from EELS analysis that there is no direct spatial correlation between Er and Si in this sample, the more intense PL emission at 1.54 μm for this sample compared to the other two can be understood as follows: in this sample Si-NCs (i) can sensitize Er ions and (ii) can do this most efficiently as these ions are dispersed in the matrix rather than participating in shell structures around the NCs, and hence the probability of Er-Er interaction and up-conversion phenomenon is low.

6.7 Conclusion

HREM, HAADF and EELS techniques were carried out in a dedicated aberration corrected STEM (SuperSTEM II) to establish structure and composition of solely Er

and Er and Si doped silica samples, grown with different growth and annealing conditions, for device application. We have shown that co-implanting relatively high concentrations of Er and Si in SiO_2 after employing a single, high temperature anneal led to several hundred times more intense PL emission at 1.54 μm then in solely Er-doped silica. Clear Er $N_{4,5}$ EEL edges were observed in the area where Si-NCs were formed. High spatial correlation between Si-NCs, Er, and O in the co-implanted, single-stage annealed sample has been proven for the first time to the best of our knowledge. However, the PL intensity was lower than anticipated. We ascribed this to quenching of sensitized Er ions due to excitation of further Er ions and a resulting reduction in the PL emission. To improve this, two stage implantation and annealing was applied. The resulting new material showed higher PL intensity. We explored this sample using the same techniques and, surprisingly, our results showed no spatial correlation between Er and Si-NCs. Chemistry and structure of the matrices in all samples were investigated and showed a higher atomically dispersed Er fraction in the matrix of sample C. We conclude from this that lower up-conversion Er-Er quenching occurs as a result of the larger distance between Er ions.

7

Valence band electron energy loss spectroscopy

7.1 Introduction

The lower light emission from co-implanted then from sequentially implanted samples needs more investigation regarding the possibility of formation of metallic Er-silicide; this might be feasible as all the Er and Si are co-located.

It is not possible to determine this directly from HREM images because the NCs are too small (2 nm) and embedded in an amorphous matrix, which obscures the lattice information. Hence Fourier transforms of HREM images are too noisy to reveal differences to those of pure Si.

From core loss EELS it appears all Er is co-located with Si-NCs and no Er is detectable in the SiO_2 matrix. The O-edge signature changes to that of a rare earth oxide around the Si-NCs, suggesting a Si-NC-Er_2O_3-core shell configuration. In sequentially implanted samples, on the other hand, it seems Er forms few large Er_2O_3 clusters with the rest of the Er finely dispersed (presumably as oxide) within the matrix in between the Si-NCs, but not co-located with them. This does not give a direct explanation for the higher efficiency of the second sample; on the contrary, it would appear that an oxide shell around the Si-NCs would facilitate the Er-Si interaction. If, however, Er-silicide phases formed within the NCs, these would pose entirely different optical characteristics.

7.2 Low Loss EELS

Low loss EELS can be employed for localised electronic structure investigations: The smallest loss signals (in the range of meV) arise due to phonon production. Losses of

1eV up to 10 eV in semiconductors and insulators signify inter- and intra band transitions, e.g., from the valence to the conduction band. Higher energy losses, as previously noted, arise from collective excitations, e.g. production of plasmons. With our present experimental set-up we can only access the energy loss region from ~5 eV upwards. The ZLP is part of the low loss spectra; because it has orders of magnitude higher intensity then the core-losses it leads to saturation of the detector. This can be counteracted by use of high energy dispersions, which has the additional benefit of separating low loss signals from the ZLP. When signals are sufficiently remote, i.e., made to occur on the lower tail end of the ZLP, the latter can be removed by appropriate fitting routines and subtraction from the low loss spectra. However, this is often not sufficient for reliable signal extraction, and deconvolution algorithms, like the Richardson-Lucy (RL) algorithm have been applied (spectra which have been obtained after RL deconvolution will be noted in the following results).

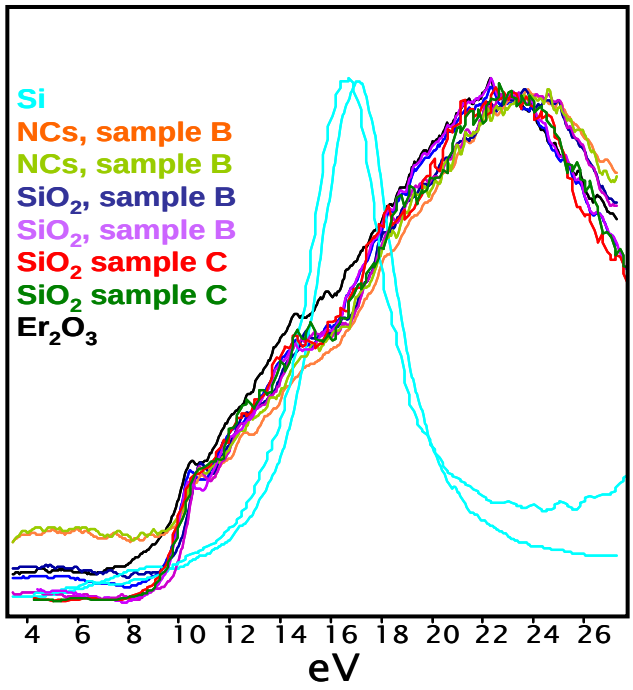

Figure 7.1 low loss spectra of Er:Si-NC samples A and B, of Er_2O_3, of SiO_2 and of Si

Figure 7.1 shows low loss spectra of oxide and NC regions in samples A, B and C, as well as of Er_2O_3 and SiO_2 and of Si. Apart from the Si-spectra (turquoise), the spectra look all very similar. This is partly due to the predominant contribution of the SiO_2

matrix, even if spectra were obtained with the probe focussed on individual NCs (e.g., orange and light green). The only significant difference is that the NC spectra exhibit higher losses in the low loss region <10 eV. These arise from Er5d6s-> O3s transitions (Er4f->5d contributions are also possibly contributing) [105]. There is furthermore an earlier rise of the intensity at ~ 8 eV in the Er_2O_3 spectrum (black) obtained from a large Er-cluster in sample A. Apart from the Si (turquoise) and the pure SiO_2 spectra (blue and purple), obtained in regions with no NCs, all spectra consist of superpositions of loss characteristics of different materials, i.e., SiO_2 and Si-NCs.

7.3 KK analysis and dielectric function

One way to proceed in order to gain more information about the nature of the NCs in sample B is to extract the dielectric functions from low EELS data via KK analysis, and compare these to functions of Er-oxide and Er-silicide in the literature. We have attempted this, using the KKA routine in DM, for the co-implanted sample.

Figure 7.2c shows the real (solid lines) and imaginary (dashed lines) parts, ε_1 ε_2, of the dielectric functions extracted from spectra of NCs, assigned orange lines in figure 7.2c, from the region with the orange cross in the HAADF image in figure 7.2a. Curves extracted from spectra of oxide regions without NCs (blue cross in figure 7.2a), are assigned blue lines in figure 7.2c. ε of a large Er_2O_3 cluster in sample A is represented by black lines and of pure Si by the turquoise lines. Figure 7.2b shows literature results [106] for Er_2O_3 and $ErSi_2$. The blue shaded area in figure 7.2c is the energy regime accessible to us 7.2(b). The corresponding region is shaded in blue in the reference spectra in 7.2b. Comparing Er_2O_3 data obtained from large Er-clusters (black curves in 7.2c, the corresponding image is not shown here) with reference data [106], there is a similarity in trend but not in value in the imaginary part, ε_2. This is not too surprising, as the KKA routine requires determination of the single scattering distribution, for which deconvolution routines are used. These in turn rely on extraction of the ZLP (intensity and shape), which carries large uncertainties in the tail region of the ZLP due to limitations in energy resolution. Hence it can be expected that the values of the

extracted dielectric function have large errors. The real part fares better in terms of value, but less well in the overall shape.

Spectra obtained from SIs of individual NCs (figure 7.2c, orange lines) show greater similarity with Er_2O_3 then with $ErSi_2$ for their real parts, but the opposite applies for the imaginary part. However, the NC dielectric function bear greatest similarity with that of SiO_2 (figure 7.2c, blue line); hence it becomes clear that the matrix above and below the NC, traversed by the probe, has a dominant effect. One could furthermore say that the dielectric function of both, the NCs and the Si-oxide resembles in trend that of Er-oxide.

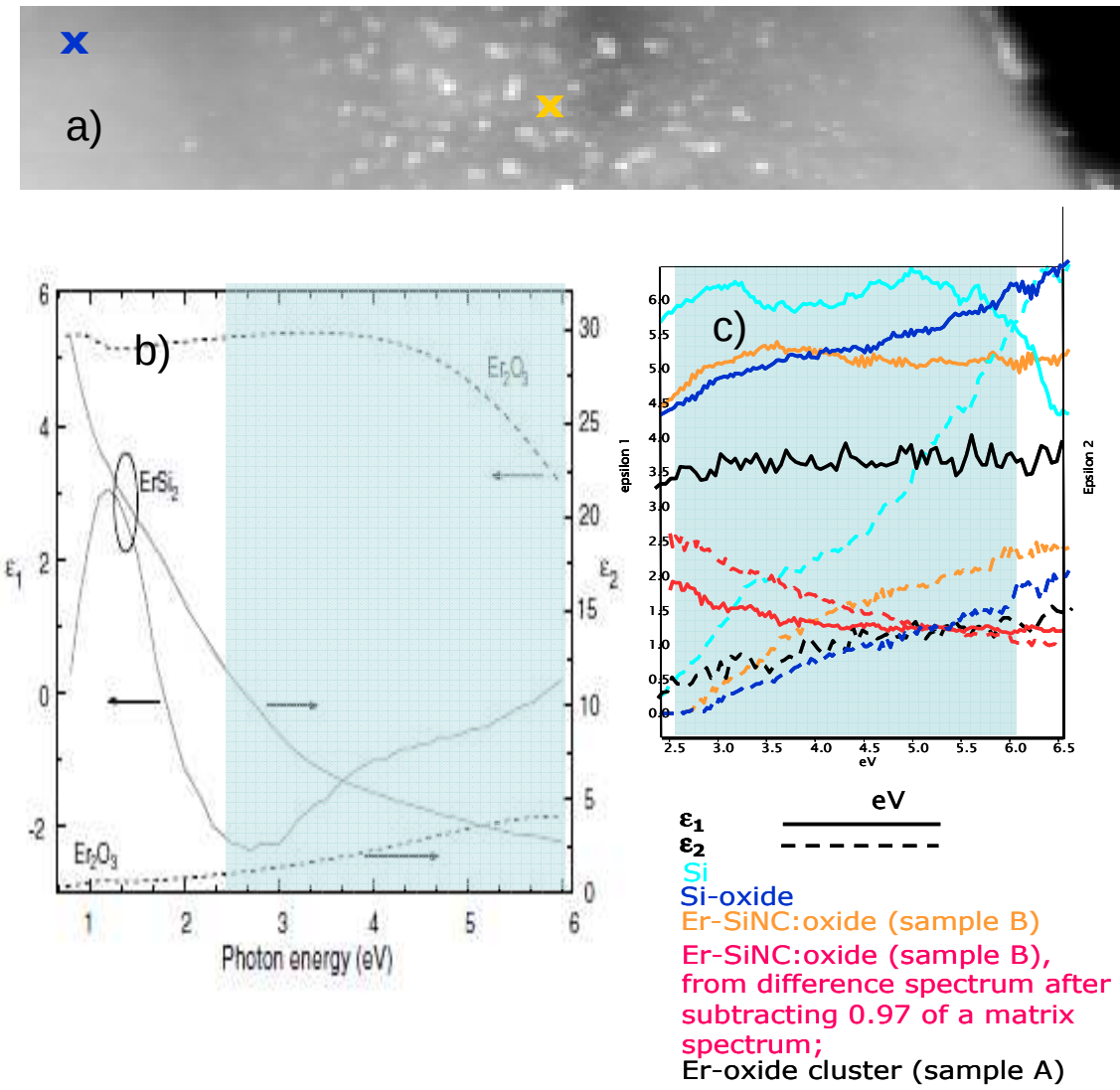

Figure 7.2 (a) HAADF image of SI area in sample B. (b) Experimental real and imaginary part of the dielectric functions of Er_2O_3 and $ErSi_2$ [106] and (c) those of different regions in samples B

In order to enhance the contribution of the Er:Si NCs in sample B it is feasible to obtain difference spectra by subtracting a portion of a SiO_2 low loss spectrum from a 'composite' spectrum obtained with the beam positioned on a NC. This portion was estimated as 97% of a pure Si-oxide spectrum and was derived from the NC/oxide volume ratio that the e-beam encounters, when placed on a NC, which in turn can be estimated from the size of the NCs in HAADF images and the specimen thickness (determined by EELS). KKA performed on a difference spectrum gives the dielectric function shown in the dark red curve in figure 7.2c. Here the trend and shape of both, ε_1 and ε_2 are very different from those obtained without subtraction of a matrix contribution, and one could argue that now the imaginary part ε_2 resembles that of $ErSi_2$, however, the real part ε_1 looses resemblance to both, $ErSi_2$ and Er_2O_3. Thus the issue of presence of $ErSi_2$ remains unresolved using this analysis, and neither is a significant presence of Er_2O_3 confirmed.

Overall, the KKA analysis and dielectric function comparison failed to give consistent results. This could be due to two major reasons; i) the composite nature of the material made it impossible to obtain the unique shape of the functions of the constituent materials (i.e., Er_2O_3, $ErSi_2$), even after subtraction of the matrix contribution; ii) a further complication arises due to insufficient data quality and instabilities in the KKA program in the region of interest arising from the small signal and noisy data.

7.4 Plasmons and interband transitions in difference spectra

Investigating the low loss intensity directly, especially in the plasmon region, seems a more promising prospective. Figure 7.3 shows difference spectra of the energy region 5-30 eV for various scenarios with vertical lines assigning low loss events to their respective energies.

Curves are numbered (*i*) to (*x*) and discussed in the following.

Curve *i* (purple) is the difference of an Er:Si-NC- spectrum in the co-implanted sample B and an Er_2O_3-spectrum. It appears the Er-oxide contribution has completely disappeared, and the SiO_2 matrix contribution is dominant (as discussed for the previous figure) with only the SiO_2 surface and bulk plasmon peaks at ~15 and ~23 eV [107]

present (see also curves in figure 7.1). If, however, an oxide spectrum proportion is subtracted from Er:Si-NC spectra (*iv-vi*, blue curves), the Si plasmon at ~16.7 eV occurs, giving witness of the existence of crystalline Si. (A Si-spectrum obtained from the Si-substrate is shown in the turquoise curve *vii* for comparison). There is also a notable shoulder at ~9 eV (Er5d6s->O3s [105] in curve *iv-vi*, confirming the existence of Er-oxide in some form. This peak can also be seen in the Er_2O_3 spectrum (*iii*, black) obtained by subtracting a SiO_2 contribution from a spectrum of a large Er-oxide cluster in the SiO_2 matrix. However, it should be noted that the Er_2O_3 plasmon at ~15 eV is missing in difference spectra (*iv-vi*). Curves *viii* and *ix* (orange) are difference spectra of places in the Si-oxide between Si-NCs in the co-implanted sample B and places in the pure oxide. A reminiscent Si-plasmon as well as the Er-oxide transition at ~9 eV can be seen; the occurrence of both is not surprising considering the proximity of Er:Si-NC and the delocalisation of low loss events. Curve *x* is the difference between two oxide spectra and is comparatively featureless.

An additional curve (*ii*, red) shows the difference between a spectrum of the oxide region containing Si-NCs and an oxide region without Si-NCs in the sequentially Si and Er implanted sample C. Here Er was not found to be co-located with Si, but dispersed in the Si-oxide matrix between the Si-NCs. The Er-oxide transition at ~9eV can be seen as well as the SiO_2–plasmons at ~15 and ~23eV, as can be expected.

The absence of an Er-oxide plasmon is not surprising in the last case, as Er-oxide formation and distribution (see HAADF images in previous chapter) presumably takes place on a molecular level (hence no collective phenomena are expected). In cases *iv-vi*, however, if a core shell structure had formed, one would expect a Si- as well as an Er-oxide-plasmon, which might even give rise to a new interface plasmon.

The lack of such plasmons indicates either a highly defective ‘interface’ between the Si-NC core and the Er-oxide shell, or an unconnected rather ‘dendritic’ Er-oxide network surrounding the Si-NCs, or both. The lower light efficiency of this sample combined with the lack of a plasmon point towards the existence of high numbers of defects at the Si-NC surface/interface with the Er-oxide, which cause significant non-radiative recombination.

Furthermore, from the plasmon structure there is no evidence of Er-silicide formation: a silicide should have introduced a plasmon at 18-20 eV[107].

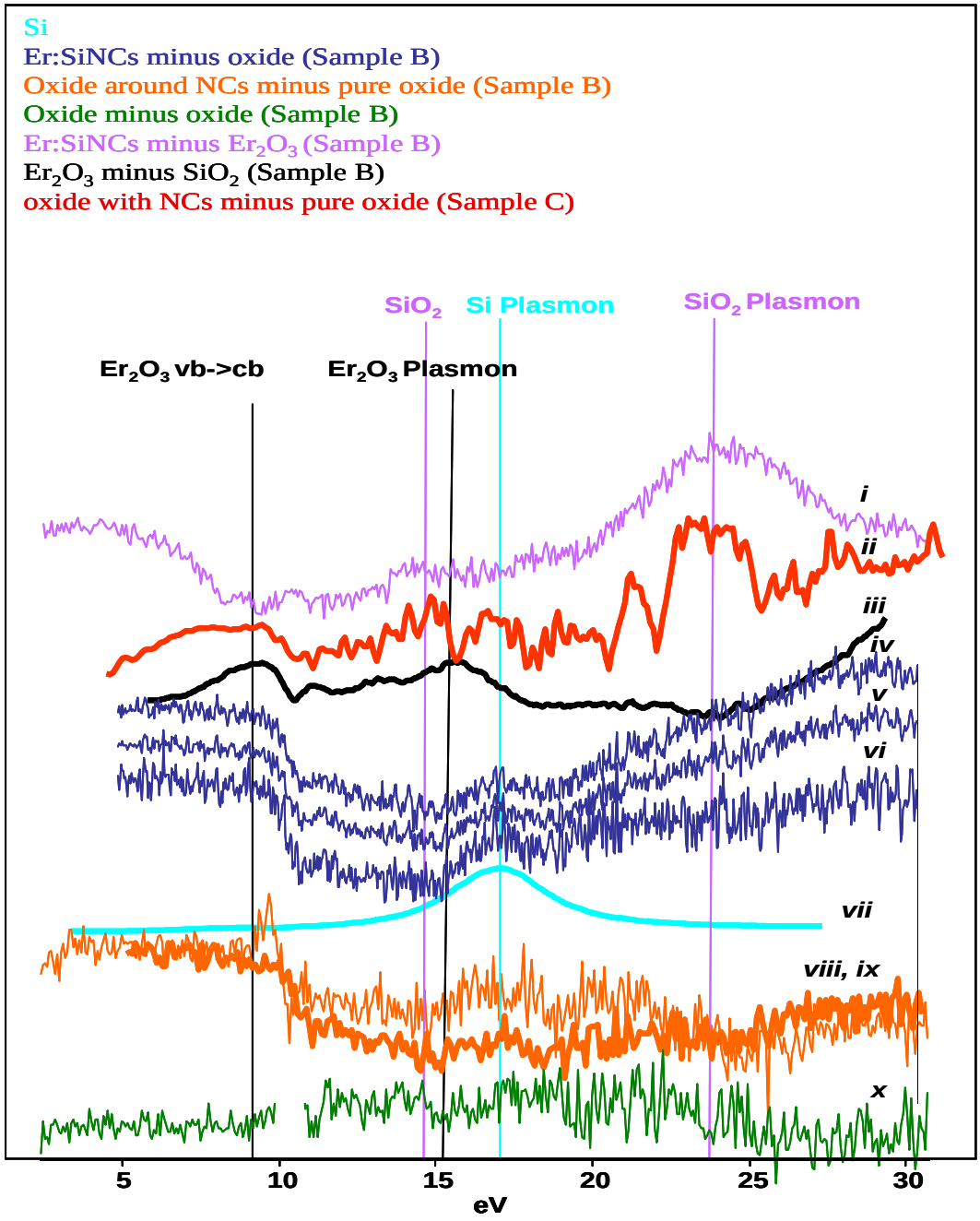

Figure 7.3 Difference spectra of the energy region 5-30 eV for various scenarios with low loss events assigned to their respective energies. Numbered curves are discussed in the text.

7.5 Conclusion

Valence band EELS was conducted to further investigate the composition- and structural relationship of Er and Si-NCs, especially regarding the possibility of Er-silicide phase formation in the co-implanted sample B, where strict co-location of Er and NCs was observed. Low loss spectra of various locations in the SiO_2 layer, apart from showing characteristic Er5d6s-> O3s transitions when taken of NCs in sample B, look all similar, i.e., are dominated by the surface and bulk plasmon of the Si-oxide matrix. Also dielectric functions, extracted via KKA from low loss spectra gave inconclusive results. It became evident that Si-oxide contributions had to be removed from the spectra prior to KKA analysis. This was done by obtaining difference spectra, i.e., by subtracting a portion of a Si-oxide spectrum from the NC spectra, and resulted in drastic changes in the dielectric function, but still did not give consistent results. Direct investigation of difference spectra, however, revealed interesting characteristics of the low loss function, especially the absence of an Er-oxide plasmon in the NCs in sample B. Previous core loss EELS results pointed to the formation of an Er-oxide shell around the Si-NCs in the co-implanted sample B. If this was the case, an Er-oxide plasmon (which was clearly observed in Er_2O_3 clusters in sample A) would also be expected in the NCs in sample B. The lack of the latter in sample B indicates a highly defective 'interface' between the Si-NC core and the Er-oxide shell, and was thought to be the reason for the inferior emission efficiency of sample B, due to potentially high numbers of non-radiative recombination centres. There is no evidence for Er-silicide phases.

8

Overall conclusion and future work

8.1 Conclusion of work from this thesis

Ge-NCs embedded in Al_2O_3 films were successfully produced by RF-magnetron sputtering. Changing the annealing temperature and gas flow pressure led to growth of Ge-NC with different sizes (on average ~5 and ~8 nm). Raman and XRD results indicate strain in the larger NCs. Furthermore, the shifts, if genuine, are concomitant with strains < 0.5 %, which is below the accuracy of HRTEM-based lattice constant determination. HRTEM suggests unstrained structures for the small NCs, because plastic relaxation and extensive nano-twinning have taken place. This explains the red shift in the Raman peak position of the sample and is a sign of relaxed NCs. HRTEM images show the polycrystalline structure of the matrix.

Investigation via different methods were carried out on two kinds of samples, grown by Molecular Beam Epitaxy, of 1.77ML InAs layers (i.e. just at the critical thickness) separated by ~25 nm GaAs spacers with and without growth interrupt (GI). It was found that applying a GI of 60s after deposition of InAs leads to formation of self-assembled QDs in each wetting layer whereas continuous growth shows no footprint of QD formation except formation of smaller dots in the surface layer.

In order to see atomic-scale distribution of In and help explain the dynamics of the dot formation in the 1.77 ML sample after GI, HAADF images were acquired and EELS investigation performed to reveal the elemental distribution within the dots.

In the case of the sample with GI intensity profile investigation on HAADF images showed the dots height and lateral extent was 2.8-3.2 nm and 13-16 nm respectively.

In-intensity maps of the QDs were provided after KK analysis and they revealed the inhomogeneous distribution of In within the dot and showed that the wetting layer near the dot's edge was ‘pinched off’ because of migration of In adatoms from the wetting layer to the dots.

In the case of the sample without GI atomic steps in bottom and diffused top interfaces of wetting layer and spacer were observed. The immediate growth of GaAs after InAs inhibits diffusion and segregation of In-adatoms, and In-Ga intermixing leads to reduction of the strain in the wetting layer. In support of the above conclusions the atomic resolution HAADF lattice images of InAs layers with a nominal thickness of 1.77 ML in superlattices without apparent dot formation suggest considerable roughness on the scale of 1-2 monolayers and step separations of ~10 nm.

GPA clearly shows lattice distortion in InAs QD layer especially where the QD has formed with a maximum In concentration of 65% inside the QD and at close to the top of QD. The compositional findings of the GPA for the QD layer support KK analysis and EELS elemental maps of the In distribution in the QD layer. The well layer in vicinity of QD showed to be an $In_xGa_{1-x}As$ ternary alloy with maximum In concentration of 28%.

Our suggestion for the QD formation mechanism is the folllowing: In adatoms segregate to step edges which acts as sinks and increase the strain in these areas. Strain relief occurs by diffusion of Ga adatoms from the substrate. This leads to erosion at the edges of islands and evolution of dots of an InGaAs alloy with inhomogeneous composition.

HREM, HAADF and EELS techniques were executed in a dedicated aberration corrected STEM (superSTEM II) to investigate structure and composition of solely Er as well as of Er and Si NCs doped silica samples for device application, grown with different growth and annealing conditions.

We have shown that co-implanting relatively high concentrations of Er and Si in a SiO_2 matrix after employing a single, high temperature anneal leads to enhancement in the optical properties of the material presenting several hundred times more intense PL emission at 1.54 μm compared to solely Er implanted silica structures. Clear characteristic double peaked Er $N_{4,5}$ EEL edges were observed in the area where Si-NCs were formed. High spatial correlation between Si-NCs, Er, and O in the single stage Er and Si co-implanted sample have been demonstrated for the first time to the best of our knowledge, using the state of art SuperSTEM machine.

The PL intensity was less then anticipated from the strong spatial correlation of Si-NCs and Er. We ascribed this to quenching of the sensitized Er ions by excitation of other Er ions, resulting in a reduction of the PL emission.

To examine the possibility enhancing the PL intensity a two-stage implantation and annealing process was carried out. The new material showed higher PL intensity. We explored this sample with the same techniques and surprisingly our results showed no spatial correlation between Er and Si-NCs. Chemistry and structure of the matrices in all samples were investigated and showed higher atomically dispersed Er for the sample grown by the two-stage implanttion and annealing process. We ascribed this to the relative lower up-conversion and Er-Er quenching, in which is energy is transferred from one sensitised and excited Er ion to other one as a result of the larger distance between Er ions surrounding the NC.

The issue concerning the lower light emission from co-implanted then from sequentially implanted samples needed more investigation. There is a possibility of formation of metallic Er-silicide in the presence of excess Er and Si in the matrix. Low loss spectra of various locations in the SiO_2 layer, apart from showing characteristic Er5d6s-> O3s transitions when taken of NCs in sample B, are dominated by the plasmon characteristics of the Si-oxide matrix and this is also reflected in the dielectric function. Removing Si-oxide contributions by subtracting a portion of a Si-oxide spectrum from the NC spectra resulted in drastic changes in the dielectric function but did not give

conclusive results. Direct investigation of difference spectra reveal no Er-silicide phase and furthermore show absence of an Er-oxide plasmon in the NCs in sample B. If formation of an Er-oxide shell around the Si-NCs, as suggested by the core loss EELS results had occurred, then an Er-oxide plasmon (which was clearly observed in Er_2O_3 clusters in sample A) would also be expected in the NCs in sample B. The lack of the latter indicates a highly defective 'interface' between the Si-NC core and the Er-oxide shell with a potentially high number of non-radiative recombination centres and this was thought to be the reason for the inferior emission efficiency of sample B.

8.2 Future work

We have found a polycrystalline structure for the alumina matrix. This issue and implications for GeNC formation and, more generally, for the memory properties, needs to be further addressed with HREM, localized nano-electron diffraction and EELS mapping of Ge.

With regards to the InAs/GaAs quantum dot structures more experiments on samples prepared with different (especially shorter) GI time and monolayer fractions need to be carried out to investigate QD formation and any changes in their population and composition. GPA gave promising results in the compositional understanding of QDs. More GPA measurements should be carried out on better quality HRTEM images, especially for sample without growth interrupt.

For the co-implanted Er- and Si-NC-doped silica sample we have reached the conclusion based on core loss studies that Er forms a shell around the NCs. This was not ascertained by low loss investigations, which suggested a highly defective Er-oxide structure. Further low loss measurement are needed by acquiring low noise and good quality SIs to reach stronger conclusions about the structure of the Er-oxide shell and to confidently exclude existence of silicide phases in the NCs. With higher energy dispersion and utilisation of deconvolution algorithms, losses <5 eV might be accessed, which can show directly the existence of bandgap states related to defects in the oxide. These could then be more strongly related to optical measurements.

Sequentially Er and Si implanted and annealed samples give stronger PL compared to co-implanted sample with similar excess Si and Er concentrations. We attributed this to composition and microstructure of the matrix where there is a higher atomic- or molecular-dispersed Er fraction in the matrix. We propose that an increase in the Si-NCs population in this sample could lead to even greater improvement and more intense PL. Samples with higher excess Si should be grown to support our idea of the role of the microstructure of the matrix in the Er related emission.

9

References

[1] J. Ng, M. Missous, Microelectronics Journal **37** (2006) 1446.

[2] P. Becker, A. Olsson, J. Simpson, Erbium-Doped Fiber Amplifiers, Elsevier Academic Press, (1999) 1.

[3] P. G. Kik, M. L. Brongersma, A. Polman, Appl. Phys. Lett. **76** (2000) 2325.

[4] L. Pavesi, D. J. L. (Eds.), Silicon Photonics, Springer-Verlag Berlin Heidelberg, Berlin, (2004).

[5] M. Wojdak, M. Klik, M. Forcales, O. B. Gusev, T. Gregorkiewicz, D. Pacifici, G. Franzò, F. Priolo, F. Iacona, Phys. Rev. B **69** (2004) 233315.

[6] P. G. Kik, A. Polman, Materials Science and Engineering B 81 (2001) 3.

[7] B. Park, S. Choi, H.-R. Lee, K. Cho, S. Kim, Solid State Communications **143** (2007) 550.

[8] P. G. Caldelas, Production and Characterisation of Composites Materials based on Ge doped dielectric layer, MSc. thesis, The University of Minho, (2009)

[9] A. Kanjilal, J. L. Hansen, P. Gaiduk, A. N. Larsen, N. Cherkashin, A. Claverie, P. Normand, E. Kapelanakis, D. Skarlatos, D. Tsoukalas, Appl. Phys. Lett. **82** (2003) 1212.

[10] P. Caldelas, A. G. Rolo, A. Chahboun, S. Foss, S. Levichev, T. G. Finstad, M. J. M. Gomes, O. Conde, Journal of Nanoscience and Nanotechnology **8** (2008) 572.

[11] S. Yerci, M. Kulakci, U. Serincan, R. Turan, M. Shandalov, Y. Golan, Journal of Nanoscience and Nanotechnology **8** (2008) 759.

[12] M. J. H⌿tch, E. Snoeck, R. Kilaas, Ultramicroscopy **74** (1998) 131.

[13] R.R.Egerton, Electron Energy-Loss Spectroscopy in the Electron Microscope, 2nd Edn. Plenum Publishing Corporation, New York (1996).

[14] C. Kittel, Introduction to Solid State Physics, John Wiley and Sons (2005).

[15] J. A. Hunt, D. B. Williams, Ultramicroscopy **38** (1991) 47.

[16] C. Jeanguillaume, C. Colliex, Ultramicroscopy **28** (1989) 252.

[17] M. Tencé, M. Quartuccio, C. Colliex, Ultramicroscopy **58** (1995) 42.

[18] J. Singh, Electronic and Optoelectronic Properties of Semiconductor Structures, Cambridge University Press, Cambridge (2003).

[19] S. R. S. B.D.Cullity, Elements of X-Ray Diffraction, Prentice-Hall, Inc., New Jersey (2001).

[20] T. Ungár, Materials Science and Engineering A **309-310** (2001) 14.

[21] R. J. M. R. Alani, and P. R. Swann, Mat. Res. Soc. Symp. Proc. 480 (1997) 263.

[22] S. M. Sze, Semiconductor devices, Physics and Technology, John Wiley and Sons, Inc (1985).

[23] M. Henini, Nanoscale Res Lett (2006) 32–45.

[24] F. Adler, M. Geiger, A. Bauknecht, F. Scholz, H. Schweizer, M. H. Pilkuhn, B. Ohnesorge, A. Forchel, J. Appl. Phys. **80** (1996) 4019.

[25] A. Z. H.T. Dobbs, D.D. Vvedensky and M. Tringides, Surface Diffusion, Plenum, New York (1998) 263.

[26] N. P. Kobayashi, T. R. Ramachandran, P. Chen, A. Madhukar, Appl. Phys. Lett. **68** (1996) 3299.

[27] D. Leonard, K. Pond, P. M. Petroff, Phys. Rev. B **50** (1994) 11687.

[28] J. Wu, P. Jin, X.-j. Lü, Y.-h. Jiao, Z.-g. Wang, Frontiers of Physics in China **2** (2007) 68.

[29] F. F. C. a. v. d. M. J. H., Proc. R. Soc. London, Ser. A (1949) 205.

[30] M. Volmer and A. Z. Weber, Phys. Chem. (1926) 277.

[31] L. K. I.N. Stranski, Akad. Weiss. Lit. Mainz Math.-Natur Kl. (1939).

[32] M. G. D.Bimberg, N.N.Ledentsov, Quantum Dot Heterostructures, John Wiley and Sons, London (2001).

[33] B. D. Shchukin.V, Physical Mechanisms of Self-Organized, Formation of Quantum Dots.

[34] L. Goldstein, F. Glas, J. Y. Marzin, M. N. Charasse, G. Le Roux, Appl. Phys. Lett. **47** (1985) 1099.

[35] D. J. Eaglesham, M. Cerullo, Physical Review Letters **64** (1990) 1943.

[36] S. Guha, A. Madhukar, K. C. Rajkumar, Appl. Phys. Lett. **57** (1990) 2110.

[37] R. Heitz, T. R. Ramachandran, A. Kalburge, Q. Xie, I. Mukhametzhanov, P. Chen, A. Madhukar, Phys. Rev. Lett. **78** (1997) 4071.

[38] A. M. T. R. Ramachandran, I. Mukhametzhanov, R. Heitz, A. Kalburge,Journal of Vacuum Science & Technology B: Microelectronics and Nanometer Structures **16** (1998) 1330.

[39] F. Patella, S. Nufris, F. Arciprete, M. Fanfoni, E. Placidi, A. Sgarlata, A. Balzarotti, Phys. Rev. B **67** (2003) 205308.

[40] T. J. Krzyzewski, P. B. Joyce, G. R. Bell, T. S. Jones, Phys.l Rev. B **66** (2002) 201302.

[41] T. J. Krzyzewski, P. B. Joyce, G. R. Bell, T. S. Jones, Surface Science **532-535** (2003) 822.

[42] K. A. Littau, P. J. Szajowski, A. J. Muller, A. R. Kortan, L. E. Brus, J. Phys. Chem. **97** (1993) 1224.

[43] D. M. Holunga, R. C. Flagan, H. A. Atwater, Industrial & Engineering Chemistry Research **44** (2005) 6332.

[44] Q. Zhang, S. C. Bayliss, D. A. Hutt, Appl. Phys. Lett. **66** (1995) 1977.

[45] J. U. Schmidt, B. Schmidt, Materials Science and Engineering B **101** (2003) 28.

[46] T. Orii, M. Hirasawa, T. Seto, Appl. Phys. Lett. **83** (2003) 3395.

[47] L. A. Nesbit, Appl. Phys. Lett. **46** (1985) 38.

[48] T. Shimizu-Iwayama, K. Fujita, S. Nakao, K. Saitoh, T. Fujita, N. Itoh, J. Appl. Phys. **75** (1994) 7779.

[49] T. Shimizu-Iwayama, N. Kurumado, D. E. Hole, P. D. Townsend, J. Appl. Phys. **83** (1998) 6018.

[50] K. S. Min, K. V. Shcheglov, C. M. Yang, H. A. Atwater, M. L. Brongersma, A. Polman, Appl. Phys. Lett. **69** (1996) 2033.

[51] P. Pellegrino, B. Garrido, C. García, R. Ferré, J. A. Moreno, J. R. Morante, Physica E: Low-dimensional Systems and Nanostructures **16** (2003) 424.

[52] S. R. C. Pinto, A. G. Rolo, A. Chahboun, R. J. Kashtiban, U. Bangert, M. J. M. Gomes, Thin Solid Films **518** (2010) 5378

[53] P. Caldelas, A. G. Rolo, M. J. M. Gomes, E. Alves, A. R. Ramos, O. Conde, S. Yerci, R. Turan, Vacuum **82** (2008) 1466.

[54] W. K. Choi, H. G. Chew, F. Zheng, W. K. Chim, Y. L. Foo, E. A. Fitzgerald, Appl. Phys. Lett. **89** (2006) 113126.

[55] A. Wellner, V. Paillard, C. Bonafos, H. Coffin, A. Claverie, B. Schmidt, K. H. Heinig, J. Appl. Phys. **94** (2003) 5639.

[56] I. H. Campbell, P. M. Fauchet, Solid State Communications **58** (1986) 739.

[57] A. G. Rolo, M. I. Vasilevskiy, O. Conde, M. J. M. Gomes, Thin Solid Films **336** (1998) 58.

[58] L. Liu, K. L. Teo, Z. X. Shen, J. S. Sun, E. H. Ong, A. V. Kolobov, Y. Maeda, Phys. Rev. B **69** (2004) 125333.

[59] F. Zheng, W. K. Choi, F. Lin, S. Tripathy, J. X. Zhang, The J. Phys. Chem. C **112** (2008) 9223.

[60] V. M. Ustinov, et al., Nanotechnology **11** (2000) 397.

[61] S. Mitsuru, E. Hiroji, H. Nobuaki, A. Yasuhiko, A. Tomoyuki, O. Kohji, N. Yoshiaki, SPIE **5365**(2004) 80.

[62] K. Eui-Tae, M. Anupam, Y. Zhengmao, C. C. Joe, Appl. Phys. Lett. **84** (2004) 3277.

[63] F. A. E Placidi, M Fanfoni, F Patella, E Orsini and A Balzarotti, J. Phys.: Condens. Matter **19** (2007) 225006

[64] P. B. Joyce, T. J. Krzyzewski, G. R. Bell, T. S. Jones, S. Malik, D. Childs, R. Murray, Phys. Rev. B **62** (2000) 10891.

[65] P. B. Joyce, T. J. Krzyzewski, G. R. Bell, B. A. Joyce, T. S. Jones, Phys. Rev. B **58** (1998) R15981.

[66] I. Kegel, T. H. Metzger, A. Lorke, J. Peisl, J. Stangl, G. Bauer, J. M. Garcیa, P. M. Petroff, Phys. Rev. Lett. **85** (2000) 1694.

[67] A. Rosenauer, D. Gerthsen, D. V. Dyck, M. Arzberger, G. Bhm, G. Abstreiter, Phys. Rev. B **64** (2001) 245334.

[68] X. Z. Liao, J. Zou, D. J. H. Cockayne, R. Leon, C. Lobo, Phys. Rev. Lett. **82** (1999) 5148.

[69] N. Grandjean, J. Massies, O. Tottereau, Phys. Rev. B **55** (1997) R10189.

[70] A. M. Sanchez, P. L. Galindo, S. Kret, M. Falke, R. Beanland, P. J. Goodhew, Microscopy and Microanalysis **12** (2006) 285.

[71] P. Wang, A. L. Bleloch, M. Falke, P. J. Goodhew, J. Ng, M. Missous, Appl. Phys. Lett. **89** (2006).

[72] T.-E. Nee, H.-T. Shen, J.-C. Wang, R.-M. Lin, Journal of Crystal Growth **287** (2006) 468.

[73] A. G. Cullis, D. J. Norris, T. Walther, M. A. Migliorato, M. Hopkinson, Phys. Rev. B **66** (2002) 081305.

[74] M. H. Gass, A. J. Papworth, T. J. Bullough, P. R. Chalker, Ultramicroscopy **101** (2004) 257.

[75] E. G. Bithell, W. M. Stobbs, J. Appl. Phys. **69** (1991) 2149.

[76] V. Grillo, Stem_Cell, http://tem.s3.infm.it/stemcell.htm

[77] A. Rosenauer, Transmission Electron Microscopy of Semiconductor Nanostructures., Springer, Berlin (2003).

[78] C. William. O'Mara, Robert B. Herring and Lee P. Hunt, Handbook of Semiconductor Silicon Technology, Noyes Publications New Jersey (1995).

[79] S. Furukawa and T. Miyasato , Jpn. J. Appl. Phys. (1988) L2207.

[80] L. T. Canham, Appl. Phys. Lett. **57** (1990) 1046-1048.

[81] S. Furukawa, T. Miyasato, Phys. Rev. B **38** (1988) 5726.

[82] J. Heitmann, Phys. Rev. B **69** (2004) 195309.

[83] L. Pavesi, J. Appl. Phys. **80** (1996) 216.

[84] B. Averboukh, J. Appl. Phys. **92** (2002) 3564.

[85] M. Luppi, S. Ossicini, J. Appl. Phys. **94** (2003) 2130.

[86] S. Godefroo, M. Hayne, M. Jivanescu, A. Stesmans, M. Zacharias, O. I. Lebedev, G. Van Tendeloo, V. V. Moshchalkov, Nat Nano **3** (2008) 174.

[87] G. Franzo, F. Priolo, S. Coffa, A. Polman, A. Carnera, Appl. Phys. Lett. **64** (1994) 2235.

[88] J. Michel, J. L. Benton, R. F. Ferrante, D. C. Jacobson, D. J. Eaglesham, E. A. Fitzgerald, Y. H. Xie, J. M. Poate, L. C. Kimerling, J. Appl. Phys. **70** (1991) 2672.

[89] S. Coffa, F. Priolo, G. Franzo, V. Bellani, A. Carnera, C. Spinella, Phys. Rev. B **48** (1993) 11782.

[90] H. S. Jung, K. Mun-Jun, S. Se-young, L. Choochon, Appl. Phys. Lett. **72** (1998) 1092.

[91] J. Palm, F. Gan, B. Zheng, J. Michel, L. C. Kimerling, Phys. Rev. B **54** (1996) 17603.

[92] P. G. Kik, M. J. A. de Dood, K. Kikoin, A. Polman, Appl.. Phys. Lett. **70** (1997) 1721.

[93] N. S. Bergano, J. Lightwave Tec. **23** (2005) 4125.

[94] W. J. Miniscalco, J. Lightwave Tec. **9** (1991) 234

[95] E. M. Yeatman, M. M. Ahmad, O. McCarthy, A. Vannucci, P. Gastaldo, D. Barbier, D. Mongardien, C. Moronvalle, Optics Communications **164** (1999) 19.

[96] G. Franzò, V. Vinciguerra, F. Priolo, Appl. Phys. A **69** (1999) 3.

[97] M. Fujii, M. Yoshida, Y. Kanzawa, S. Hayashi, K. Yamamoto, Appl. Phys. Lett. **71** (1997) 1198.

[98] G. F. D. Pacifici, F. Priolo,F. Iacona and L. Dal Negro, Phys. Rev. B **67** (2003) 245301.

[99] A. J. Kenyon, P. F. Trwoga, M. Federighi, C. W. Pitt, J. Phys. Con. Mat. **6** (1994) L319.

[100] P. G. Kik, A. Polman, J. Appl. Phys. **88** (2000) 1992.

[101] F. Priolo, G. Franzo, D. Pacifici, V. Vinciguerra, F. Iacona, A. Irrera, , J. Appl. Phys. **89** (2001) 264.

[102] D. Pacifici, G. Franzò, F. Iacona, S. Boninelli, A. Irrera, M. Miritello, F. Priolo, Materials Science and Engineering: B **105** (2003) 197.

[103] S. Schamm, G. Scarel, M. Fanciulli, Local Structure, Composition and Electronic Properties of Rare Earth Oxide Thin Films Studied Using Advanced Transmission Electron Microscopy Techniques (TEM-EELS), Rare Earth Oxide Thin Films (2007) 153.

[104] P. Pellegrino, B. Garrido, J. Arbiol, C. Garcia, Y. Lebour, J. R. Morante, Appl. Phys. Lett. **88** (2006) 121915.

[105] E. Bertel, F. P. Netzer, J. A. D. Matthew, Surface Science **103** (1981) 1.

[106] M. F. Cerqueira, M. Stepikhova, M. Losurdo, M. M. Giangregorio, A. Kozanecki, T. Monteiro, Optical Materials **28** (2006) 836.

[107] M. C. Cheynet, R. Pantel, Micron **37** (2006) 377.

[108] Brydson, R. and C. Hammond, Generic Methodologies for Nanotechnology:Classification and Fabrication., in Nanoscale science and technology, R.W. Kelsall, I.W. Hamley, and M. Geoghegan, Editors. 2005, John Wiley: Chichester.

[109] http://www.rare-metal.com/en/bigclassmemo.aspx?id=40

[110] http://onlineheavytheory.net/images/fig2.jpg

[111] http://www.polymicro.com/techsupport/techsupport_lowoh.htm